Epitaxial growth and characterization of GeTe and $GeTe/Sb_2Te_3$ superlattices

D I S S E R T A T I O N

zur Erlangung des akademischen Grades

Dr. rer. nat.
im Fach Physik

Spezialisierung: Experimentalphysik

eingereicht an der
Mathematisch-Naturwissenschaftlichen Fakultät
Humboldt-Universität zu Berlin

von
M.Sc. Rui Ning Wang

Präsident der Humboldt-Universität zu Berlin:
Prof. Dr.-Ing. Dr. Sabine Kunst

Dekan der Mathematisch-Naturwissenschaftlichen Fakultät:
Prof. Dr. Elmar Kulke

Gutachtern:
(i) Prof. Dr. Henning Riechert
(ii) Prof. Fulvia Patella
(iii) Dr. Raffaella Calarco

Tag der mündlichen Prüfung: 31.03.2017

Keywords: MBE, phase-change materials, GeTe, Sb_2Te_3, GeSbTe, chalcogenide superlattice, X-ray diffraction, reflection high-energy electron diffraction, Raman spectroscopy, resonant bonding, Peierls distorsion, intermixing.

Abstract

The growth by molecular beam epitaxy of GeTe and Sb_2Te_3/GeTe superlattices on three differently reconstructed Si(111) surfaces is demonstrated. Namely, these are the $Si(111)-(7\times7)$, $Si(111)-(\sqrt{3}\times\sqrt{3})R30°-Sb$, and $Si(111)-(1\times1)-H$ reconstructions. Through X-ray diffraction, the epitaxial relationship of GeTe is shown to depend on the passivation of the surface; in-plane twisted and twinned domains could be suppressed on a passivated surface. This behavior which resembles what would be expected from lamellar materials, is attributed to the relative weakness of resonant dangling bonds, that are further weakened by Peierls distortion.

At growth onset of GeTe, unusual phenomena are observed on the various surfaces by *in-situ* reflection high-energy electron diffraction; as further demonstrated by Raman spectroscopy, growth is initiated on the $Si(111)-(7\times7)$ and $Si(111)-(1\times1)-H$ reconstructions by the accumulation of an amorphous layer, although the growth parameters should clearly yield a crystalline film; a larger than expected in-plane lattice spacing is also measured at the growth onset of GeTe on $Si(111)-(\sqrt{3}\times\sqrt{3})R30°-Sb$, which could be explained by a disordering or suppression of Peierls distortion in this early stage of growth. These phenomena show that the stable structure in the bulk may not always be viable directly at growth onset in an ultra-thin film, the influence of the interface dominates in this case.

In the superlattice structure, the epitaxial relationship of the whole stack is shown to be decided by the very first layer already. Thus, no twisted domains are observed if they are suppressed in the initial layer. At the interfaces, intermixing between GeTe and Sb_2Te_3 into an ordered ternary GeSbTe alloy is observed and demonstrated by scanning-transmission electron microscopy and X-ray diffraction. The resulting structure is a stack of 2D materials. Taking advantage of the high-angle annular dark field detector's ability to discriminate atomic species by their contrast in atomic mass, the tendency toward ordering of each species into separate layers within the GST blocks is resolved. However, due to kinetic limitations and to the effect of diffusion, mixed Ge/Sb layers are observed, especially in the top-side of each GST sublayer. From these results, a model describing the intermixing during growth is presented.

Finally, through RHEED monitoring, a surprising variation of the in-plane lattice spacing is observed during the growth of the superlattices. It could be ascribed neither to classical epitaxy nor to van der Waals epitaxy. This is explained by a certain degree of coupling, even across van der Waals bonds. Supported by grazing-incidence X-ray diffraction, the possibility for strain engineering in van der Waals bonded superlattices is demonstrated.

Zusammenfassung

Die epitaktische Wachstum von GeTe Dünnschichten und Sb_2Te_3/GeTe Übergittern durch Molekularstrahlepitaxie wird auf drei verschiedenen Silizium Oberflächen gezeigt: $Si(111)-(7\times7)$, $Si(111)-(\sqrt{3}\times\sqrt{3})R30°-$Sb, und $Si(111)-(1\times1)-$H. Mit Röntgenstrukturanalyse wird bewiesen, dass die epitaktische Beziehung der GeTe Schicht von der Oberflächepassievierung abhängig ist; auf einer passivierten Fläche können verdrehte Domänen unterdrückt sein. Dieses Verhalten ähnelt dem, welches bei 2D Materialien zu erwarten wäre, und wird auf die Schwäche der Resonanten ungebundenen Zustände zurückgeführt, die durch Peierls Verzerrung noch schwächer werden.

Am Anfang des Wachstums werden ungewöhnliche Phänomene mit RHEED (Beugung hochenergetischer Elektronen bei Reflexion) auf den verschiedenen Oberflächen beobachtet; Im weiteren wird durch Raman-Spektroskopie nachgewiesen, dass Wachstum auf den $Si(111)-(7\times7)$ und $Si(111)-(1\times1)-$H Rekonstruktionen durch die Anhäufung einer amorphen Schicht eingeleitet wird, obwohl die Wachstumsparameter eindeutig einen kristallinen Film ergeben sollten. Auf der $Si(111)-(\sqrt{3}\times\sqrt{3})R30°-$Sb Oberfläche wird bei Einsetzen des Wachstums ein Gitterabstand gemessen, der grösser ist als erwartet, das durch eine Fehlordnung oder Unterdrückung der Peierls Verzerrung erklärt werden. Diese Ergebnisse zeigen, dass die Struktur im Volumenmaterial Beim Wachstum von ultradünn Schichten nicht immer stabil ist. Der Einfluss der Grenzfläche dominiert in diesem Fall.

Die epitaktische Beziehung des gesamten Stapels in der Übergitterstruktur wird bereits durch die erste Schicht entschieden, somit werden keine verdrehten Domänen beobachtet, wenn sie in der Ausgangsschicht unterdrückt werden. An den Grenzflächen zwischen GeTe und Sb_2Te_3 wird die Durchmischung in eine geordnete Ge-Sb-Te Legierung durch Rastertransmissionselektronenmikroskopie und Röntgenstrukturanalyse nachgewiesen. Die resultierende Struktur ist ein Stapel von 2D-Materialien. Mittels der Fähigkeit Elemente durch ihren Kontrast in Atommasse mit annularer Dunkelfelddetektoren zu unterscheiden wird die Tendenz zur Ordnung der einzelnen Elemente in getrennten Schichten innerhalb der GST Blöcke dargestellt. Jedoch aufgrund kinetischer Beschränkungen und auf der Diffusion werden gemischte Ge/Sb Schichten beobachtet, insbesondere in der oberen Seite jeder Ge-Sb-Te Schicht. Aus diesen Ergebnissen wurde ein Modell für die Durchmischung während des Wachstums erstellt.

Abchließend wird mittels RHEED eine überraschende Änderung des Gitterabstand während des Wachstums der Supergitter beobachtet. Es konnte weder der klassischen Epitaxie noch der van der Waals-Epitaxie zugeschrieben werden. Dies wird durch eine bestimmte Kopplungs über die van der Waals-Bindungen erklärt. Mittels Röntgenbeugung wird die Möglichkeit das Einstellen der Verzerrung in van der Waals gebundenen Gittern gezeigt.

Selbständigkeitserklärung

Ich erkläre, dass ich die vorliegende Arbeit selbständig und nur unter Verwendung der angegebenen Literatur und Hilfsmittel angefertigt habe.

Berlin, den Rui Ning Wang

List of publications

Publications written in the framework of this thesis

Towards truly single crystalline GeTe films: The relevance of the substrate surface
R. N. Wang, J. Boschker, E. Bruyer, D. Di Sante, S. Picozzi, K. Perumal, A.Giussani, H. Riechert, R. Calarco; *J. Phys. Chem C* 118 (51), 29724-29730 (2014)

Interface formation of two- and three-dimensionally bonded materials in the case of GeTe-Sb_2Te_3 superlattices
J. Momand, R. N. Wang, J. E. Boschker, M. A. Verheijen, R. Calarco, B. J. Kooi; *Nanoscale* 7, 19136-19143 (2015)

Intermixing during epitaxial growth of van der Waals bonded nominal GeTe/Sb_2Te_3 superlattices
R. N. Wang, V. Bragaglia, J. E. Boschker, R. Calarco; *Crystal Growth & Design* vol. 16, no. 7, pp. 3596–3601 (2016)

Peierls distortion prevented at growth onset of GeTe ultra-thin films
R. N. Wang, D. Campi, J. Momand, B. J. Kooi, M. Bernasconi, R. Calarco; *Scientific Reports* vol. 6, p. 32895 (2016)

[in submission] – **Genesis of resonant bonding in ultrathin GeTe films**
R. N. Wang, J. E. Boschker, H. Riechert, M. Wuttig, R. Calarco; *NPG Asia Materials* (2016)

[in preparation] – **2D or not 2D: Strain tuning in weakly coupled heterostructures**
R. N. Wang, F. Lange, S. Cecchi, T. Krause, A. Giussani, K. Perumal, M. Hanke, M. Wuttig, R. Calarco (2016)

Other publications

Surface reconstruction induced coincidence lattice formation between two dimensionally bonded materials and a three dimensionally bonded substrate
J. E. Boschker, J. Momand, V. Bragaglia, R. N. Wang, K. Perumal, A. Giussani, B. J. Kooi, H. Riechert, R. Calarco; *Nano Letters* 111, 28-32 (2014)

Laser-driven switching dynamics in phase change materials investigated by time resolved x-ray absorption spectroscopy
J. E. Boschker, R. N. Wang, V. Bragaglia, A. Giussani, R. Calarco, L. Le Guyader, M. Beye, I. Radu, K. Holldack, P. Fons, A. V. Kolobov; *Phase transitions* 88, 82-89 (2015)

Giant Rashba-type Spin Splitting in Ferroelectric GeTe(111)
M. Liebmann, C. Rinaldi, D. Di Sante, J. Kellner, C. Pauly, R. N. Wang, J. E. Boschker, A. Giussani, S. Bertoli, M. Cantoni, L. Baldrati, I. Vobornik, G. Panaccione, D. Marchenko, J. Sanchez-Barriga, O. Rader, R. Calarco, S. Picozzi, R. Bertacco, M. Morgensternp; *Advanced Materials* vol. 28, no. 3, pp. 560–565 (2016)

Evidence for spin to charge conversion in GeTe(111)
C. Rinaldi, J. C. Rojas-Sánchez, R. N. Wang, Y. Fu, S. Oyarzun, L. Vila, S. Bertoli, M. Asa, L. Baldrati, M. Cantoni, J.-M. George, R. Calarco, A. Fert, R. Bertacco; *APL Materials* vol. 4, no. 3, p. 032501 (2016)

Spin mapping of surface and bulk Rashba states in ferroelectric α-GeTe(111) films
H. J. Elmers, R. Wallauer, M. Liebmann, J. Kellner, M. Morgenstern, R. N. Wang, J. E. Boschker, R. Calarco, O. Rader, D. Kutnyakhov, S.V. Chernov, K. Medjanik, C. Tusche, M. Ellguth, H. Volfova, H. Borek, J. Braun, J. Minár, H. Ebert, and G. Schönhense; *Physical Review Letters* vol.94, no.201403 (2016)

Laser induced structural transformation in chalcogenide based superlattices
E. Zallo, R. N. Wang, V. Bragaglia, and R. Calarco; *Appl. Phys. Lett.* vol. 108, no. 22, p. 221904 (2016)

Atomic stacking and van-der-Waals bonding in GeTe-Sb_2Te_3 superlattices
J. Momand, F. R. L. Lange, R. N. Wang, J. E. Boschker, M. A. Verheijen, R. Calarco, M. Wuttig, B. J. Kooi; *Journal of Materials Research*, pp. 1–10 (2016)

[in submission] – **Accurate control of interface sharpness in Sb_2Te_3/GeSbTe van der Waals superlattices**
S. Cecchi, E. Zallo, J. Momand, R. N. Wang, B. J. Kooi, M. A. Verheijen, R. Calarco; *Applied Materials & Interfaces* (2016)

Conference presentations and dissemination

Study of GeTe and Sb_2Te_3-GeTe alloys by time resolved XANES
EPCOS 2013 Poster Presentation
R. N. Wang, J. E. Boschker, V. Bragaglia, A. Giussani, R. Calarco, L. Le Guyader, M. Beye, I. Radu, K. Holldack, P. Fons, A. V. Kolobov

Epitaxial Growth of Sb_2Te_3/GeTe Superlattices by Molecular Beam Epitaxy
DPG Spring 2014 Conference talk
R. N. Wang, J. E. Boschker, R. Calarco, J. Momand, B. J. Kooi

Growth of Quasi-Single-Crystalline GeTe Films by Molecular Beam Epitaxy
MRS Spring 2014 Conference talk
R. N. Wang, J. E. Boschker, R. Calarco

Growth of Germanium Telluride Thin Films on Passivated Silicon Surfaces by Molecular Beam Epitaxy
DPG Spring 2015 Conference talk
R. N. Wang, J. E. Boschker, R. Calarco

At the Interfaces Between GeTe and Sb_2Te_3 in Chalcogenide Superlattices
MRS Spring 2015 Conference talk
R. N. Wang, J. E. Boschker, R. Calarco, J. Momand, B. J. Kooi, M. Verheijen

Epitaxial Growth of GeTe and GeTe/Sb_2Te_3 Superlattice Structures
PDI Internal Institute Seminar (2015)
R. N. Wang, J. E. Boschker, R. Calarco, J. Momand, B. J. Kooi, M. Verheijen

XRD and TEM Characterization of GeTe/Sb_2Te_3 Superlattice Structures
PDI Internal Student Seminar (2015)
R. N. Wang, J. E. Boschker, R. Calarco, J. Momand, B. J. Kooi, M. Verheijen

Contents

Acknowledgements

The present work came to fruition thanks to the many co-workers at the Paul-Drude-Institut and external collaborators. A large array of complementary skills and techniques in material fabrication and characterization are gathered at the institute, blended in a friendly and constructive atmosphere. In the following, the main contributors are acknowledged, each in their own field of expertise.

First of all, I would like to thank Prof. Dr. Henning Riechert for giving me the opportunity and privilege to work at the institute as a PhD student. I am very grateful for the financial support provided during the last six months.

I would also like to thank Prof. Henning Riechert, Dr. Raffaella Calarco, Prof. Fulvia Patella, Prof. Christoph T. Koch, and Prof. W, Ted Masselink for accepting to be part of the thesis review committee. Thank you for taking interest in my work, and for giving me the chance to compete for the PhD title.

I wish to thank Dr. Lutz Geelhaar as head of the epitaxy department, and Dr. Raffaella Calarco as my direct supervisor in the phase change material group. I was truly blessed with the caring leadership, the continuous support, the wise guidance and feedback, and the most inspiring enthusiasm for science.

I would like to thank all my colleagues in the phase change material group; Dr. Alessandro Giussani and Dr. Karthick Perumal for initiating me to the world of phase change materials and MBE growth; Valeria Bragaglia, Dr. Jos E. Boschker, Dr. Eugenio Zallo, Dr. Stefano Cecchi, and Prof. Fabrizio Arciprete for all the fruitful and never-ending discussions. From the inception of each idea, to the analysis of results, including the design and realization of the experiments, none of the content presented here would have been possible without them.

In the institute, I would like to thank all technicians in the MBE lab; Carsten Stemmler, Steffen Behnke, and Hans-Peter Schönherr for the incredible feat of keeping the Pharao II MBE machine operational; Claudia Hermann for support in the chemical lab and on the AFM setup; Dr. Bernd Jenichen for X-ray diffractometry at the institute, Dr. Michael

Hanke, Thilo Krause and Giovanni Li Destri for measurements at the ESRF beamline; Dr. Timur Flissikowski and Dr. Manfred Ramsteiner for discussion and support with Raman spectroscopy; Many thanks to Mr. Andreas Hartung and Mrs. Kerstin Arnhold for the support with all the administrative tasks.

For three years of financial support and for the fruitful collaboration, I would like to acknowledge all the members in the FP7 project PASTRY (GA 317746), coordinated by Dr. Andrea Redaelli from Micron Technology Inc., with special mentions for the group of Prof. Bart J. Kooi with Jamo Momand from the Zernike Institute for Advanced Materials of the University of Groningen who took care of all the TEM imaging in collaboration with Dr. Marcel Verheijen at the Eindhoven University of Technology. Equally, I wish to thank Prof. Mattias Wuttig and Felix Lange from the RWTH Aachen University for the close collaboration on the interpretation, modelling, and publishing of data acquired on ultra-thin GeTe films and superlattice structures.

I would like also to acknowledge Dr. Silvia Picozzi and Dr. Emilie Bruyer from CNR-SPIN in L'Aquila, and Dr. Domenico Di Sante from the Department of Physical and Chemical Sciences in the University of L'Aquila for the theoretical calculations on GeTe surface reconstructions. I would like to thank Prof. Marco Bernasconi and Dr. Davide Campi from the University of Milano-Bicocca for their work on Raman calculations and relaxation in ultra-thin GeTe films.

Finally, I would like to thank my family for their long-distance but very effective support. Thanks to my numerous colleagues and new friends for all the resourcing coffee and lunch breaks, for discovering and enjoying the city of Berlin together, and for making my stay here so pleasant and memorable.

Motivation

Electronics and big data have reached such a level of omnipresence in every aspect of daily life that it almost seems superfluous to mention Moore's law at this point. And yet, it is not enough: Research fields such as neuroscience, genomics, particle physics, astrophysics, or quantum computing are still bottlenecked by a lack of computational power. Data is being generated much faster than it can be processed. Although immense progress has been made in data science, revolutionizing how data is acquired, processed, compressed, stored, read, analyzed, and presented, the insatiable need for more capable memory devices has never been felt as strongly.

Due to the excessively high requirements to fulfill, data storage devices have been designed to specifically address certain needs, at the expense of other aspects. Different devices are then combined and made to synergize within one electronic device. Thus, data storage in hard disk drives (HDD) is slow, but the memory is non-volatile, meaning that virtually no energy is needed to keep the data intact. On the other hand, data in dynamic random access memories (DRAM) can be stored and processed very quickly, but will be lost as soon as the device is not powered anymore. From this perspective, the Holy Grail of memory devices would feature all desired characteristics: non-volatile, scalable, low energy consumption, cheap, and fast.

In this quest for the perfect memory device, phase change materials (PCM) are serious contenders. Because their working principle is based on the switching between two stable states, they at least fulfill the non-volatile requirement. In fact, they are at the base of rewritable CD, DVDs and Blue-Ray technology. In these applications, data is accessed optically, which involves the comparatively slow scanning of the active medium under the reading/writing laser. Recent efforts have been invested toward the electronic access to the data in phase-change DRAM devices (PCRAM), potentially combining non-volatile data with the speed of DRAM.

The landscape of electric data storage is currently filled by two main technologies; DRAM and solid state drives (SSD) based on NAND flash architecture. DRAM has already been presented above as a volatile memory device, its strength resides in its fast access to in-

dividual bits of data. SSD on the other hand is non-volatile and less greedy energetically, but more expensive to produce, it's major caveat is that data can only be processed by blocks of thousands of bits. And while read operations do not deteriorate the device, SSDs only offer a limited number of guaranteed successful rewriting operations. Although this limit is nowadays high enough so that the replacement of HDDs by SSDs is reasonably foreseeable for common daily consumer usage, they remain extremely ill adapted to work as DRAMs.

At the boundary between these two technologies, there is space for a compromise that combines the freedom of access and speed offered by DRAMs with the non-volatility and energy efficiency of SSDs. And this is the field where PCRAM technology has the most chances to shine in its current state. These positions are however not static; as long as deeper fundamental understanding of PCMs and their switching mechanism translates into enhanced performances in memory devices, PCRAM can carve out its own territory by conquering applications where it could surpass DRAMs or SSDs. For instance, cells based on PCMs also benefit from a simple and straightforward architecture; the active material only needs to be connected to selector electrodes, which is even more simple than DRAMs requiring one transistor and capacitor per bit. This allows PCMs to be more easily integrated into three-dimentional memory devices such as the 3D XPoint technology recently announced by Intel and Micron, introducing a paradigm shift that could render planar device designs obsolete in the long term.

The active material itself can also be greatly improved; as it will be further discussed in the introduction, reduction of configurational entropy by texturing of the material into a superlattice structure has shown to enhance switching performances. This shows how critical it is at this point to better understand the fundamental phenomena shaping these materials, in order to better engineer their properties. And to this end, the fabrication of the highest quality samples can help to discriminate the effect of defects, and isolate the underlying phenomena at the core. With this objective in mind, GeTe and GeTe/Sb_2Te_3 superlattices are grown by molecular beam epitaxy on silicon substrates after different surface treatments. Though the study of epitaxial registry and structural characterization, insights about the fundamental phenomena shaping the structure and switching mechanism of these materials are obtained.

1 Introduction to phase-change materials

1.1 Phase-change properties

Phase change materials designate a class of materials that can be switched reversibly between at least an amorphous and an crystalline phase. Owing to a difference in the bonding nature and atomic arrangement, a striking change in the optical and electrical properties occurs between the amorphous phase with low reflectivity and high resistance, and the crystalline phase with high reflectivity and low resistance.[1–4] The latter, being the more stable phase, can be obtained from the amorphous phase by bringing the material to the crystallization temperature (T_x) and giving enough time to let the structure reorganize. On the other hand, a strong spike in energy that sends the material above the melting point (T_m) can disorganize the crystalline phase, the material can then be frozen in its metastable amorphous phase by a rapid quenching. These two processes are illustrated in Figure 1.1(a). For technological purposes, the amorphization is often called the power limiting process because of the energy needed to reach T_m, while crystallization is data rate limiting because of the time needed to let crystallization take place.

Switching between the two phases can be triggered on a very short timescale, and at a reasonable energetic cost,[6] in a way that almost seems paradoxical, considering how contrasting their properties are. It is therefore no surprise that these materials have been exploited during the past two decades in optical data storage applications such as rewritable CDs, DVDs, and now Blue-Ray discs.[7] More recent efforts have also been invested to utilize more specifically the change in electrical properties of such materials in non-volatile electronic memory devices.[8,9] In all these applications, the most commonly used materials, as well as the most promising future candidates, are chalcogenides;[7] this term simply refers to the chemical compounds containing one or more elements from the sixth column of the periodic table (excluding oxygen). In Figure 1.1(b) the technologically relevant chalcogenide alloys are gathered in one single ternary alloy diagram.

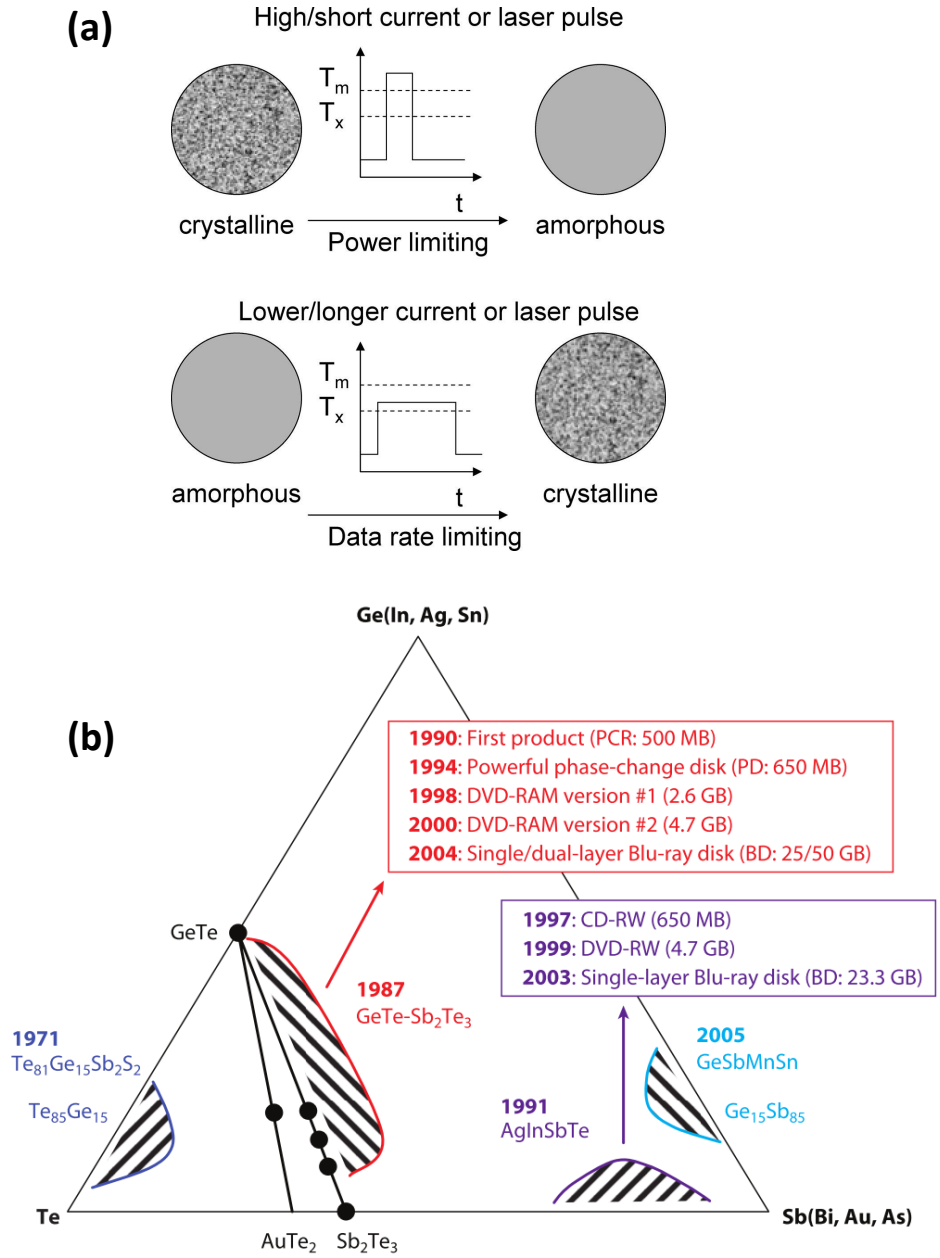

Figure 1.1: (a) Schematic showing the crystallization and amorphization processes in phase change materials.[3] (b) Ternary diagram of chalcogenide compounds. Several alloys used in phase change data storage applications are indicated.[5]

In this thesis work, the attention is not directly directed on the phase-change mechanism itself, but rather about the fundamental structural characteristics of these materials that make switching possible. More specifically, exemplified in germanium telluride (GeTe), insights are attained by observing the epitaxial relationships that are established between GeTe and differently reconstructed Si surfaces. In a second part, the structure of epitaxial GeTe/Sb_2Te_3 chalcogenide superlattices is elucidated, as such structures have promising properties,[10,11] but are still currently relatively poorly understood. Beyond their application as phase-change materials, the structure of these chalcogenide compounds and heterostructures also define their other most relevant properties as topological insulators,[12,13] or thermoelectric materials.[14,15]

1.2 Germanium telluride, the phase change archetype

Considering its very simple stoichiometry, GeTe is a rather unconventional and complex compound from the fundamental point of view. In its amorphous phase (a-GeTe), it is covalently bond, mainly in 4-fold coordinated *sp3* tetrahedra,[16] a configuration quite commonly found with amorphous semiconductors.[17] In fact, the electrical and optical properties of a-GeTe are what one could expect from any amorphous semiconductor. It is really the crystalline phase of GeTe (c-Gete) that displays extraordinary properties.

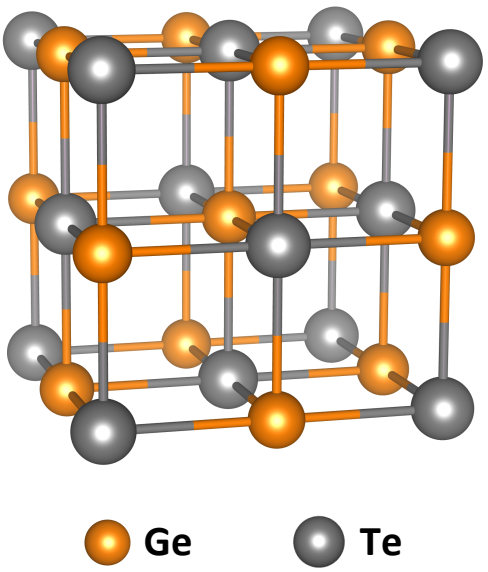

Figure 1.2: Schematic model of a cubic β-GeTe crystal with its rock-salt structure.

To fully describe its structure, it is best to start with a simplified model where all Ge and Te atoms are sitting on their own sub-lattice, in a rock-salt structure. Incidentally, this cubic GeTe crystalline phase does exist at high temperature, and is called the β-GeTe phase (Figure 1.2). While the rock-salt structures are usually found for crystals with a stronger ionic character, more compatible with the necessity to accommodate six direct neighbors, the octahedral configuration in GeTe is stabilized by another phenomena; it is owed to resonant bonding.

1.2.1 Resonant bonding

Both Ge and Te use electrons in their outer *p* shell to create bonds, and between them they possess three electrons in average per atom. This amount is clearly insufficient for the formation of saturated bonds with all six neighbors. Instead, a compromise is reached by adopting a resonant state, stemming from the superposition of equivalent virtual states where they would form saturated bonds with only half of the neighbors. Bonding is therefore achieved in each of the three dimensions by one unsaturated resonant orbital, binding each atom with the two neighbors at opposite sides.[2,18] Resonant bonding is illustrated in the case of pure Sb in Figure 1.3. This peculiar bonding mechanism, which can neither be defined as ionic, nor as hybridized,[19] is truly at the origin of the distinct optical properties of c-GeTe. In this configuration, the *p* electron density is highly delocalized and polarizable, which has a critical incidence on the dielectric function and reflectivity of the material.[2,20]

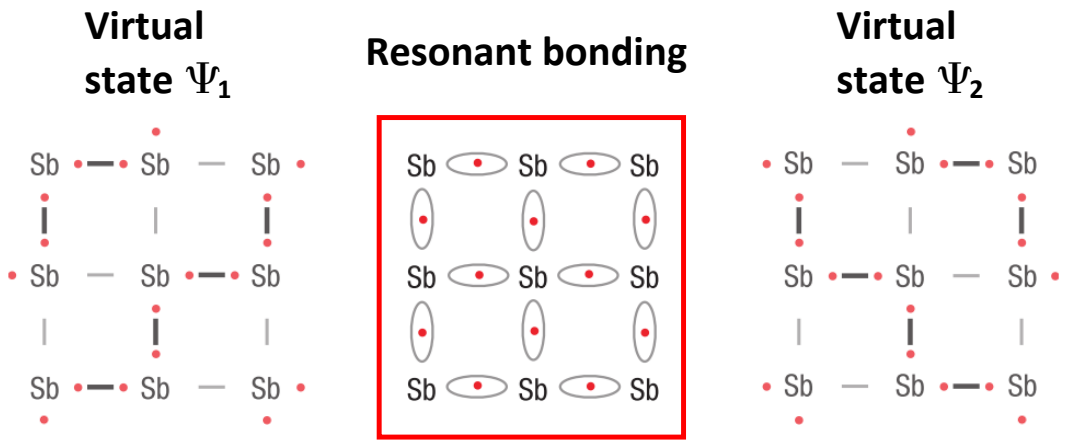

Figure 1.3: Schematic model of crystalline Sb, with its resonant bonds originating from the superposition of the two virtual states Ψ_1 and Ψ_2.[2]

1.2.2 Peierls distortion

The best proof of the compliance in this resonant structure resides in the second fundamental phenomenon that defines its shape: Peierls distortions, also called Yahn-Teller effect when applied to covalent molecules. These terms describe the intrinsic desire for any metallic periodic chain of atoms to form dimers. Because from an electronic point of view, going from a mono-atomic chain to di-atomic means splitting the single metallic band into two separate bands and opening a bandgap at the Fermi level. This has for effect to stabilize the system by lowering slightly the energy of the occupied states, while raising the level of the empty conduction band. This is illustrated schematically in Figure 1.4. Of course the trade-off is that the elastic energy is upset, the atoms being displaced from their ideal positions.[21]

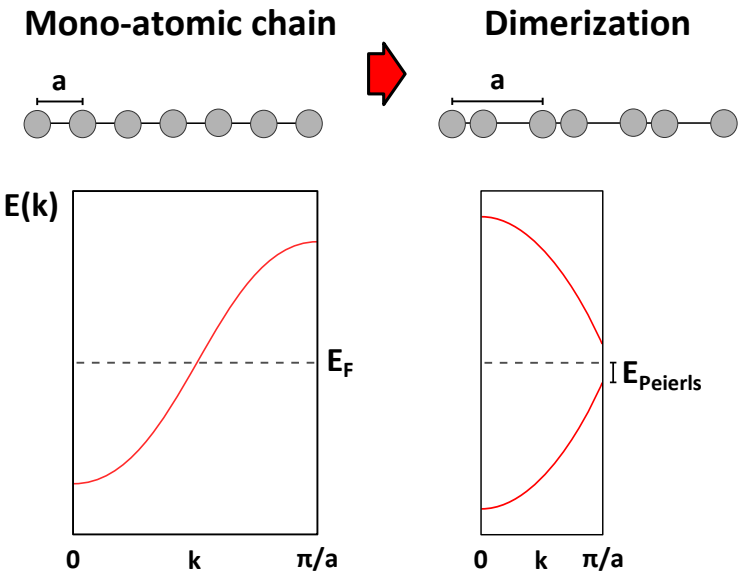

Figure 1.4: Schematic band diagrams showing the electronic stability gained by dimerization of a mono-atomic chain.

But in resonantly bonded structures, displacing atoms does not cost so much elastic energy, because of their compliance and high electron delocalization discussed above. As long as the *p* orbitals overlap each other, the structure maintains a good stability.[22] In GeTe, Peierls distortion has for effect the formation of alternated short strong bonds and longer weaker ones.[19,23] Incidentally, it has been shown to be favorable for these short and long bonds to be distributed in an orderly fashion, into layers in the ⟨111⟩ direction.[24] As a result, the crystal is elongated in this direction, leading to a rhombohedral distortion of the cubic rocksalt unit cell. The structure of α-GeTe found at room tem-

perature (RT) is thus obtained, as illustrated in Figure 1.5. In this schematic model, the short strong bonds are represented by thicker connectors, while the long weak bonds are thinner.

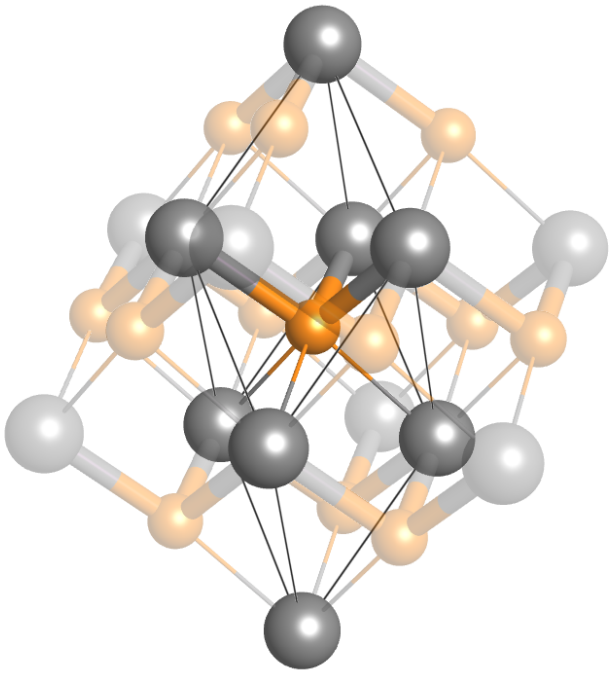

Figure 1.5: Schematic model of α-GeTe, with the primitive cell in rhombohedral coordinate system highlighted. The additional atoms of the distorted rocksalt unit cell are shown in transparent overlay.

The direct consequence of this ordered rhombohedral distortion is a shift of the Ge sublattice with respect to the Te atoms. The two sublattices no longer share the same center of charge, a ferroelectric polarization is induced in α-GeTe.[25–28] At a longer range, This dipolar moment also exists spontaneously, already without prior polarization by an external field. The favorable ordering of the Peierls distorted bonds acts like a driving force, guiding and aligning the polarization direction in neighboring crystalline unit cells.

Rashba spin-splitting has also been demonstrated in GeTe.[29] It is intriguing that such properties are present in GeTe, because they are usually expected from two-dimensional systems. It is again the alternation of the strong and weak bonds that give the GeTe similar properties than layered materials. The Rashba effect is of special interest in GeTe because it synergies very well with its ferroelectric properties. Indeed, the dipolar moment in GeTe could be utilized to control and switch the electronic spin simply via an electric field.[30,31] The coupling between these properties opens up a whole new dimension of possible spintronic devices.

As stated above, GeTe adopts a cubic β-GeTe structure at high temperature (∼720K), which can initially lead to think that the Peierls effect is suppressed. This could even be understood from the schematic in Figure 1.4; as thermally activated electrons start filling the higher energy states in the conduction band, the splitting of the bands is not favorable anymore, and it would be better to merge the bands again and go back to a periodic mono-atomic chain. This view has however been challenged:[32] Using X-ray absorption fine structure (EXAFS) measurements, it has been shown that bond hierarchy by Peierls effect was still present in the cubic β-GeTe phase, except that the long and short bonds would be randomly distributed, leading to a structure that appears to be cubic in average.

1.2.3 Intrinsic Ge vacancies

As shown very schematically in Figure 1.4, the Peierls distorted GeTe should be a semiconductor with its Fermi level in the middle of the gap. But this is contradicted by experimental data, where p-type conduction with a carrier concentration of the order of 10^{20} cm^{-3} is typically measured.[33–35] The reason for this discrepancy has been identified as the presence of defects in the form of Ge vacancies in a far from negligible concentration of $\sim 8-10\%$ on the Ge sublattice.[36] These defects have been shown to have the lowest formation energy among a collection of different possible candidates.[37] In fact, starting from a perfect crystal, with a Fermi level in the middle of the bandgap, the formation energy of Ge vacancies is even negative, meaning that they will form spontaneously and are intrinsic to the material.

In the same publication, it has been shown that the germanium vacancy is "self-healing", meaning that upon removal of one Ge atom, the neighboring Te atoms keep their threefold resonant p orbitals and simply bind more strongly to the other Ge atom still present on the other side. But these p states still need the electrons previously provided by the Ge atom. With each less Ge atom, only the associated s state is truly removed, with its concomitant need for two electrons. But four outer-shell electrons are taken out of the system. Therefore, each vacancy leads to a total of two missing electrons, or in other words, the formation of two holes. On the band diagram, the introduction of these intrinsic holes will lead to a lowering of the Fermi level toward the valence band. And as the Fermi level is lowered, the formation energy of further vacancies gradually increases and becomes less likely. By the time an equilibrium concentration of Ge vacancies is reached, the Fermi level is already in the top part of the valence band, giving to GeTe it's

characteristic but at first unexpected p-type conduction. Combined with the intrinsic ferroelectric polarization, these two electric properties that are not often found in the same material.

It is interesting to make here a quick estimation of the expected density of carriers from the concentration of vacancies: Considering a rock-salt-like Ge_4Te_4 unit cell with cell parameter 6Å, one cubic centimeter contains 4.6×10^{24} unit cells. Each cell contains four Ge sublattice sites, 8% of these sites contain vacancies, and each vacancy contributes two carriers. In theory, in a perfect crystal, the Ge vacancies should contribute to a carrier concentration of $\sim 3 \times 10^{21} cm^{-3}$. This value is higher than the experimentally measured $10^{20} cm^{-3}$, but does not take into account all other possible defects that could trap or annihilate the carriers (grain boundaries, Te vacancies, oxygen or silicon contamination). This simple estimate remains a good indication that all free carriers in GeTe probably originate from these vacancies.

The electric properties of GeTe do not fall within the scope of the present thesis, therefore these vacancies will not be further investigated. Edward et al.[37] have calculated that they should not play an important role in the crystalline structure of GeTe, despite their important concentration, since the introduction of these defects only barely repositions the neighboring Te atoms. They could however play an important role in the phase switching mechanism, as it has been calculated that they provide convenient pathways for the diffusion of Ge atoms,[38] helping in the necessary rearrangement of atoms between the two phases. Vacancies are also present in Ge-Sb-Te ternary compounds (GST), where they play an even more important role, as their ordering into layers has been shown to drive a metal-insulator transition, or grant topological insulator properties.[12,39]

1.3 Antimony telluride, almost a phase-change material

Although the properties of antimony telluride are not specifically investigated in this thesis work, this compound is still relevant as one of the component of the $GeTe/Sb_2Te_3$ superlattice structures. It is also one of the extremities of the pseudo-binary line shown in Figure 1.1, encompassing most of the technologically relevant phase change materials. But by itself, Sb_2Te_3 is not considered to be one of them; its high propensity for crystallization makes the amorphous phase unstable and unreliable for technological applications.

But clearly, the reason why ternary GST compounds show superior phase-change performances compared to the binary GeTe is because they borrow some of their aptitude to crystallize from Sb_2Te_3. Studies have shown however that crystallization in Sb_2Te_3 could maybe be harnessed by introducing very heavy nitrogen doping.[40]

Sb_2Te_3, just like GeTe, is a resonantly bonded material. But in the densely packed (111) planes (in cubic notation), each molecular block of five atomic layers is separated from the neighbor blocks by an empty layer on the Sb sublattice. The facing Te atoms on each side of the vacant layer are separated by a van der Waals gap (vdW gap). Better than with words, the structure of Sb_2Te_3 is illustrated in Figure 1.6. It is noteworthy to underline that the Te sublattice follows a cubic stacking in the out-of-plane axis for GeTe (ABCABCABC), whereas it becomes an hexagonal stacking in Sb_2Te_3 (ABCBCACAB), with the introduction of these vdW gaps.

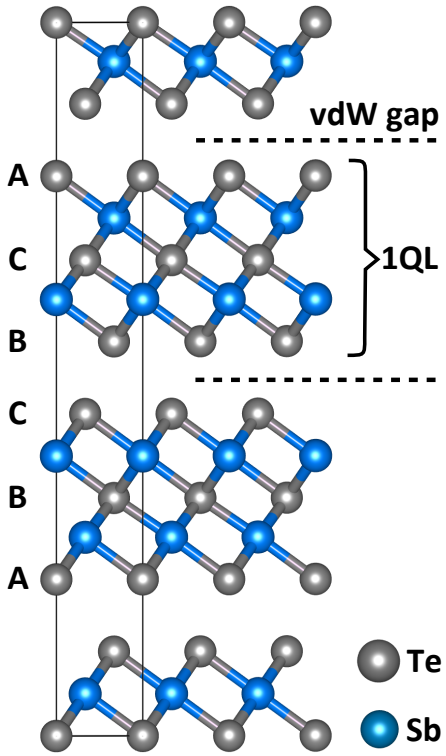

Figure 1.6: Scale model of the crystalline Sb_2Te_3 structure. The stacking sequence for the Te sublattice is indicated on the left-hand side. vdW gaps and the size of one QL is highlighted.

The existence of these vdW gaps can be easily understood by considering that Sb_2Te_3 is indeed a resonantly bonded material. As shown in the case of GeTe, the ideal resonantly bonded network possesses an average of three p electrons per atom, distributed on the resonant orbitals p_x, p_y, and p_z in all three dimensions. Pure Sb, and pure Bi, also have three p electrons per atom and they are resonantly bonded. The average number of p

electrons in Sb_2Te_3 is however 3.6 electrons per atom; there is a surplus of 0.6 electrons per atom. After each five atomic layers, the amount of electrons in surplus amounts to three. Which means that there are enough spare electrons to fill the resonant state, without the necessity for an extra layer of atoms. Therefore the vdW gap is created.

In fact, the same simple arithmetic argument can be applied to all the ordered stoichiometric GST compounds. $Ge_1Sb_2Te_4$ has an average of 3.429 electrons per atom, therefore its ordered structure has one vdW gap each seven atomic layers, because that is the number of atoms needed to accumulate three electrons in surplus. $Ge_2Sb_2Te_5$ has an average of 3.33 electrons per atom, in other words a surplus of 0.33 electrons per atom. $9 \times 0.33 = 3$, therefore there is one vdW gap after each 9 atomic layer. Finally, $Ge_3Sb_2Te_6$ has 3.27 electron per atom, a surplus of 0.27, therefore one vdW gap after each eleven atomic layers, because $11 \times 0,273 = 3$. In their metastable configuration, the formation of intrinsic vacancies[41] can be explained in a similar fashion: In a resonantly bonded network, it is favorable for the crystal to have no more than an average of three electrons per lattice site. The formation of vacancies could be understood as a mechanism to get rid of excess electrons. This logic however can not be applied to GeTe, it already has an average of three electron per atom in its perfectly stoichiometric form. The formation of Ge vacancies in GeTe must be driven by other phenomena.

In analogy with the bond hierarchy in GeTe, the Sb-Te bond lengths are also not uniform in Sb_2Te_3: The bonds at the edge of the block, closer to the vdW gaps, are shorter than the bonds near the middle of the block. Therefore, the disparity in this case is caused by the presence of vdW gaps, rather than by Peierls distortion. Another way to understand this is to consider that there is no necessity for Peierls distortion, since the periodicity of the chains is already broken by the presence of vdW gaps. But because the bonds are distorted symmetrically at both edges of the blocks, Sb_2Te_3 is not a ferroelectric material.

Sb_2Te_3 can boast to possess other interesting properties, such as the thermoelectric effect. To assess the performances of thermoelectric materials, the figure of merit $Z = \sigma \cdot S^2/\kappa$ is calculated, with σ the electric conductivity, S the Seebeck coefficient, and κ the thermal conductivity. κ is in the denominator, because it is important to maintain a gradient of temperature across the material in order to benefit from the thermoelectric effect. In the case of Sb_2Te_3, modeled on its crystalline structure, the thermal conductivity is highly anisotropic. Because of the vdW gaps, the heat conduction via phonons in the out-of-plane direction is very low.[42] It has also been proposed that the resonant bonds themselves contribute to the low thermal conductivity: The atoms interact with each other on a longer range within the resonant network, but because they are not perfectly periodically spaced, it induces anharmonic phonon scattering.[43]

Low thermal conduction is also beneficial for phase change memory applications, because it ensures that heat is confined in the active area, and minimizes cross-talk between neighboring cells. From this point of view, ordered GST structures have a clear advantage over GeTe or meta-stable GST because of the presence of vdW gaps.

1.4 $GeTe/Sb_2Te_3$ Chalcogenide superlattices

Chalcogenide superlattices (CSL) have been shortly mentioned in the introduction above, and deserve to be presented more in detail. The concept behind a superlattice structure is to stack different materials of few nanometer thickness on top of each other in order to combine their existing properties, or give rise to new superior properties that are not found in the separate materials. The most common purpose of such heterostructures is bandgap engineering, but for phase change materials, the goal is however different.

Among the first instances of CSL stuctures found in the litterature, Chong *et al.*[44] tested amorphous $GeTe/Sb_2Te_3$ superlattices after annealing, with optical data storage applications in mind. They found shorter crystallization time under optical excitation, compared to the homogeneous GST alloy of the same average composition. Similar experiments were conducted by Cao & Quiang,[45] where lower activation energy for crystallization were obtained by differential scanning calorimetry. In both cases, the formation of ternary GST compounds was observed at the interfaces after crystallization.

At the same time, these CSL structures have also been investigated for electrical data storage applications.[46] It was first proposed that such structures benefited from low programming current because of their lower thermal conductivity. Later, Simpson *et al.*[10] suggest that there may be more than just thermal conductivity at play. Using physical vapor deposition, CSLs with 1 nm thin amorphous GeTe sublayers sandwiched between 4 nm thick crystalline Sb_2Te_3 blocks were grown and fully crystallized by annealing. Such structures showed reduced switching energies, improved write-erase cycle lifetimes, and faster switching speeds. These improvements are attributed to the natural tendency for the intercalated Sb_2Te_3 layers to texture themselves in the out-of-plane direction, offering a template for the crystallization of GeTe. Thus, the configurational entropy difference between the two phases is reduced, enabling the switching between them without undergoing melting. The device-damaging long-range atomic diffusion[47,48] is also greatly suppressed.

Since then, various models have been proposed to understand the switching mechanism, and elucidate the structures of the SET and RESET states.[49–52] Interpretations can at times even seem to be in disagreement, but one has to keep in mind that there can be different levels of texturing in CSLs produced using different methods. The enhanced properties in CSLs are very likely derived from an array of various phenomena, that can have more or less pronounced effects depending on the specific structure and fabrication methods. In the fundamental investigation of CSLs, the challenge for the scientific community is to identify and deconvolute these different contributions, seek a deeper understanding for each of them, in order to rebuild all these aspects together into one global picture.

2 Experimental methods and theory

In the following chapter, a general description of the synthesis of thin-films by molecular beam epitaxy (MBE) is given, with relevant considerations about the growth process and epitaxial relationships. The different characterization methods of interest are then discussed. For each one of them, a short description is given about the fundamental phenomena dictating the interaction between the probe and the specimen. From there, the capabilities and limitations of each technique are presented, with a special care to bring clarifications about the interaction volume, and the domain of validity of the measurements. The three initial Si(111) surface reconstructions employed in the framework of this thesis are then presented, along with the procedure that was followed to obtain them.

2.1 Thin-film synthesis by molecular beam epitaxy

All thin-films investigated in the present thesis were prepared using MBE. This method combines atomic species evaporated or sublimated at a low rate from the highest purity effusion sources, and ultra-high vacuum (UHV) conditions at $10^{-10}\,mbar$, ensuring the lowest possible concentration of impurities. To initiate the deposition, the substrate surface is simply exposed to the flux of material emitted by the cells. Owing to the low flux and UHV conditions, the evaporated species have such a large mean-free path that they are certain to arrive to the substrate surface without encountering intermediate collisions with other molecules.

By keeping the flux of material low, and by heating the substrate, all impinging atoms or molecules are given a chance to diffuse on the surface, and to find a preferred site to be adsorbed. Using a crystalline substrate, the position of these favorable sites will be defined by its crystalline structure at the exposed surface. And if the deposited material is also crystalline, its orientation will be inherited from the substrate; an epitaxial relationship is established between the film and the substrate. If no favorable sites are found within the time where the atoms are allowed to diffuse, with enough heat supplied to

the substrate, the rejected atoms are desorbed and captured by the cryogenically cooled chamber shroud, thus keeping the UHV background pressure and a controlled concentration of the different species present on the surface.

Thus, MBE enables the growth of very high purity and high quality crystalline structures in a controlled fashion, at the cost of very slow deposition rates. It is therefore a method most successful in the fabrication of low-dimensional structures such as quantum dots, nanowires, quantum wells, and thin films. The applications for these structures in optoelectronics are innumerable. To only cite a few, terahertz quantum-cascade lasers based on GaAs/$Al_{0.25}Ga_{0.75}As$ heterostructures,[53] light-emitting diodes based on (In,Ga)N quantum wells in GaN nanowires,[54] based on the same materials in core-shell geometry[55] can be mentioned.

The MBE system used in the framework of this thesis was custom-built by CreaTecFischer & Co. GmbH. In contrast with other MBE systems where the substrate is positioned above the cells, facing down, the substrates and cells are oriented along the horizontal axis here. This peculiar design was chosen to adapt the MBE to be mounted on the BESSY II beamlines for real-time in-situ characterization by X-ray diffraction.[56] However, for the experiments conducted throughout this thesis, the machine was taken out of the beamline and installed in the MBE lab of the Paul-Drude Institut.

This system is composed of three vacuum chambers of progressive quality. The first chamber is the load-lock, used for transferring samples in and out of the system. Pumped down to $10^{-8}\,mbar$, the stage can be heated for degassing, and it is equipped with a RF sputtering unit that can be used to apply protective capping layers (Si_3N_4, ZnS-SiO_2, TiN, or W) on the samples before exposing them to the atmospheric environment. The second part is the transfer chamber, where the substrate can be further baked and degassed, at a pressure of $10^{-9}\,mbar$. It also acts as a buffer zone before the substrate is introduced into the UHV growth chamber at $10^{-10}\,mbar$. The growth chamber hosts four ports for cells, three of them are occupied by the Ge, Sb, and Te cells. The fourth port holds a second Te cell that is not actively in use. In addition to beryllium windows that are transparent to the synchrotron x-ray radiation and allow the in-situ measurements on the beamline, a reflection high-energy electron diffraction system is also integrated. For flux calibration and desorption studies, the chamber is equipped with a molecular beam flux monitor, an atmospheric quadrupole mass spectrometer (QMS), and an in-line QMS. Unfortunately, the in-line QMS was out of commission and could not be used for this thesis.

2.1.1 Epitaxial growth processes

In heteroepitaxy, three different growth processes can occur: The first possibility is the so-called two-dimentional Frank-van der Merwe layer-by-layer growth, where each molecular layer grows to ideally cover the whole surface before a new layer nucleates. In contrast, isolated three-dimensional islands can nucleate and coalesce simultaneously, forming a much rougher film (Volmer-Weber process). The third possible mechanism is the so-called Stranski-Krastanov process, where growth initially starts in a layer-by-layer fashion, until three-dimensional islands are formed on top of the epilayer, due to the accumulated strain in the film once a certain critical thickness is reached. These three scenarios are illustrated in Figure 2.1. In order to achieve a flat fully covering thin-film with low surface roughness, only the layer-by-layer mechanism is desirable. This is even more important in the case of superlattices, where additional layers need to be stacked on top of each other.

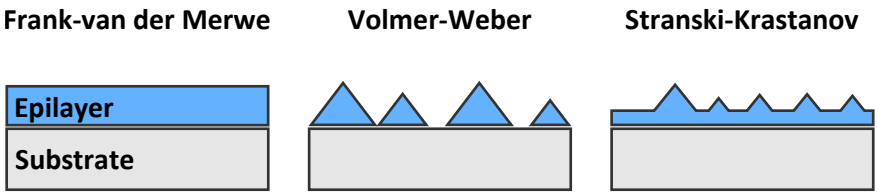

Figure 2.1: Schematic diagram showing the Frank-van der Merwe, Volmer-Weber, and Stranski-Krastanov growth modes for heteroepitaxy.

In order to make two-dimensional growth favorable, the sum of the free energies from the newly created interface and film surface needs to be inferior to the free energy of the initial substrate surface. For the bare substrate and the film surface, the free energies are defined by the respective crystalline structures and cleavage planes. As for the free energy of the interface, it will depend on the epitaxial relationship and the nature of the bonds keeping the two materials together. At this interface, there will most likely be a certain mismatch between them. And as a rule of thumb, the larger the mismatch the higher the risks to find undesired three-dimensional growth, since a larger mismatch is generally speaking synonym of a higher interface free energy.

Fortunately, these values for the free energies, that are static at equilibrium, can be tailored by changing the growth kinetics. For instance, the surface diffusivity can be enhanced by increasing the growth temperature, or by decreasing the total impinging flux. Both the thermodynamics and kinetics of the system can also be changed by saturat-

ing the surface environment with selected chemical species, or by introducing a surfactant.[57,58] Therefore, epitaxial growth in the thin film geometry by MBE goes beyond the epilayer and substrate pairs that are simply allowed by thermodynamics at equilibrium.

2.1.2 Types of epitaxial registry

While the growth process shapes the morphology of the film, it is the epitaxial relationship that decides the crystalline orientation inside the film. And this is defined by an array of characteristics shared among the film and the substrate; the crystalline structure of both materials at the interface, their symmetry and mismatch in their cleavage plane, the chemical species at the surface, and the presence of dangling bonds.

In the best case scenario, only one epitaxial relationship is clearly favored energetically over all other possible orientations. But even in that ideal case, single crystalline orientation is no synonym of single crystal. For instance, anti-site boundaries can occur between grains that nucleated and coalesced separately.

In-plane rotational domains can also occur because of symmetry considerations.[59] If the film is of a higher symmetry that englobes the one of the substrate, or if they both share the same one, epitaxial relationships between all equivalent surfaces are indistinguishable. But if the symmetries are dissimilar, the same epitaxial relationship between equivalent surfaces will yield domains that appear to be rotated with respect to each other. In a first approximation, these domains are mostly energetically equivalent.

Then, at the edge of a cleaved crystal, because of the missing neighbors that would normally be expected in the bulk, the usual crystalline structure cannot be adopted. Instead, the surface atoms attempt to reorganize themselves in order to minimize the amount and impact of the dangling bonds left behind by the cleaving. It is however unlikely for the material to eliminate all dangling bonds all by itself, because if such an advantageous configuration existed, it could then also be adopted in the bulk. Therefore, a certain number of dangling bonds will always remain.

If the mismatch between the substrate and the film is reasonably low ($\leqslant 7\,\%$), the first few atomic layers of the deposited film will strain themselves to adapt to the lattice of the substrate. As the volume of deposited material increases, elastic energy is accumulated due to the stress in the film. Once a certain critical thickness is reached, the material will start to release that stress by the formation of misfit dislocations. This scenario is commonly referred as a case of classical lattice-matched epitaxy, and the value of the critical

thickness is inversely proportional to the mismatch. It is worth noting that this critical thickness is different from that of the three-dimensional island formation in the Stranski-Krastanov growth process. If strain is released via dislocation formation, islanding by Stranski-Krastanov can be prevented or postponed, and vice-versa. Intuitively, islanding could be favored if the free energy of specific island facets is low in comparison to the free energy of the strained surface.

When the mismatch between the substrate and the film is too large ($\geqslant 8\,\%$), the critical thickness for misfit dislocation formation approaches the order of one single atomic layer.[60] In this case, the two lattices cannot be matched anymore, and the film relaxes immediately by forming misfit dislocations directly at the interface. However, since a correspondence could not be found at the range of the unit cells, the epilayer material will still attempt to match an integer number of its unit cell with more distant lattice points of the substrate, to form epitaxial domains. As a result, the film is not fully relaxed; there is generally some residual domain mismatch, but it is typically much smaller compared to the lattice mismatch ($\leqslant 1\,\%$). This type of epitaxial registry is called domain-matched epitaxy. In each instance, there might be more than one possible correspondence between the lattice points of the film and the substrate. And each of these correspondence could potentially lead to the formation of energetically non-equivalent in-plane twisted domains.

By terminating the dangling bonds of the cleaved surface with selected alien species, the interaction with the material deposited above is reduced. If this material has a two-dimensional lamellar structure, there would not be any strong bonds left across the interface, the saturated bonds on both sides would only interact through van der Waals forces, thus the name given to such cases: van der Waals epitaxy. The low interaction here makes the lattice mismatch less relevant; ideally, the film can grow directly relaxed, with little defects and without introducing dislocations. For epitaxial purposes, it is however desirable for the film to keep an interaction with the substrate that is strong enough, so that a clear epitaxial relationship can still be dictated by the symmetry of the substrate. If the interaction is really too weak, as exemplified by the epitaxy of graphite on Pt(111), the film could be polycrystalline, with domains randomly oriented in the in-plane direction.[61]

2.2 Thin-film characterization methods

2.2.1 Crystallinity investigation by X-ray diffraction

X-ray diffraction (XRD) is a characterization method based on the interference of a collimated monochromatic X-ray beam after scattering upon a periodic crystalline structure. X-rays have a relatively high transmittance through matter, and can penetrate 10-100 µm into the sample. The lateral size of the spot is also in the 100 µm range, which means that XRD is considered as an averaging bulk technique.

When coherent X-rays strike a periodic crystal, they interact with electrons in outer electronic shells, where part of them are assimilated and re-emitted radially in all directions, interfering with each other. At specific angles described by the rules of Laue diffraction, this interference can be constructive, and result into a diffracted beam. The angles at which these reflections occur, as well as their relative intensity, is directly linked to the crystalline structures in the specimen. Using a triple-axis XRD spectrometer, the orientation of the sample can be changed with respect to the incident X-ray beam, and the orientation of the detector can be changed with respect to the sample. The source, sample, and detector can therefore be setup to investigate specific diffracted beams. The diffractometer used for XRD characterization in this thesis was the triple-axis Panalytical X'Pert PRO MRD system with Ge(220) hybrid monocromator, employing a monochromated Cu-Kα1 radiation (λ= 1.54 Å).

A common analysis method is the symmetrical ω-2θ scan, where the inclination of the incident beam with respect to the sample is mirrored by the detector. In this geometry, only the diffractions generated by lattice planes stacked in the out-of plane direction are measured. As a first step in the determination of an eventual epitaxial relationship between the substrate and a deposited film, this scan provides information about its out-of-plane component. In order to access the in-plane component, scans in the φ-scan configuration are performed. In this case, the setup is oriented to show a reflection from a set of diffracting planes that possess some in-plane component in their normal. The stage is then rotated around it's out of plane-axis, and information about the symmetry and in-plane texture can be obtained from the breadth of the reflections from the equivalent planes, and the angular distance between them. This is schematically shown in Figure 2.2.

In the rocking curve technique (or ω-scan), the sample and detector are oriented to highlight one specific reflection. The stage is then slightly rocked around its ideal position. Information about the crystalline quality or misorientation of thction of the diffracted

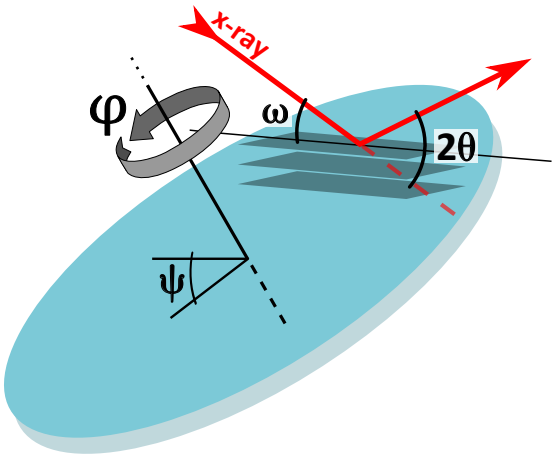

Figure 2.2: Schematic diagram of XRD $\varphi-$scan geometry. The sample is tilted by an angle ψ in order to set off-axis planes so that they are orthogonal to the plane of the source and detector. $\omega-2\theta$ is then set into Bragg condition with respect to this specific set of plane. The sample is then rotated around φ in order to measure all planes of the same family.

beam due to the slight perturbations. The rocking curve measurement can also be performed for any ω-2θ pair of angles within a certain range, yielding a reciprocal space map (RSM), to get a more complete picture of the crystalline state in the sample. By imaging a wider section of the reciprocal space, including multiple reflections, their relative position can be used to determine the state of strain in the film in respect to the substrate or to other layers.[62]

2.2.2 Thin-film characterization by X-ray reflectivity

Interestingly, the same equipment used for XRD can be utilized to exploit a radically different interaction between X-rays and a thin film; that is X-ray reflectivity (XRR). Due to the difference in refractive index and underlying electron density between the sample and air, there is a critical angle below which all incident X-rays are reflected. Above this angle, part of the beam is able to be refracted into the material, changing its phase velocity both in direction and magnitude, depending on the contrast in refractive index. If the incident angle is increased too much, the portion of the beam that is reflected will drastically decrease, most of it is absorbed into the sample.

But at low angle, reflection and refraction events can thus occur multiple times at each interface in the sample. If a refracted beam is able to escape the thin-film , it will recover the same direction and velocity as the directly reflected beam, owing to the conservation of momentum. However, because the beam will have traveled a longer path at slower

speeds in the material, it could be out of phase from the main specular reflection, and will therefore interfere with it. By increasing the incident angle, the path-length is gradually reduced, making the phase-shift alternate between a constructive and a destructive interference. Plotted with respect to the incident angle, the total reflected intensity will therefore show periodic oscillations, the so called Kiessig fringes. From the shape of the oscillations, their periodicity, and the extinction of the reflected beam as the incident angle increases, the density of each layer in the film, their thickness, and the roughness at each interface can be estimated by comparing the acquired spectra with theoretical simulations.

This method is of course an averaging technique, the rather large collimated X-ray spot being additionally spread out in the incident direction because of the small incidence angle. XRR can be performed indiscriminately on amorphous and crystalline material, since it does not rely on diffraction, but only on the contrast in electron density. The theory behind this phenomena is well known, such that even complex multi-layered structures can be simulated. The addition of many free variables in a complex case should however be considered carefully, as XRR is not a direct characterization method, and different sets of parameter could yield similar fits.

2.2.3 Real-time in-situ surface characterization by reflection high-energy electron diffraction

The MBE chamber is equipped with a reflection high-energy electron diffraction system (RHEED) to monitor the evolution of the surface in real-time during growth. RHEED analysis is based on the diffraction of a focused monochromatic high-energy electron beam striking the sample at a grazing angle. The impinging electrons are charged particles, and they are subjected to Coulomb interactions with the nuclei and other electrons of the atoms in the investigated sample. Their scattering probability is therefore much higher compared to X-rays of the same energy, leading to a lesser penetration depth. Combined with the shallow geometry of incidence, the volume investigated by RHEED is strictly limited to the topmost surface.

Because the diffracting volume is of a very finite size in the out-of-plane direction, and cannot be considered as infinite anymore. The more commonly encountered sharp spots are diffusely broadened vertically, connecting the reciprocal lattice nodes into rods. The intersection of these reciprocal rods with the Ewald sphere then gives rise long vertical

streaks.[63] In fact, if spots are observed in RHEED instead of streaks, it indicates the presence of faceted islands or other 3-dimensional structures protruding from the flat surface and reducing the out-of-plane confinement.

The RHEED pattern is generated from two distinct interactions between the incident beam and the surface. The first kind of interaction is specular reflection. Because $k_{\perp}$, the wave vector component perpendicular to the surface, is very small due to the grazing incidence, a portion of the e-beam is reflected by the negative potential barrier formed by the surface electrons.[64] By definition, this specular reflection remains in the plane of the incident beam. The other contribution comes from electrons diffracted by the in-plane periodic structures that are orthogonal to the incident beam. These diffracted beams form the streaks on each side of the specular beam and carry the information about the crystalline structure of the surface, as their lateral spacing is inversely proportional to the periodic arrangement of the atoms. In practice, as illustrated in Figure 2.3, supposing a (111) oriented surface, and an incidence beam aligned along the in-plane $[01\bar{1}]$ direction, the RHEED pattern gives an indication about the spacing between the $\{\bar{2}11\}$ lattice planes, whose normals are orthogonal to the incident direction. By rotating the sample around its out-of-plane axis, the incident beam can be aligned along different azimuths, revealing the lattice spacing in each respective orthogonal direction.

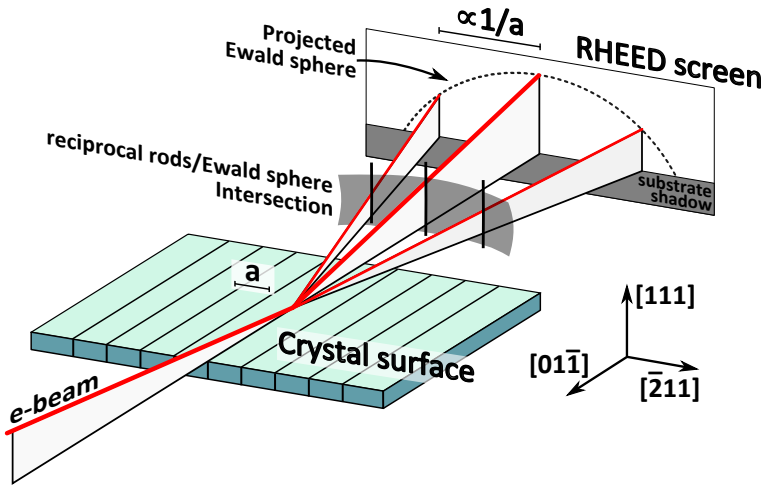

Figure 2.3: Schematic diagram of RHEED geometry, showing the incident electron beam at grazing angle, diffracted by the atomic planes perpendicular to the incident direction. The image formed on the screen originates from the intersection between the Ewald sphere and the reciprocal rods.

At a cleaved crystal surface, the atoms are not coupled with their usual neighbors, their equilibrium is upset. These atoms will often be displaced and adopt a reconstructed arrangement. RHEED is also sensitive to larger periodic modulations, such as these surface reconstructions. Because of the high energy, well collimated, and mono-chromated

electron source used in RHEED, the lateral coherence length is in the 100 nm range. This means that electrons remain coherent within this range, and they are able to interfere constructively when they are diffracted by periodic structures within this size.[65] RHEED is therefore able to easily resolve large superstructures such as the $Si(111) - (7 \times 7)$ reconstruction, as several repetitions of these superstructures can be expected within the coherence length of the beam. It is noteworthy to underline that the coherence length does not equate the interaction volume of the beam, which is typically 1 mm in the incident direction, 100 µm laterally, and less than 1 nm in depth.

Another consequence of the large coherence length, which is both a curse and a blessing, is that RHEED is not so sensitive to disordered defects. The disadvantage is that amorphous phases and defects merely produce a diffuse background, difficult to characterize and quantify using this method. The advantage is that small crystallites can be resolved, even in the midst of a disordered phase. The presence of a secondary minority crystalline phase can also be easily detected by their own RHEED streaks. A polycrystalline surface can also easily be recognized by the presence of rings, similar to the pattern expected from such a sample investigated by XRD.

The specular beam itself also carries information about the surface; its intensity is highly dependent on the surface roughness. Most famously, in the case of a layer by layer growth, intensity oscillations are observed over time during growth. Starting with a perfectly flat fully covered layer, roughness increases as new islands nucleate and coalesce. This causes a decrease of the RHEED specular intensity. As the new layer approaches full coverage, its roughness diminishes again, until a perfectly flat layer is recovered again once full coverage is reached. As long as the growth remains two-dimensional, oscillations can be measured, and their period can be used to precisely determine the growth rate.[66]

2.2.4 Molecular bonding investigation by Raman spectroscopy

While XRD and RHEED are both based on diffraction phenomena, related to periodicity and long range order in a crystal, Raman spectroscopy uses the inelastic interaction between optical laser radiation and electron orbitals to probe the binding and conformation of atoms in the short range. This method can therefore be applied indiscriminately to amorphous and crystalline material. Using a focusing objective lens, a laser spot as small as 1 µm can be obtained. Depending on the wavelength of the chosen laser and sampled

materials, penetration depth can vary in a range from few nanometers to few micrometers. To a certain extent, Raman spectroscopy can be considered as an averaging bulk characterization method.

To be more specific fundamentally, it is the electromagnetic field of the photons that excites the electron densities present around the molecules. Depending on how susceptible these orbitals are to polarization, they are prompted to oscillate in unison with the monochromatic light, turning the molecule into an oscillating dipole. Under such acceleration, the electrons are in turn radiating their own electromagnetic wave. In most cases, the emitted and impinging light have the same wavelength, no energy is exchanged. In this case, the emitted radiation does not carry any information about the material, the scattering event is considered to be elastic (Rayleigh scattering).

In rare one-in-a-million cases, the oscillation of the dipole is coupled with vibrational modes in the molecule or crystal. As a result, the wavelength of the emitted light differs from the impinging one. If energy is taken away from the oscillating dipole, to send the molecule into a higher excited vibrational state, the emitted radiation will have less energy and a longer wavelength (Stockes Raman scattering). The polarization of the impinging light can also work against an already excited state, pushing it back down into its ground state. In this case, the energy of the excited state will be added to the emitted radiation, and a shorter wavelength is observed (anti-Stockes Raman scattering). At a given temperature, the difference between the incoming and outgoing energy will match signature values for the different vibrational states of the material, depending on the nature of the atoms and the bondings between them. At room temperature, the vibrational ground states are more dominantly populated, making the Stockes scattering more likely. In fact, due to its temperature dependance, the ratio between Stockes and anti-Stockes events can be used to calculate an effective temperature in the material. For general purposes, and in the scope of this thesis, only the Stockes scattered Raman is measured.

The response of the material to the polarizing radiation is highly dependent on the relative orientation between the polarization of the light and the crystalline structure of the material. This is even further exacerbated in the case of a single crystalline thin-film, where the orientation is dictated by the epitaxial relationship. One has to take special care to make sure that the geometry of incidence of the laser and its direction of polarization are not laid out in way such that some vibrational modes are suppressed. A good practice is to compare with Raman spectra acquired on a polycrystalline sample of the same material,[28] where all existing modes are expected.

The setup used for the Raman measurements in the framework of this thesis was the HORIBA LabRAM HR Evolution. Measurements were taken in backscattering $z(x, xy)\bar{z}$ geometry, meaning that incident light is polarized in the x direction, while the polarization of the backscattered light is not selected. The 632.8 nm line of a He-Ne laser was used to excite the material, and the scattered light was analyzed using a spectrometer equipped with an LN_2-cooled charge-coupled device detector.

2.2.5 Surface morphology by atomic force microscopy

Atomic force microscopy (AFM) is based on the interatomic forces between the surface and a sharp micro-engineered AFM tip positioned in very close proximity, within few nanometers. The tip is located at the end of a piezoelectric cantilever, and the force exerted on the tip causes the cantilever to bend. From its deflection, the height of the surface can be imaged with a resolution of a fraction of a nanometer. The cantilever itself is mounted on a high-precision XY piezo-stage, allowing to trail the tip over the surface and scan the topology over areas up to 100 μm, with a lateral resolution of few nanometers. The setup used was the Bruker Dimension 3100 system.

Investigating the morphology of a surface is highly relevant, especially when an heterostructure is to be stacked on top of it. The surface quality then constitutes the upper limit for the interface quality. An assessment of the grain size and crystal symmetry can often be drawn from the surface morphology, using this very straightforward technique that does not require specific sample preparation or complex setup alignment procedures.

There are mainly two different ways to drive an AFM: In contact mode, the tip is kept in contact with the surface, and the topological map is drawn from the deflection of the cantilever. In tapping mode, an oscillation is induced into the cantilever, in close proximity from the surface. The tip only touches the surface intermittently, and is not dragged along over the surface. The atomic forces from the surface interfere with this oscillator, and the topological information can be deduced from the loss in amplitude of the oscillation. Tapping mode is the method of choice with soft materials like the resonantly bonded chalcogenides. In contact mode, the hard tip could damage the surface. Debris would then attach themselves to the tip by vdW forces, ruining the resolution of the probe.

There is a large variety of setups similar to AFM that use a nano-engineered tip to probe different properties. To only cite few examples, elastic properties can for example be assessed using ultrasound force microscopy, where an the tip is in contact with the surface

and made to vibrate at ultrasound frequencies.[67,68] In piezo-force microscopy, a voltage is applied to the sample surface through the tip, the deformation induced by piezo-effect can be used to map the polarization domains of the surface.[25] With scanning tunneling microscopy, in addition to imaging the local density of states, the tip can also be used to displace adsorbed species over a surface, to operate specific nano-engineering tasks.[69]

2.3 Three different Si(111) surface reconstructions

Undeniably, the state of the substrate surface is critical in epitaxial growth, and the epitaxial relationship can be tailored by modifying the surface. Throughout this thesis work, the effect of three different Si(111) surface reconstructions on the epitaxy of GeTe are investigated. Namely, following the order in which they will be presented, the hydrogen passivated $Si(111)-(1\times1)-H$, the non-passivated $Si(111)-(7\times7)$, and the Sb passivated $Si(111)-(\sqrt{3}\times\sqrt{3})R30°-Sb$. At the end of this part, RHEED images for each of these reconstructed surfaces are presented in Figure 2.6, acquired along the two $\langle\bar{2}11\rangle$ and $\langle\bar{1}10\rangle$ azimuths. Owing to the 6-fold symmetry of the (111) surfaces, these are the two azimuths that need to be characterized to identify the size of the reconstructed cell.

2.3.1 Hydrogen passivated $Si(111)-(1\times1)-H$

When in contact with the atmosphere, the silicon surface forms a $2\,nm$ thick amorphous oxide.[70] In commercial wafers, the surface is often protected from deeper scratches by enhancing this native oxide into a $100\,nm$ thermal oxide, by treating the surface under oxygen atmosphere between $600-1000°C$. For any epitaxial process, this oxide layer needs to be stripped, and the surface needs to be protected from further oxidation during the transfer of the substrate into the growth chamber.

For this purpose, there is only one chemical agent adapted and commonly used in industry for the dissociation of silicon oxide: Hydrofluoric acid (HF). Typically, a 10 minutes dip into a 5% solution buffered with ammonium fluoride (NH_4F) is enough to entirely remove the thermal oxide layer. A convenient feature of this wet-etching treatment is that the bare Si(111) surface is directly passivated by hydrogen,[71] forming the $Si(111)-(1\times1)-H$ surface. After HF etching and throughout rinsing, the silicon substrate can readily be transfered into the MBE system, without fear of further oxidation.

Chemically, the treatment by HF can lead to two main different kind of passivation: The monohydride SiH with the top layer silicon atoms bound to three other silicon below and passivated by one single hydrogen atom above, or the trihydride SiH_3 bound to one single silicon atom below and passivated by three hydrogen atoms above (dihydrides can also be found as defects).[72] These two main configurations depend on which Si(111) atomic plane is etched away. The simple dipping process with the buffered HF employed in this thesis work is known to consistently create the first kind of passivation, with monohydrides on the flat surfaces.[73]

The RHEED patterns formed by this surface reconstruction are shown in the upper panels of Figure 2.6. As the size of the cell stays unitary and no superstructure is formed, the lattice spacing is simply inversely proportional to the distance between the streaks. On these RHEED images, the Kikuchi lines are well visible, testifying of the cleanness, smoothness, and crystalline quality of the surface preparation.

2.3.2 Non-passivated $\mathrm{Si}(111) - (7 \times 7)$

Once the $\mathrm{Si}(111) - (1 \times 1) - \mathrm{H}$ reconstructed sample is introduced into the growth chamber, after the preliminary thermal treatments in the load-lock and transfer chamber get rid of adsorbed water and oxygen, the silicon substrate can already be used as it is. As an alternative, the rather weakly bond hydrogen atoms can be totally desorbed by heating the substrate to 720°C. At this temperature, left to its own device, in absence of passivating species, the Si(111) surface reconstructs into the large and rather artistic 7×7 structure illustrated in Figure 2.4. Once this reconstruction is formed, it is preserved even if the substrate is cooled back to RT, or growth temperature.

This reconstruction is easily identified by RHEED, as shown by the middle panels of Figure 2.6. The spacing between 1×1 streaks in both azimuths is now divided by additional streaks into 7 equal parts, indicating the formation of a commensurate superstructure that is seven times larger in both directions. Especially on the image taken along the $\langle \bar{1}10 \rangle$ azimuth, the 1^{st} order Laue circle can be seen. The sharpness of these higher order reflections demonstrates the quality of the surface reconstruction.

From a non-reconstructed 7×7 surface that would create 49 dangling bonds, only 19 remain on specific atoms. This shows just how favorable it is energetically to minimize the number of these dangling bonds, considering the trouble the surface goes through in order to create this complex structure that spans over 49 unit cells and three atomic

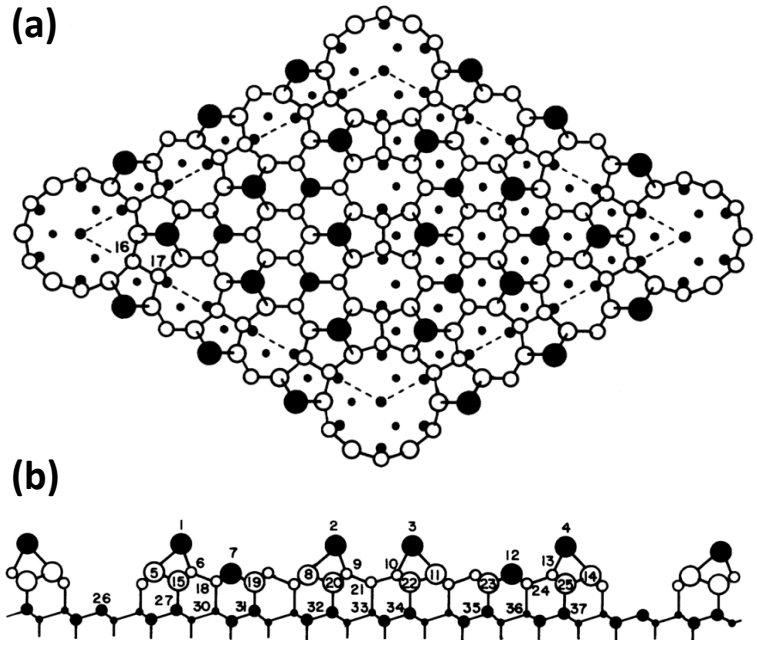

Figure 2.4: (a) *Ab initio* model of the $\mathrm{Si}(111)-(7\times7)$ reconstruction in top view.[74] Atoms at increasing distances from the surface are indicated by circles of decreasing size. (b) Side view.

layers in the out-of-plane direction.[74] This surface is very interesting to investigate as a comparison with other fully passivated surfaces, to understand the role these dangling bonds play in the epitaxy of GeTe.

2.3.3 Antimony passivated $\mathrm{Si}(111)-(\sqrt{3}\times\sqrt{3})R30°-\mathrm{Sb}$

Starting from $\mathrm{Si}(111)-(7\times7)$, an Sb terminated $\mathrm{Si}(111)-(\sqrt{3}\times\sqrt{3})R30°-\mathrm{Sb}$ surface can be obtained, following a process described in Park *et al.*[75] The substrate temperature is gradually ramped down from 720 to 350°C, while the surface is exposed to a flux of Sb (Cell temperature $T(Sb)_{Base}=455$°C, $T(Sb)_{Tip}=605$°C). At this rather high temperature, only one single monolayer of Sb is expected to resist desorption on the Si(111) surface.[76], arranged into so called "milk-stool" structures, where Sb atoms are bundled into groups of three, each one being bound to one Si and the two neighbor Sb. This structure is best described in Bengio *et al.*,[77] and schematically illustrated in Figure 2.5. This resulting surface is also fully passivated, like $\mathrm{Si}(111)-(1\times1)-\mathrm{H}$. The comparison between the two is interesting to investigate, in particular the effect of different surface terminating species on the epitaxy of GeTe.

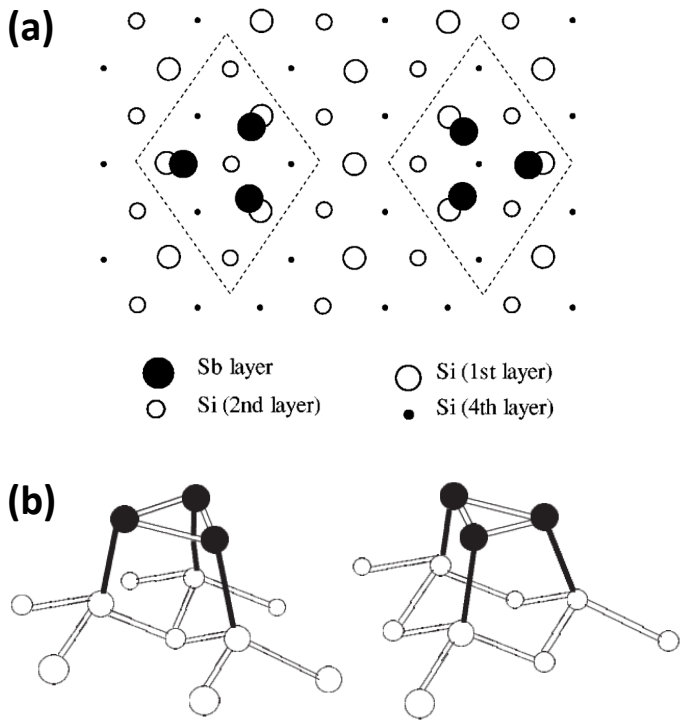

Figure 2.5: (a) Schematic top view of the two variants of "milk-stool" structures forming the $Si(111) - (\sqrt{3} \times \sqrt{3})R30° -$ Sb reconstruction.[77](b) 3D view.[78]

The RHEED pattern of this surface reconstruction are shown in the lower panels of Figure 2.6. Compared to the 1×1 surface, the distance between the streaks is identical along $\langle \bar{2}11 \rangle$, but three times smaller along $\langle \bar{1}10 \rangle$. The dimmer intensity of higher order reflections and Kikuchi lines show that the surface quality may be slightly lower compared to the two other reconstructions.

In this $Si(111) - (\sqrt{3} \times \sqrt{3})R30° -$ Sb reconstruction, each surface Si atom is bound to a Sb. It may seem surprising that such a structure can be obtained starting from the $Si(111) - (7 \times 7)$, where the number of dangling bonds has already considerably reduced. In order to obtain the new reconstruction, previously formed covalent Si-Si bonds need to be torn apart, to be supplanted by the new Si-Sb bonds. In fact the transition from $Si(111) - (7 \times 7)$ to $Si(111) - (\sqrt{3} \times \sqrt{3})R30° -$ Sb is rather complex, several intermediate reconstructions can be formed between a Sb coverage between zero and one monolayer. Among which, $(7\sqrt{3} \times 7\sqrt{3})$, $(5\sqrt{3} \times 5\sqrt{3})$, (2×1), and (2×2).[75,76,79] This goes to show that surface chemistry is to be investigated separately, knowledge from bulk studies cannot be readily applied. The stability of a surface reconstruction depends on the chemistry of the environment, and on the temperature. It is possible for different surface reconstructions to co-exist under given conditions, and one should be aware of how pure a certain surface reconstruction is.

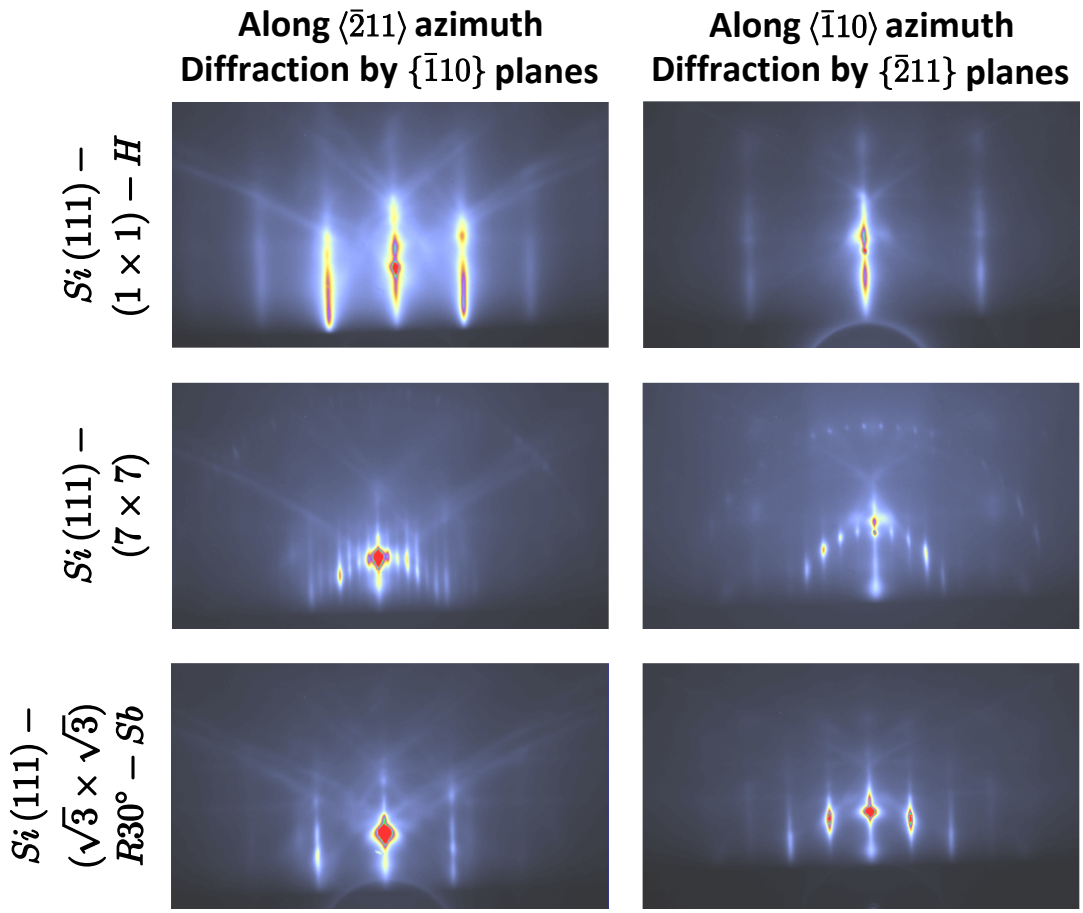

Figure 2.6: RHEED images along $\langle\bar{2}11\rangle$ and $\langle\bar{1}10\rangle$ azimuths, acquired on all three Si(111) reconstructions presented in this thesis; $(1\times1)-$H, (7×7), and $(\sqrt{3}\times\sqrt{3})R30°-$Sb.

3 Epitaxy of GeTe on Si(111)

In this chapter, the heteroepitaxy of GeTe thin films on Si(111) is explored, employing the three different surface reconstructions described in Chapter 2: $\mathrm{Si}(111)-(7\times7)$, $\mathrm{Si}(111)-(\sqrt{3}\times\sqrt{3})R30°-\mathrm{Sb}$, and $\mathrm{Si}(111)-(1\times1)-\mathrm{H}$. The two materials joined together are always the same; GeTe and silicon. Only the topmost atomic layers of the starting surface are different. And yet, the epitaxial relationships obtained in each case can differ radically, especially in the in-plane directions. Distinctions in the process by which growth is initiated are also encountered; in the very early stage of the deposition, the material can adopt structures and properties unexpected in a thicker film.

By understanding the differences between these surfaces, and by observing how GeTe interacts with them, fingerprints can be uncovered, left by the two main fundamental phenomena sculpting the structure of GeTe: Resonant bonding and Peierls distortions. The utmost importance of the surface reconstruction is highlighted, especially in the engineering of ultra-thin GeTe films of only few atomic layers. If the surface is not carefully chosen, the formation of the crystalline phase can be suppressed, preventing any kind of phase-change properties. Or, the film may not have the intended ferroelectric properties yet. With the support of the literature, these implications are extended to other resonantly bonded chalcogenide compounds, and their possible properties as thermoelectrics, ferroelectrics, or topological insulators.

3.1 In-plane epitaxial relationship

3.1.1 Twinned and twisted domains

Epitaxial growth of GeTe by MBE on a $\mathrm{Si}(111)-(7\times7)$ surface has first been demonstrated by Giussani *et al.*[80] In order to put the present work into its context, part of their results are first reproduced here. Furthermore, an explanation is offered for some of their uninterpreted findings, in light of more recent data. Despite the large lattice mis-

match of $\sim 7.9\,\%$, a single $\alpha-\mathrm{GeTe}[111]\,||\,\mathrm{Si}[111]$ out of plane relationship is achieved. For the in-plane relationship however, in addition to the $\alpha-\mathrm{GeTe}[\bar{2}11]\,||\,\mathrm{Si}[\bar{2}11]$ relationship, twinned and multiple twisted domains are observed, as illustrated by the $\varphi-$scan in Figure 3.1.

In-plane twinned domains can be recognized by the presence of peaks each 60° (red curve), while they are spaced by 120° in the silicon substrate (black curve). In fact, both GeTe and silicon are characterized by a 3-fold symmetry around the out-of-plane direction, and no twinned domain should in principle be expected. However, if the interaction between the material and the substrate at the interface is relatively weak, only the topmost atomic layer of the substrate, characterized by its $6mm$ point symmetry, dictates the epitaxial relationship and allows the formation of twins.[59] The intensities of the peaks from the twinned and non-twinned domains are very similar, showing that they are present in equal proportions in the thin-film, and equally favorable energetically.

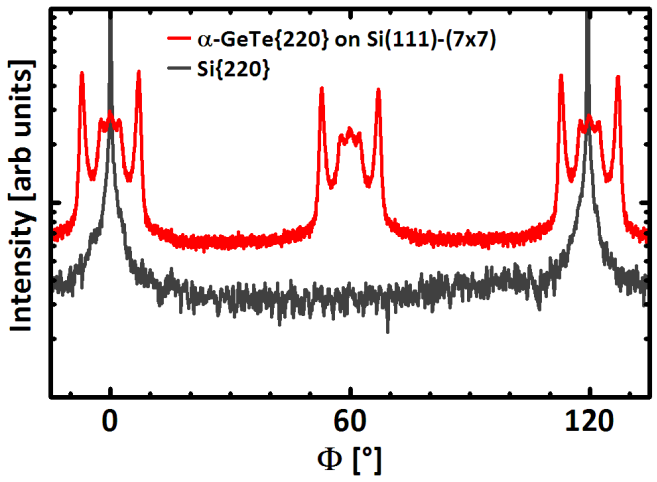

Figure 3.1: XRD $\varphi-$scan of a GeTe film grown on $\mathrm{Si}(111)-(7\times7)$ around the out-of-plane $\mathrm{Si}(111)$ direction scanning for the GeTe$\{220\}$ reflections. Substrate Si$\{220\}$ reflections are shown as a reference.

The presence of in-plane twisted domains is indicated by multiple peaks spread around the main peak aligned with the silicon substrate in the $\varphi-$scan (Figure 3.1). To investigate the volume occupied by the different domains, the angular spread around GeTe$\{220\}$ is fitted with five Lorentzian functions and shown in Figure 3.2. The exact fitting parameters are given in Table 3.1. From the area under the fit, $\pm2.3°$ domains (sum of the two peaks at $-2.3°$ and $+2.3°$) are 1.5 times more frequently formed than the non-twisted domains. As for the domains at $\pm7°$, they are found twice more frequently. The narrower width of the fit in these domains show that they also benefit from a higher texturing than the domains at $\pm2.3°$ and the non-twisted domains.

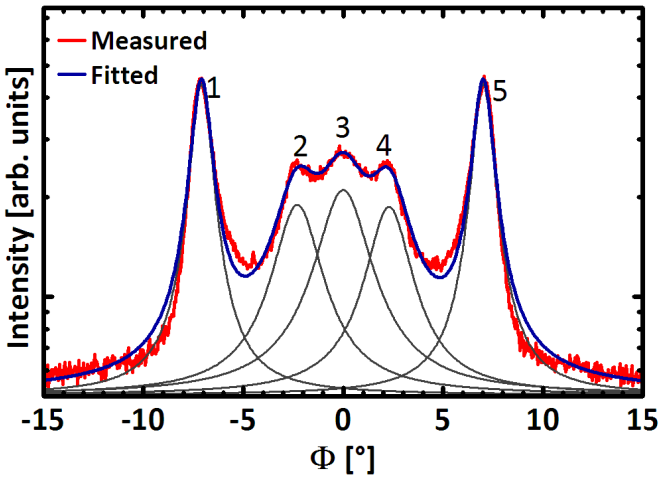

Figure 3.2: Detailed view around GeTe{220} and reflections from twisted domains. The fitted angular spread, in blue, is the sum of the five Lorentzian functions represented by the black curves.

	Center [°]	Width [°]	Area [-]
Lorentzian 1	−7	1.13	689.3
Lorentzian 2	−2.3	2.45	536.1
Lorentzian 3	0	2.72	683.6
Lorentzian 4	2.3	2.29	491.3
Lorentzian 5	7	1.12	683

Table 3.1: Fitting parameters used for fitting presented in Figure 3.2.

These highly favorable and better textured in-plane twisted domains can be explained by domain matched epitaxy.[35,60] Because of the large mismatch between the GeTe and Si surfaces, lattice matched epitaxy cannot be applied. In classical lattice matched epitaxy, relaxation occurs by the formation of dislocations once a critical thickness is reached, as approximated by (3.1),[81] with h_c the critical thickness, b the norm of one Burger vector, and f the lattice mismatch between film and substrate. Between GeTe and Si, the mismatch of 7.9 % is so large that the critical thickness is brought down to only 5 Å, to the order of few atomic layers. This approximation given by (3.1) is also known to overestimate h_c when the mismatch is larger than 4 %. Either way, misfit dislocations are generated and propagated immediately at the interface, epitaxial domains are formed, and (3.2) can be used to predict epitaxial rotation based on the lattice mismatch and Moiré pattern formed between the two surfaces.[82]

$$h_c \approx \frac{b}{9.9 \cdot f} \tag{3.1}$$

$$cos\theta = r_{AS} \cdot sin^2\Psi_S + cos\Psi_S \sqrt{1 - {r_{AS}}^2 \cdot sin^2\Psi_S} \tag{3.2}$$

In this expression, θ is the angle of twist of the rotated domain, r_{AS} is the ratio between absorbate and substrate lattice parameters, and Ψ_S corresponds to high-symmetry rotation angles of the Moiré pattern relative to the substrate lattice. With 3.84 Å and 4.17 Å for the $\{\bar{1}10\}$ in-plane lattice spacing for silicon and GeTe respectively, rotational angles $\theta = 2.6°$ and 7.1° are found for high symmetry angles $\Psi_S = 30°$ and 60°, which is in good agreement with the twisted domains observed experimentally.

To visualize the Moiré patterns created by the superposition of the GeTe film and the silicon surface, scale models are presented in Figure 3.3. The non-rotated surfaces are shown in (a). After offsetting the GeTe and the silicon surfaces by $\theta = 2.6°$ and 7°, Moiré patterns are revealed, with coincidence nodes along a cell that is rotated by $\Psi_S = 30°$ and 60° respectively (b and c), as expected from Equation 3.2. Depending on the angle of rotation, the Moiré patterns also have different densities of coincidence points. And it seems that the most favorable domains rotated by 7°, also possess the highest density of coincidence points.

Although the domain mismatch between coincidence points is minimal compared with the lattice mismatch between the two materials, there is still always some residual strain. With this in mind, the domain mismatch between coincidence points can be calculated,

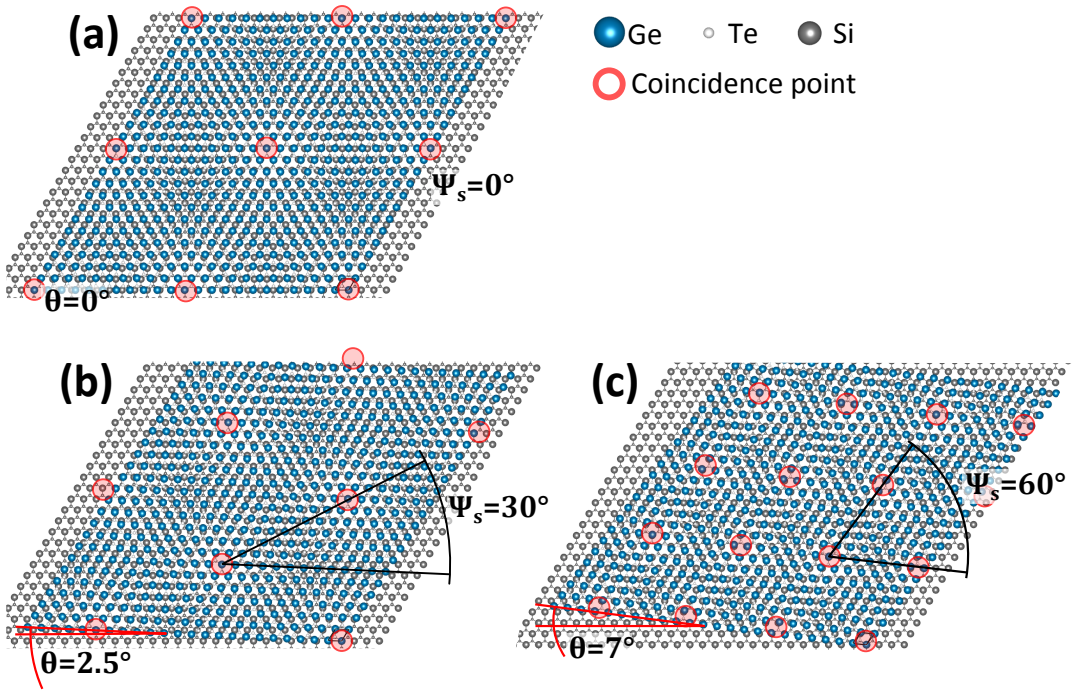

Figure 3.3: Moiré patterns appearing from the superposition of a $\alpha-$GeTe(0001) surface on Si$(111)-(1\times1)$ without rotation, (a) rotated by 2.5°, (b) and rotated by 7°. (c) (All stuctural models have been created using VESTA [83])

as illustrated in Figure 3.4 (a). Here, the domain mismatch is considered between an integer number $n-1$ of GeTe unit cells and the distance to a point in the Si lattice with coordinates (n,k), where n and k are the number of Si unit cells in a and b directions. By fixing $k=1$, a minimum mismatch of 0.14 % is found at $n=19$ in Figure 3.4 (b), which corresponds to a rotation of 2.6° (Figure 3.4 (c)). There is then a distance of 18 GeTe unit cells between two coincidence points $(n-1)$. Similarly, by fixing $k=2$, a minimum mismatch of 0.07 % is found at $n=14$, corresponding to a rotation of 7.1° (Figure 3.4 (d) and (e)), with a distance of 13 GeTe unit cells between two coincidence points. Therefore, the angular twist of 7° which yields the most favorable domains, also coincides with the smallest domain mismatch.

Finally, the growth of GeTe on the Si$(111)-(7\times7)$ surface can be compared with the growth of Sb_2Te_3 on the same surface. In the case of Sb_2Te_3, the formation of in-plane twisted domains is also observed, but the rotated domains occur at angles that match coincidence points with the dangling bonds of the Si$(111)-(7\times7)$ surface,[84] whereas GeTe finds coincidence domains with the unreconstructed Si$(111)-(1\times1)$ surface. This difference resides in that Sb_2Te_3 is a 2D material with covalently bonded quintuple atomic layers (QLs) held together by vdW forces, while GeTe is more commonly considered as a 3D-bonded material. When Sb_2Te_3 is deposited on the Si$(111)-(7\times7)$ surface, the surface reconstruction remains unaltered, only the dangling bonds are able to interact

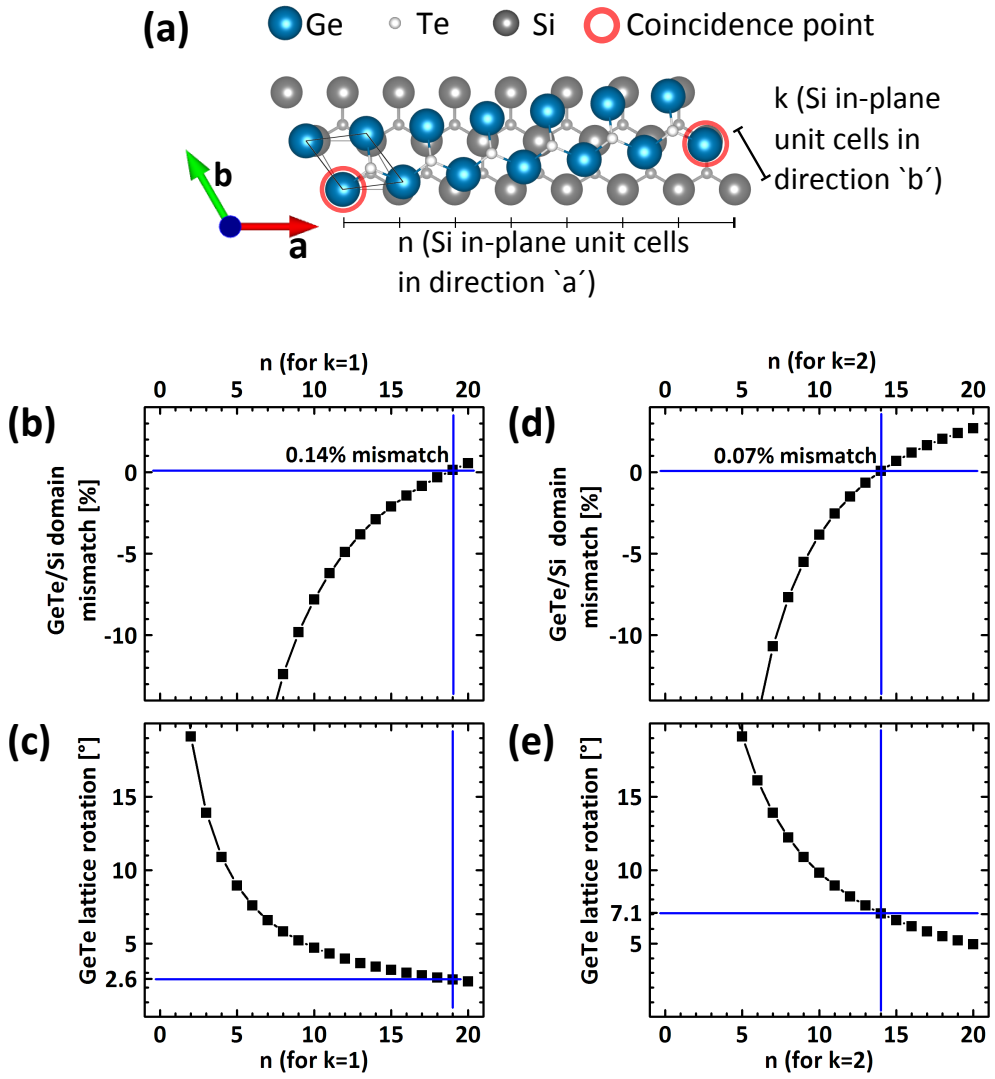

Figure 3.4: Schematic representation of a GeTe layer on top of a Si(111) substrate. n and k correspond to the number of Si unit cells in a and b directions. (a) Coincidence lattice mismatch and rotation as a function of n, with $k = 1$, (b and c) and with $k = 2$. (d and e)

with the weakly bonded film; they thus dictate the angles at which the in-plane twisted domains occur. As for GeTe grown on the $Si(111)-(7\times7)$ surface, the 3D material has a stronger interaction with the surface atoms, the reconstruction is lost when it is covered by GeTe. This interaction at the interface is clearly stronger than vdW interactions of 2D materials, but it is still weak enough for the formation of twinned domains.

3.1.2 Single in-plane orientation for GeTe on passivated Si(111)

In the case of Sb_2Te_3, it has been demonstrated that twisted domains could be suppressed by growing on the Sb terminated $Si(111)-(\sqrt{3}\times\sqrt{3})R30°-Sb$ surface instead of the $Si(111)-(7\times7)$.[84] Interestingly, although GeTe and Sb_2Te_3 have quite different structures, twisted domains are also suppressed in GeTe using the same stategy.[35] This is demonstrated by the XRD $\varphi-$scan presented in Figure 3.5 (a): Instead of several reflections grouped together, only one single peak is measured (blue curve). In order to discriminate the role of the surface passivation from an eventual interaction between GeTe and the Sb involved in the $Si(111)-(\sqrt{3}\times\sqrt{3})R30°-Sb$ surface preparation, the growth of GeTe on the $Si(111)-(1\times1)-H$ surface is investigated. This surface is also fully passivated, but does not involve any Sb in its preparation. Figure 3.5 (b) shows that twisted domains are suppressed on this passivated surface as well (red curve), demonstrating that the presence of Sb is not a necessity, the full passivation seems to be responsible for the improved epitaxial relationship instead.

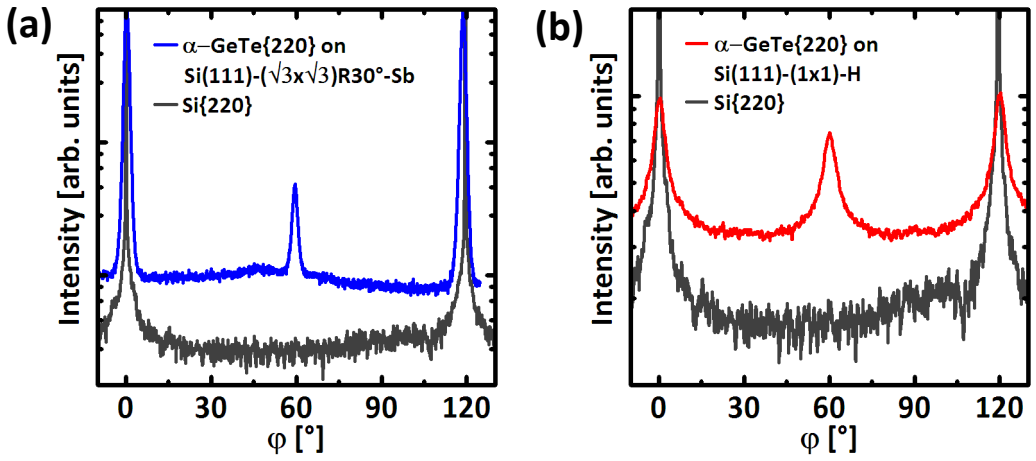

Figure 3.5: XRD $\varphi-$scan aligned on the GeTe{220} reflections, for a GeTe film grown on $Si(111)-(\sqrt{3}\times\sqrt{3})R30°-Sb$ (a) and $Si(111)-(1\times1)-H$ (b). Substrate Si{220} reflections are shown as a reference.

On a passivated surface, a 2D material such as Sb_2Te_3 is only weakly bound by vdW forces, and the epitaxial registry is dictated by vdW epitaxy.[84,85] Because the formation of twisted domains is a strain relaxation process, it is no longer needed when the influence of the substrate lattice is drastically weakened. The epitaxial relationship is then mainly guided by the symmetry of the substrate.

In contrast, regardless of the substrate passivation, a cleaved GeTe surface is expected to leave dangling bonds at the interface, which would in principle prevent vdW epitaxy. However, because GeTe is resonantly bonded, the p orbitals are shared between two lobes at opposite sides of the atom. Therefore, the dangling bonds are much weaker for a resonantly bonded material than for a covalent material. In addition, these resonant bonds are also less rigid, both in their orientation and length compared to covalent bonds. These p orbitals are also asymmetric because of Peierls distortion, with one shorter lobe of higher electron density and one longer lobe of lower density.[86] This could also play a role in the epitaxial registry of GeTe on silicon as well: By pointing the longer weaker lobes toward the interface, GeTe can further minimize the interaction with the passivated surface and mimic vdW epitaxy.

A major difference between GeTe and Sb_2Te_3 on the $Si(111)-(\sqrt{3}\times\sqrt{3})R30°-Sb$ surface is that twinning is reduced in the case of GeTe while it is always present in Sb_2Te_3. The two materials must however be compared carefully, as twins are only expected to form at the interface in the case of GeTe, whereas they can potentially occur both at the interface and within the film at each vdW gap for Sb_2Te_3. Would the twinned domains be suppressed at the interface for Sb_2Te_3, they could be formed again later in the film. An XRD $\varphi-$scan on one single QL would be necessary to assess the formation of twins specifically at the interface. For an experiment on such a thin film, only synchrotron radiation has a chance to provide enough intensity contrast between the peaks and the background.

But for GeTe, by fitting the $\varphi-$scan reflections in Figure 3.5 (a) with a single Lorentzian, the peaks aligned with the silicon reflections have an area under the curve 20 times larger than the reflections from the twinned domains; the twinned domains are suppressed down to 5 % of the volume of the film. At first, a suppression of twinning could indicate a stronger interaction with the deeper atomic layers of the substrate, but this explanation is unlikely; the surface being fully passivated, the interaction with the surface should only be weaker. Another possible explanation could be that the topmost Sb atoms terminating the surface are arranged in a 3-fold symmetric configuration,[77] negating the formation

of twins. The remaining possibility is that GeTe reacts with the Sb atoms terminating the surface, the resulting GST compound could in turn have a stronger interaction with the substrate surface, suppressing the twinned domains.

Concerning the likelihood for intermixing to occur, there are arguments weighting on both sides of the balance: The terminating Sb atoms are covalently bound to the silicon surface and also among themselves,[77] and are not expected to be easily removed. The fact that a temperature of 650 °C has to be reached in order to desorb the Sb atoms passivating the surface stands witness to the strength of these bonds.[76] Therefore, the reaction with Sb has to be favorable enough to overcome this large energy barrier. On the other hand, Sb is known to be surfactant for the growth of pure Ge.[57] These results can only be cautiously translated into the present system that contains a large amount of Te in addition, which completely changes the energy landscape.

However, all these conjectures don't explain why the ratio of twinning is also slightly reduced on the $Si(111)-(1\times1)-H$ surface, as shown in Figure 3.5 (b). Here no Sb is involved, and the topmost surface still has a $6mm$ symmetry. From the integrated intensity of the peaks, the film contains 42 % twinned domains. Evidently, the quality of GeTe grown on the H-terminated surface is lower compared to GeTe grown on the Sb-terminated surface. The reflections are much broader, showing that there is more angular dispersion. (Width of 5° versus 1.2° on the Sb-terminated surface) The weaker texturing and the slight suppression of twinned domains could be caused by some imperfections in the surface reconstruction, providing sporadic anchor points between the film and the substrate. This hypothesis could of course also be applied to the Sb passivated surface, but to a lesser extent, given the much higher quality obtained.

To further illustrate the strong in-plane epitaxial relationship achieved, atomic force microscopy (AFM) images of GeTe layers grown on $Si(111)-(7\times7)$ and $Si(111)-(\sqrt{3}\times\sqrt{3})R30°-$Sb are compared in Figure 3.6. Both samples are grown at a substrate temperature of 250 °C, to a thickness of 60 nm. On $Si(111)-(7\times7)$, GeTe yields a surface with RMS roughness of $3-4\,nm$ that appears to be formed by the coalescence of $150-300\,nm$ large islands with triangular profiles. Some of these islands can protrude $2-10\,nm$ above the flatter parts of the surface, depressions of about the same heights are also observed.

With the $Si(111)-(\sqrt{3}\times\sqrt{3})R30°-$Sb surface, the protruding islands are greatly suppressed, lowering the RMS roughness down to 0.8 nm. Most noticeably, the triangular islands all share the same in-plane orientation, their size is increased up to $400-600\,nm$. Aligned with the islands, a network of straight lines can also be observed. These lines could originate from a preferential deposition occuring at the step edges or at the bound-

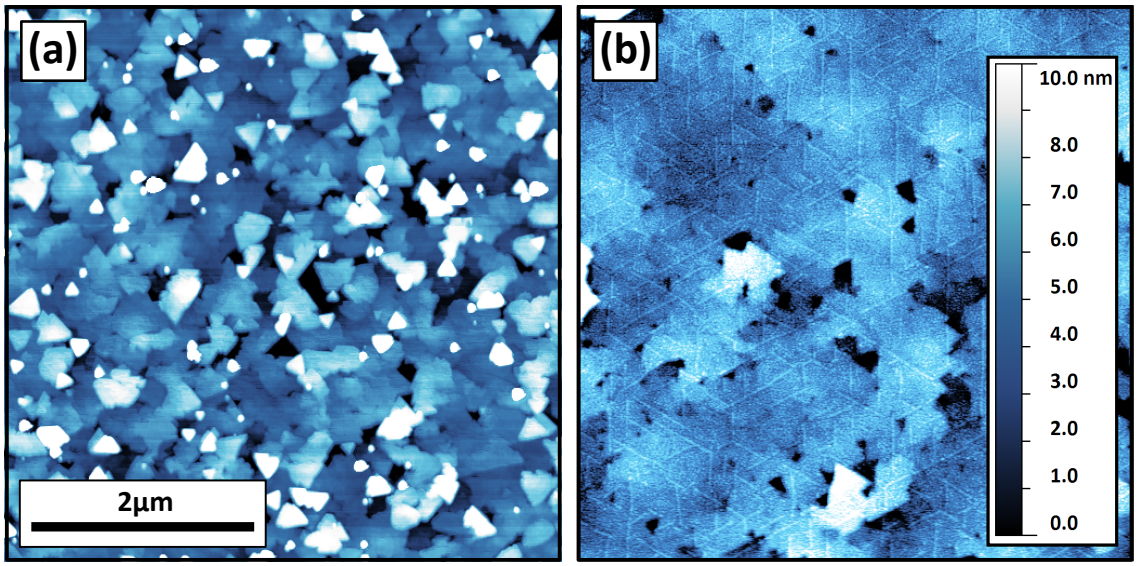

Figure 3.6: Comparison between AFM images acquired on $60\,nm$ thick GeTe films grown on $Si(111)-(7\times7)$ (a), and $Si(111)-(\sqrt{3}\times\sqrt{3})R30°-Sb$ (b).

ary between two coalescing islands. Further studies are necessary to understand the origin and nature of these lines, they have never been observed for the growth of GeTe on $Si(111)-(7\times7)$.

Despite the great improvements achieved, the surface is still plagued by the presence of triangularly shaped depressions. For technological applications, a perfectly flat surface would certainly be more desirable. And also for characterization methods such as piezo-force microscopy (PFM), where the probing tip is dragged across the surface in direct contact with the material, depressions such as these will inevitably damage the probe. In an effort to suppress the formation of these depressions, the pre-deposition of Ge before growth onset has been investigated.

Once the $Si(111)-(\sqrt{3}\times\sqrt{3})R30°-Sb$ reconstruction is obtained and the intended substrate temperature is reached, the shutter to the Ge cell is opened and the substrate is exposed to an impinging flux of germanium during up to 120 seconds. The Te cell shutter is then opened as well, and the growth of GeTe proceeds normally. This additional step has been shown to reduce the size of the depressions, the area they occupy in the film, and their average depth as well. Three AFM images acquired on GeTe films grown on $Si(111)-(\sqrt{3}\times\sqrt{3})R30°-Sb$ after Ge pre-depositions of 15, 30, and 60 seconds are presented in Figure 3.7 (a), (b), and (c), with the depressions marked in red.

Interestingly, these triangular depressions often appear to be rotated by 180° with respect to the triangular islands. Thus it is suspected that there could be a link between them and the twinned domains, where the same rotation is expected. In order to investigate this

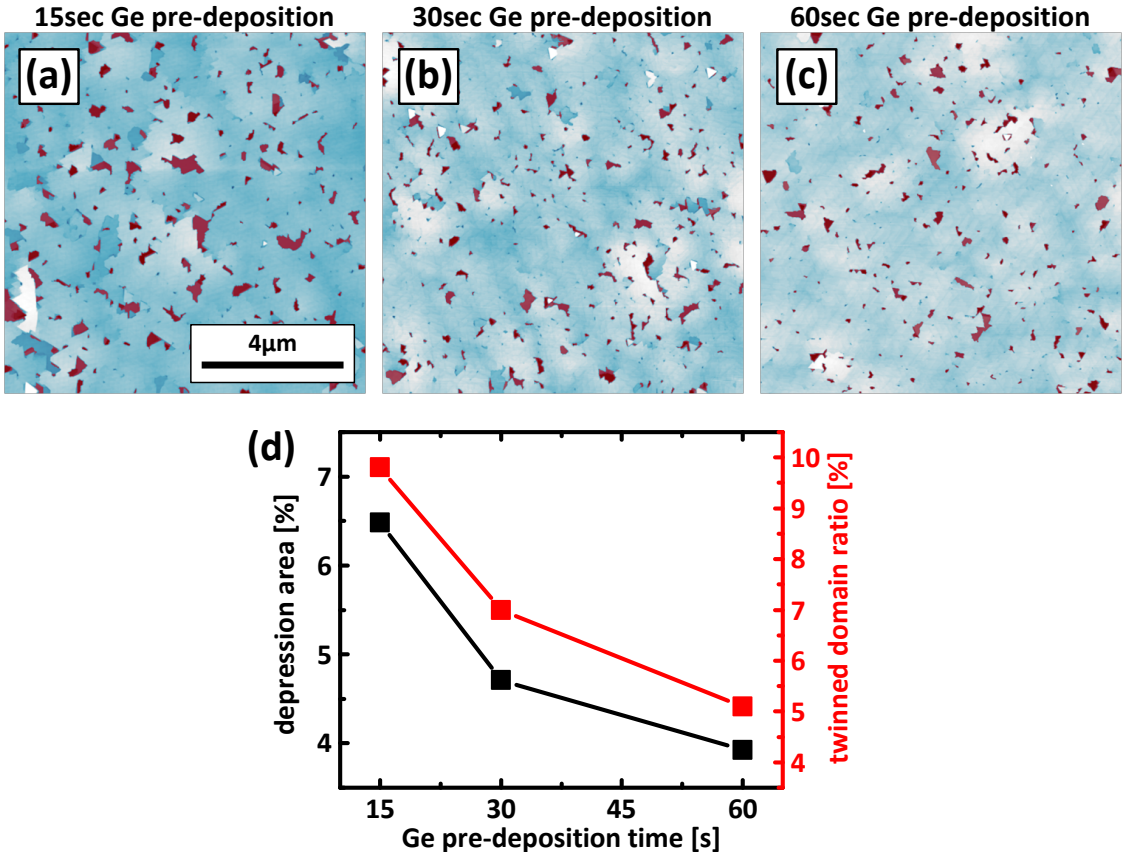

Figure 3.7: Comparison between AFM images of three 30 nm thick GeTe films on $Si(111)-(\sqrt{3}\times\sqrt{3})R30°-Sb$, grown with 15 (a), 30 (b), and 60 seconds (c) of Ge pre-deposition, the surface depressions are highlighted in red. (d) The relative area covered by the depressions and the ratio of twinned domain obtained from XRD $\varphi-$scans are plotted versus Ge pre-deposition time.

possible correlation, XRD $\varphi-$scans are performed on these GeTe samples grown after Ge pre-deposition. The proportion of twinned domains is again calculated from the ratio between the integrated intensity of the reflections from the twinned and non-twinned domains. And indeed, within the same series of experiments, a correlation can be observed, as shown in Figure 3.7 (d). As the area occupied by the depression decreased, the ratio of twinned domains decreased as well. The triangular depressions could have been left behind from the partial overgrowth of energetically less favorable twinned domains.

Unfortunately, the full suppression of these depressions could not be achieved simply by increasing the Ge pre-deposition time. With 120 seconds, a roughening of the surface is observed and the proportion of triangular depressions increases again. The formation of twinned domains in GeTe seems to be very sensitive to the surface conditions, and some dispersion in the results can be encountered, depending on the cleanness of the substrate, the quality of the surface reconstruction, and the ratio between Ge and Te fluxes.

It has been later observed that lowering the substrate temperature from 260°C down to 230°C can also yield films where the depressions are suppressed, but the ratio of twinning is not lowered as much. So these two values are not correlated anymore. An AFM image and $\varphi-$scan on such a GeTe film are shown in Figure 3.8 (a) and (b). The depressions only occupied 3 % of the surface, while the intensity of reflections from the twinned domains remained as high as 30 %. This could mean that the energetic difference between twinned and non-twinned domains is only exacerbated at high temperature. The twinned domains are able to compete with the non-twinned ones at low temperature, they grow almost equally quickly. If the objective is not to specifically suppress twinning, but simply to obtain a better surface quality, lowering the substrate temperature can be an easy and efficient method. There is however a lower limit in the growth window, where the film risks entering a polycrystalline or amorphous form. It has been found that this risk was increased when Ge pre-deposition is attempted with this lower temperature.

These improvements in surface quality and in-plane texturing make MBE grown films the best platform for the investigation of ferroelectric properties of GeTe. Despite screening of charges by the rather high concentration of bulk carriers $n_p \approx 10^{20}\, cm^{-3}$, ferroelectric switching by piezo-force microscopy is achieved on these films.[26] The strong suppression of rotational domains also enables the acquisition of clearer angle-resolved photoemission spectroscopy (ARPES) data that can be interpreted more confidently. These data are paramount in the characterization of Rashba spin splitting, in particular to validate the predicted dependency of the Rashba effect in GeTe on its ferroelectric polarization.[30]

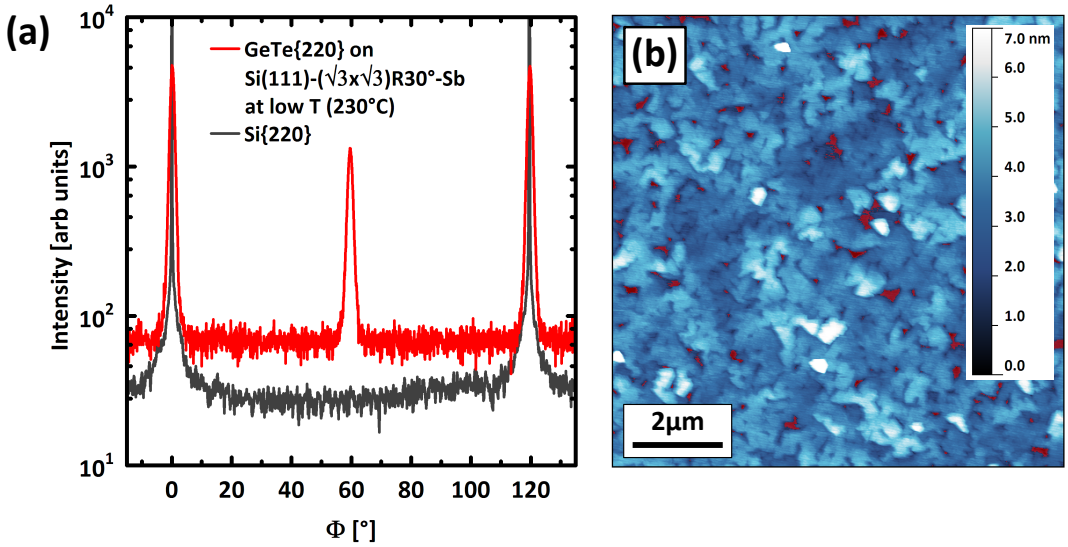

Figure 3.8: (a) XRD $\varphi-$scan aligned on the GeTe$\{220\}$ reflections, for a GeTe film grown on $Si(111)-(\sqrt{3}\times\sqrt{3})R30°-Sb$ at a substrate temperature of 230°C. (b) AFM image on the same 45 nm thick GeTe film (Depressions highlighted in red).

3.2 Out-of-plane epitaxial relationship

When GeTe was first grown on $Si(111)-(7\times7)$, a very strong $\alpha-GeTe[111]\,||\,Si[111]$ out-of-plane epitaxial relationship was achieved. In this respect, growth on passivated surfaces did not improve the already very good texturing in the growth direction. Nevertheless, the out-of-plane reflections in XRD are interesting to investigate for the insights they offer on the structure of the material. A symmetric $\omega-2\theta$ XRD scan along the $Si(111)$ specular rod is shown in Figure 3.9 (a), scanning for the out-of-plane reflections. The angle is converted into reciprocal lattice units using (3.3), an unit independent of the wavelength of the probing radiation. In addition to the sharp peaks from the silicon substrate at Q_z = 2.00, 4.00, and 6.01 Å^{-1}, three Bragg reflections are measured at Q_z = 1.77, 3.54, and 5.31 Å^{-1}, corresponding to the $\alpha-GeTe(111)$, (222), and (333) reflections. From these reflections, an out-of-plane lattice parameter of 3.55 Å is calculated, which is in good agreement with literature.[23] Independently of the surface passivation, the out-of-plane GeTe peaks are always asymmetric, with a shoulder at higher Q_z values. To better understand the origin of this shoulder, a XRD reciprocal space map (RSM) is acquired around the $GeTe(222)$ reflection and presented in Figure 3.9 (b).

$$Q_z = (4\pi/\lambda)\times sin(\theta) \tag{3.3}$$

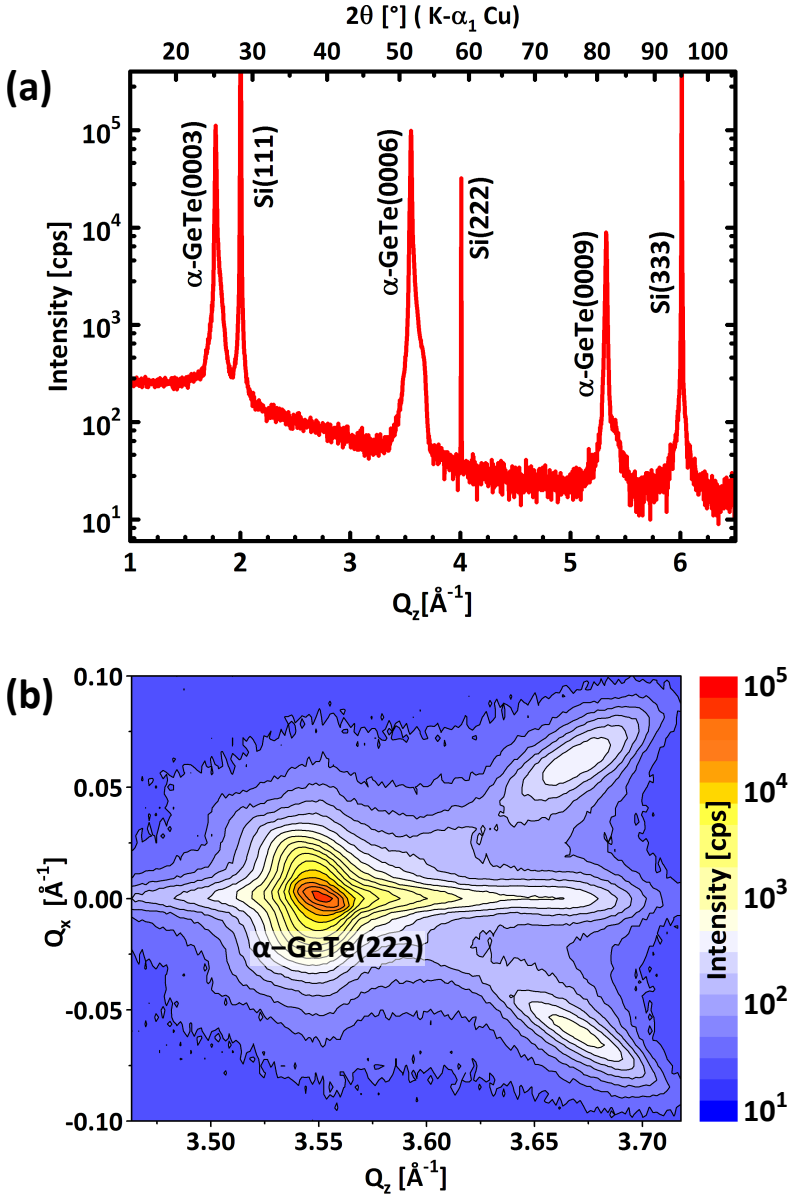

Figure 3.9: (a) Symmetric $\omega - 2\theta$ XRD scan along the Si(111) specular rod for a GeTe film grown on Si(111) $-$ $(\sqrt{3} \times \sqrt{3})R30° -$ Sb. (b) Reciprocal space map around the GeTe(222) reflection with Q_x along the $[\bar{1}10]$ direction.

What appears to be a shoulder in the $\omega - 2\theta$ scan is in fact a three-fold split peak at $Q_z = 3.67\,\text{Å}^{-1}$, which corresponds in real space to lattice planes spaced by 3.425 Å. This indicates the presence of some domains where the rhombohedral distortion did not occur in the out of plane direction, but following one of the oblique $\langle \bar{1}11 \rangle$ directions. Judging from the intensity of the peaks, these domains only occupy 2−4 % of the volume of the film. The splitting of the peaks in Q_x indicates that an angle is formed to accommodate the mis-oriented domains. A scale model is shown in Figure 3.10 to illustrate how the different directions of distortion and how the domains would fit with each other. A different axis of rhombohedral distortion also implies that the ferroelectric polarization in these domains will follow this alternative direction. And because these domains are only sparsely observed, this demonstrates that the MBE grown film possesses one single dominant axis of polarization along the growth direction.

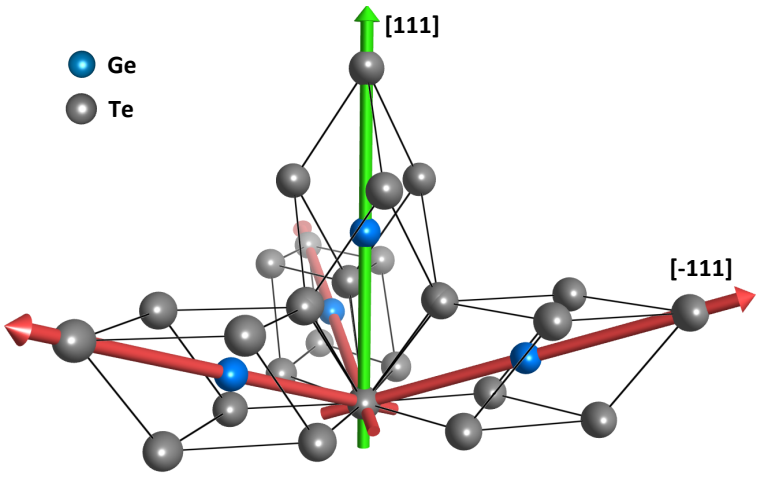

Figure 3.10: Scale model of α−GeTe crystal distorted along [111] direction (green), with the three other possible directions of distortion along $\langle \bar{1}11 \rangle$ (red). (The directions are given for a cubic crystal system, while the cells represented are rhombohedral for visual clarity.)

Using the Williamson-Hall method, the size of the grains and residual strain in the film can be assessed from the broadening they cause in the successive out-of-plane Bragg reflections.[87] As shown in Figure 3.11, the full-width at half maximum (FWHM) of the GeTe(111), (222), and (333) reflections are measured in the symmetric $\omega - 2\theta$ and ω rocking-curve configurations (in blue and red respectively). The axis are converted into reciprocal space units Q_z, ΔQ_z and ΔQ_x are calculated using the expressions (3.4) and (3.5)[88]. By fitting linearly the values measured, the slope of the fit provides information about the strain in the film, and size of the grains can simply be measured by calculating the inverse of ΔQ at the intercept. In the present case, both slopes are extremely shallow, demonstrating that there is no significant strain effect and that the film is relaxed. The

intercept for ΔQ_z indicates that the grains are 60 nm large in the out-of-plane direction, which corresponds to the full thickness of the film. The intercept for ΔQ_x is zero, which means that the size of the grains in-plane is large enough so that no size effect is observed.

$$\Delta Q_z = (4\pi/\lambda) \times \left[sin\left(\theta + \frac{FWHM_{\omega-2\theta}}{2}\right) - sin\left(\theta - \frac{FWHM_{\omega-2\theta}}{2}\right)\right] \tag{3.4}$$

$$\Delta Q_x = (4\pi/\lambda) \times \left[cos\left(\theta + \frac{FWHM_{\omega-scan}}{2}\right) - cos\left(\theta - \frac{FWHM_{\omega-scan}}{2}\right)\right] \tag{3.5}$$

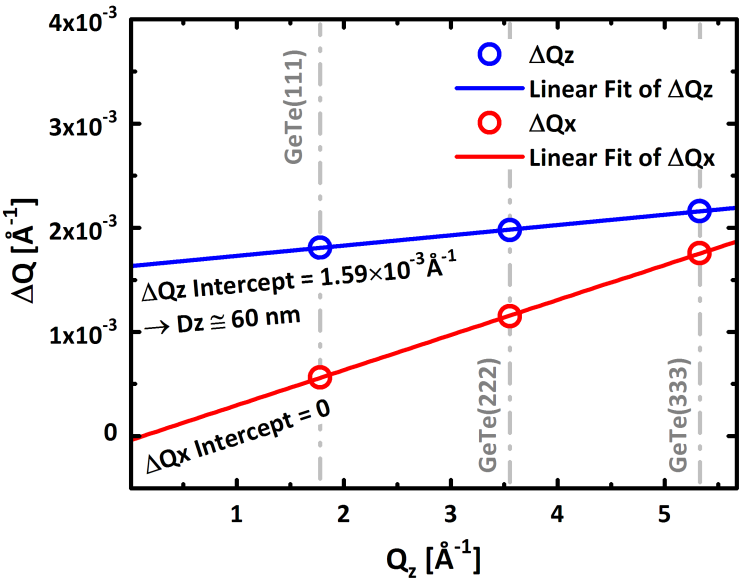

Figure 3.11: Williamson-Hall analysis on the GeTe(111), (222), and (333) reflections, both in Q_z (blue), and Q_x (red).

3.3 Growth onset phenomena

3.3.1 Amorphous to crystalline transition at growth onset

Already previously, in the case of GeTe grown on Si$(111) - (7 \times 7)$ by MBE,[80] or GST grown on GaSb(001),[89] RHEED monitoring revealed an interesting phenomenon: Right at the beginning of the growth, the sharp substrate streaks fade out into a diffusely scattered intensity, which seems to indicate that the deposition does not start with the growth of the intended crystalline layer, but by the deposition of an amorphous layer instead.

Only after a certain thickness is reached, crystalline streaks appear again in RHEED. Surprisingly, despite this initial transition into the amorphous phase, the film is able to find a strong domain matched epitaxial relationship with the substrate, as discussed in the previous section.

In literature, similar transitions have also been observed in other resonantly bonded materials. For instance in quench condensed Bi on $Si(111)$ [90] and Sb on glass,[91] the material first condenses into an amorphous phase and then spontaneously crystallizes after a certain thickness is reached. Low energy diffraction (LEED) experiments performed at the growth onset of Bi_2Se_3 on a Bi-passivated $Si(111)$ surface reveals that the crystalline streaks only appear after a thickness of $0.38\,nm$ is reached.[92] In a study dedicated to the effect of strain on the crystallization temperature of amorphous GST thin films constrained within claddings, Simpson *et al.* also suggested that there is a minimal thickness for crystallization. Finally, similar observations were reported for Gd_2O_3 on Si(111),[93] an ionic material that is not resonantly bonded, showing that the present discussion also concerns other classes of materials. Nevertheless, The unique implication for phase change materials is that there could be a minimal thickness for the resonantly bonded crystalline phase to exist, a minimal thickness below which switching is not possible. Such a limitation also has important implication for resonantly bonded thermoelectrics,[94] ferroelectrics,[26] and topological insulators,[12] properties that are only manifested within an ordered crystal.

The good news is that this issue is not intrinsic to the materials, this limitation can be circumvented. Both for GST on the $Si(111)-(7\times7)$ surface,[95] and GeTe on $Si(111)-(\sqrt{3}\times\sqrt{3})R30°-Sb$,[35] no such amorphous transition is observed, growth of crystalline GeTe is reported immediately at the beginning of the growth. This is shown in Figure 3.12 (a)−(d) by a series of RHEED snapshots during growth, both along the $Si\langle\bar{1}10\rangle$ and $Si\langle\bar{2}11\rangle$ azimuths. As soon as the deposition starts, new streaks from GeTe appear immediately, while the streaks from the silicon substrate fade out completely within the first 10 seconds. The fact that these streaks have an uniform intensity along their length shows that the film is flat and smooth.

In an attempt to further investigate the epitaxy of GeTe on passivated surfaces, growth is performed with identical parameters on the $Si(111)-(1\times1)-H$ surface as a comparison. The growth is illustrated in Figure 3.13 (a) with three RHEED images along the $\langle\bar{1}10\rangle$ azimuth acquired at different stages during growth. In Figure 3.13 (b) the RHEED intensity at the position of the $GeTe(111)-(1\times1)$ streaks is plotted as a function of the thickness during growth. Surprisingly, an amorphous transition at growth onset is observed, just as on the 7×7 non-passivated surface.

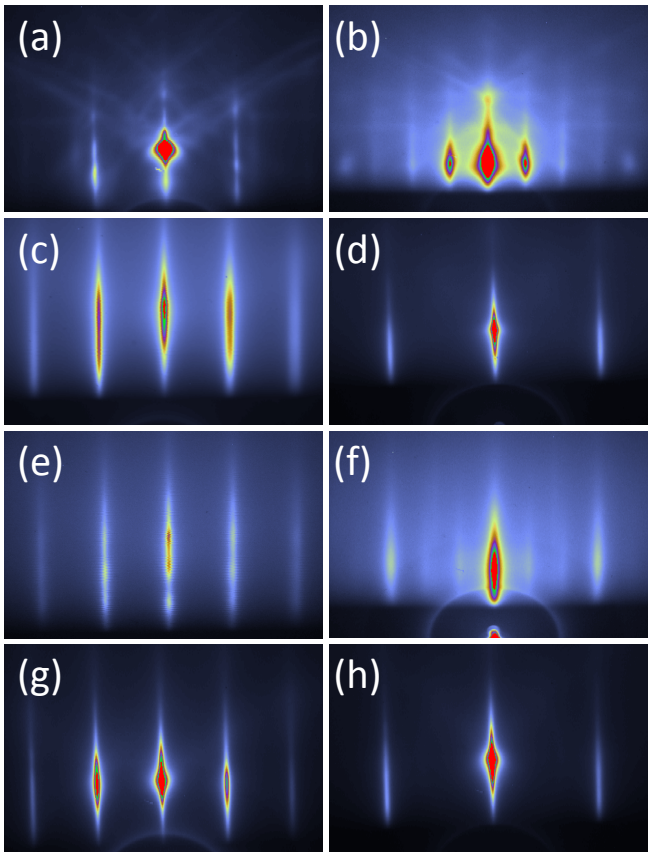

Figure 3.12: RHEED images perpendicular to the Si$\langle\bar{1}10\rangle$ and Si$\langle\bar{2}11\rangle$ azimuths of the Si$(111) - (\sqrt{3} \times \sqrt{3})R30° -$ Sb surface before growth (a and b), during the first 60 seconds of deposition (c and d), from 60 to 600 seconds (e and f), and GeTe$(111) - (1 \times 1)$ surface at the end of growth, after 2 hours (g and h).

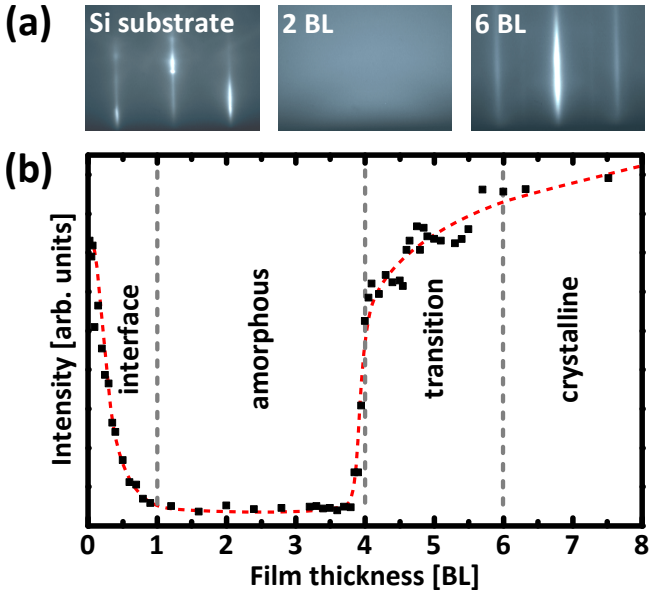

Figure 3.13: (a) RHEED images along Si$\langle\bar{1}10\rangle$ azimuth during growth of GeTe on Si$(111)-(1\times1)-$H surface before deposition, right after the start, and later during growth. (b) Relative RHEED intensity at expected Q_x position for GeTe$(111)-(1\times1)$ streaks monitored during growth.

At the beginning of growth, intensity is measured from the Si$(111)-(1\times1)-$H substrate. Within the deposition of the first GeTe bilayer (BL), the substrate streaks fade out, leaving a diffuse scattered intensity typical of an amorphous phase. After the deposition of 4 BLs, new streaks corresponding to a GeTe$(111)-(1\times1)$ surface appear and remain until the end of the growth at a thickness of $\sim 30\,nm$. As soon as the streaks appear, their spacing already correspond to the expected in-plane lattice spacing for $\alpha-$GeTe, which indicates that the film is relaxed. In this figure, the growth rate is derived from the final thickness of the film measured by XRR. This demonstrates that the passivation specifically by Sb plays an important role in the suppression of the amorphous transition in GeTe. While surface passivation in general could still be a factor tipping the thermodynamic balance, it does not seem to be a sufficient condition in this case.

To demonstrate that the changes observed in RHEED are truly linked to a phase transition, GeTe films of a few atomic layers are grown on the Si$(111)-(1\times1)-$H surface and investigated by Raman spectroscopy. Samples with nominal thickness of 2 and 4 BLs were prepared, where the growth is interrupted while the RHEED pattern still showed no crystalline streaks. Other samples are grown until the RHEED streaks appeared, at nominal thicknesses of 6 and 8 BLs. Raman spectroscopy is then performed on these thin samples, as it is proven to be a insightful technique for the investigation of graphene,[96] and very thin layers of 2D materials like WSe_2.[97] The measurements are acquired in $z\,(y,xy)\,\bar{z}$ geometry with a $633\,nm$ laser, and shown in Figure 3.14 For each sample, the

Raman spectrum is accompanied with a RHEED image, acquired at the end of the corresponding growth. In all cases, as the growth is interrupted, the RHEED patterns remain unchanged, demonstrating that all these very thin layers are stable, both before and after the amorphous to crystalline transition.

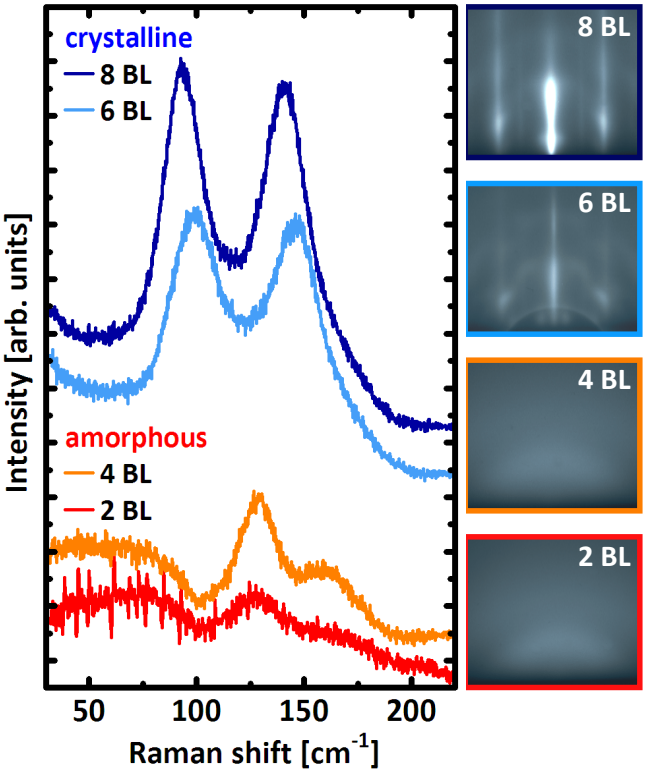

Figure 3.14: Raman spectra acquired on GeTe samples of 2, 4, 6 and 8 BLs nominal thickness grown on the $Si(111) - (1 \times 1) - H$ surface. For each sample, a RHEED image acquired at the end of the growth is shown.

For the two thicker samples (8 and 6 BLs), two modes of similar intensity can be identified at 94 and 140.3 cm^{-1} for the 8 BL sample, 99.6 and 144.6 cm^{-1} for the 6 BL sample. These modes are attributed to the $(E1)$ and (A) modes at 83 and 123 cm^{-1} observed in a 30 nm thick crystalline $\alpha-$GeTe reference. A progressive mode strengthening is observed in the ultra-thin samples, this shift is ascribed to the reduced thickness of the film. Interfacial layers in fact occupy a larger proportion than bulk and are expected to impact the phonon behavior of the crystalline film.[98]

As for the 2 thinner samples (4 and 2 BLs), two peaks with an intensity ratio of about 2/3 are observed at 128.6 and 156.2 cm^{-1} for the 4 BL sample, 127.4 and 163.3 cm^{-1} for the 2 BL sample. The intensity ratio of the two modes and the spacing between them differ clearly from the two thicker crystalline samples. Instead, these modes match very well with literature values for amorphous GeTe modes at 125 and 160 cm^{-1}.[99] In addition,

the presence of a Bose peak near the $50\,cm^{-1}$ range also indicates a strong contribution from an amorphous material.[100] This shows that an amorphous GeTe layer is indeed deposited on the surface during the first stage of the growth. As a side note, it is usually quite unexpected for semiconductor materials to have such different Raman spectra between their amorphous and crystalline phases. Only the fundamental change in the bonding nature of PCMs between the covalent amorphous and the resonant crystalline phase can produce such large differences in the phonon modes, and this Raman contrast can be recognized as a characteristic of PCMs. The clear transition between the 4 BL and 6 BL samples shows that the entire film undergoes an amorphous to crystalline transition. After switching, neither Bose peak nor modes of the amorphous GeTe are observed, ruling out the possibility for parts of the film to remain amorphous, or to have crystalline material only on top of a subsisting amorphous layer.

The amorphous transition at growth onset can be trivially explained in terms of interface energies unfavorable to the crystalline phase being gradually overpowered by free energy coming from the increasing volume of the film. The crystalline phase is the more stable phase, so given enough energy, it will always be the phase favored in the bulk. But this is not necessarily true in an ultra-thin film dominated by its interfacial energy. Now the real interest resides in the identification of the main factors ruling the interfacial energy between crystalline GeTe and the substrate.

Foremost, the principle of resonant bonding is based on an advantageous superposition of two virtual states ($\Psi 1$ and $\Psi 2$) that are energetically equivalent,[101] as illustrated in Figure 3.15. It is known that equivalence between the superimposed configurations does not need to be perfect for resonant bonding to occur, as demonstrated simply by the fact that Peierls distortions and resonant bonding both co-exist in GeTe despite being in competition with each other.[19] But a strong distortion will still accentuate the difference between $\Psi 1$ and $\Psi 2$ and weaken the resonant nature of the bonds, up to a point where they are not favorable anymore. In an ultra-thin film of only a few atomic layers, the bonds at the surface and interface clearly differ from the bonds in the film, $\Psi 1$ and $\Psi 2$ are clearly not equivalent. Resonant bonds are therefore more sensitive to the interface compared to ionic or covalent bonds. The necessity for a certain long range order and a favorable geometric arrangement make resonant bonding less likely to be expressed in an ultra-thin film.[101]

Furthermore, considering the 8-N octet rule, the silicon is 4-fold covalently bonded while crystalline GeTe is 3-fold resonantly bonded. Because of this electronic mismatch between the two materials, a high interfacial energy is expected. On the other hand, amorphous GeTe is also mostly in a 4-fold covalently bonded configuration,[102] offering a

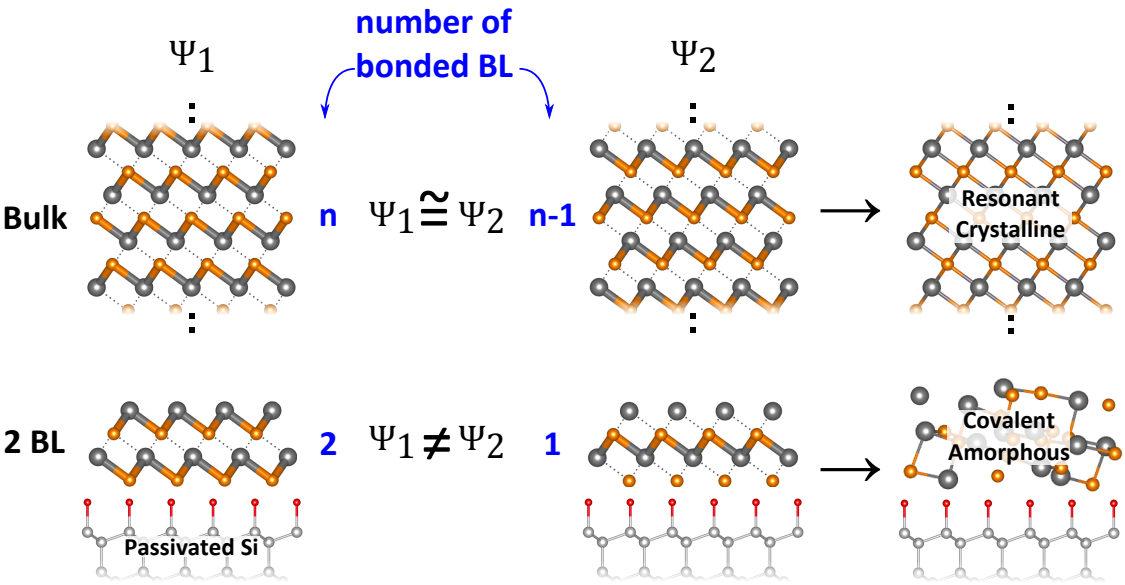

Figure 3.15: Schematic representation of GeTe bonding configurations Ψ1 and Ψ2 in the bulk, and in an ultra-thin films of 2 BLs on a $Si(111) - (7 \times 7)$ surface.

much better match with silicon, from the electronic point of view. Not only is resonant bonding more difficult in a confined thin-film, the amorphous phase is also preferred because of the silicon substrate.

The argument of the electronic mismatch however does not explain why no amorphous transition is observed in the case of GeTe on the Sb passivated silicon surface, why the film is able to grow crystalline from the very beginning. There are several factors that could help understand the different behavior in this case. Firstly, the terminating Sb atoms on the silicon surface adopt a "milkstool" configuration where each Sb atom is covalently bounded to one Si and two Sb atoms.[77] Therefore, although they are still covalently bonded, the surface Sb atoms are 3-fold coordinated, reducing the electronic mismatch with crystalline GeTe. Secondly, Sb by itself has a natural tendency for resonant bonding, both in its pure form, and also when intermixed with GeTe into GST.[19] Finally, the fact that the surface is passivated should also reduce the interfacial energy simply by reducing the interaction between the two materials at the interface, giving more weight to the bulk free energy. Surface passivation and vdW 2D materials favor the formation of resonant bonds but does not guarantee it, as shown by the present result for GeTe on $Si(111) - (1 \times 1) - H$, and for the GST on $GaSb(001)$.[103] In retrospect, for the latter case, the symmetry mismatch between the 3-fold symmetric GST film and the 4-fold $GaSb(001)$ surface could explain why the amorphous transition occurs. Therefore, symmetry mismatch between the film and substrate surfaces is also another factor that should influence the formation of resonant bonds.

As for the lattice mismatch, it does not seem to have an important influence on the resulting phase by itself; both crystalline and amorphous growth onsets were observed with the $\sim$10 % mismatch between GeTe and Si. However, a lattice matched situation should still be beneficial in terms of interfacial energy. The reason why a large lattice mismatch does not bear more adverse consequences on the formation of resonant bonding is due to the fact that relaxation occurs by other means than the formation of dislocations as in the classical epitaxy. For GeTe and GST on the Si$(111) - (7 \times 7)$ surface the epitaxial relationship is dictated by domain matching epitaxy, where mismatch is accommodated by the formation of in-plane rotated twisted domains. In this sense, if the substrate and the film cannot be perfectly matched, it is better in terms of interfacial energy to force the system into domain matching epitaxy by drastically increasing the mismatch rather than minimizing it.

To conclude this part, the dominant influence of the interface is highlighted in the epitaxial behavior of ultra thin films. Although the phenomenon of an amorphous transition at growth onset is not specific to resonantly bonded materials, it could be more likely to occur in them because of their intrinsic aspiration for long range order. It is therefore crucial to carefully select the substrate and engineer its surface if the goal is the growth of an ultra thin crystalline layer. In this respect, silicon, although technologically relevant, does not offer the best compatibility with the resonantly bonded phase change materials because of its covalent nature. However, it has also been shown that this limitation could be overcome, as illustrated by the Sb passivation for GeTe. Using this examplar, some hypothesis are outlined regarding the main actors playing in the interfacial affinity: Namely, the lattice and symmetry mismatch, the electronic mismatch and chemical affinity between the substrate and the film, and the degree of coupling between them in the case of a passivated surface or vdW epitaxy. The system is also expected to be temperature dependent; the minimal thickness is likely to decrease at higher temperature, as shown in the case of Sb deposited on glass.[91] From an experimental point of view, the contribution of each of these factors is difficult to isolate and quantify independently. With the current data, only a qualitative assessment can be made, with guidelines toward the promotion or suppression of resonant bonding inside the ultra-thin layer.

As an outlook, it would be interesting to try to utilize this particular capability of delayed crystallization to improve the epitaxial registry of GeTe on substrates that would otherwise yield poorly textured film. For instance, on substrates with $\sim 1 - 5$ % mismatch, classical lattice matched epitaxy would be expected. Growth would first be pseudomorphic, with possibly undesired out-of-plane orientations, relaxation would then occur through formation of innumerous threading dislocations once a certain critical thickness

is reached. If instead, growth is initiated by the deposition of an amorphous layer, there is already a certain volume of material gathered together, in a position to ¨express its own will¨, when the epitaxial relationship is decided, as crystallization occurs. In other words, while the epitaxial relationship in lattice matched epitaxy is enforced upon each crystalline nuclei locally, delaying the crystallization could allow for a more global epitaxial compromise between the film and the substrate, potentially giving access to previously uncharted heterostructures with novel properties.

3.3.2 Transient surface reconstruction near growth onset

As briefly hinted in Figure 3.12 (e)−(h), a transient GeTe$(111) - (\sqrt{3} \times \sqrt{3})R30°$ surface reconstruction is observed between 60 and 600 seconds of GeTe deposition on Si$(111) - (\sqrt{3} \times \sqrt{3})R30° -$ Sb. This reconstruction appears very consistently for each growth and vanishes as a certain thickness is reached. In Figure 3.16, an azimutal RHEED is acquired on a sample where growth was interrupted during this transient reconstruction. The $\sqrt{3} \times \sqrt{3}$ reconstruction can be recognized by the 2 additional equally spaced spots between consecutive brighter spots in the $\langle \bar{2}11 \rangle$ direction. Because the intensity of the spots from the transient reconstruction are visibly dimmer, it is likely that the two reconstructions coexist.

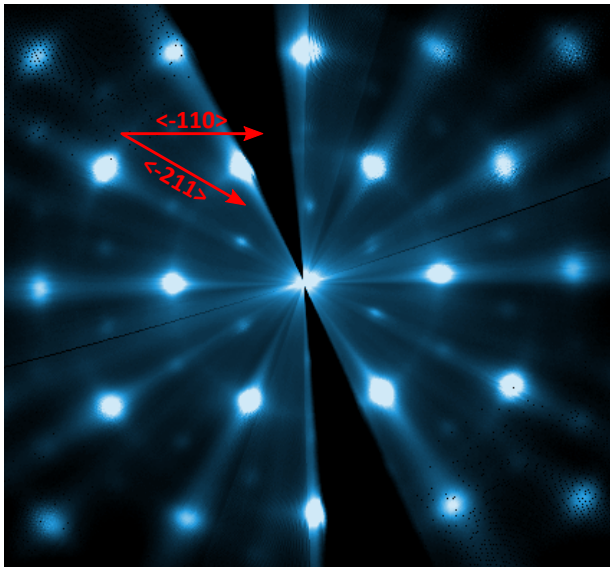

Figure 3.16: Angular dependence of RHEED intensity from GeTe grown on Si$(111) - (\sqrt{3} \times \sqrt{3})R30° -$ Sb, with growth interrupted after 300 seconds while the GeTe$(111) - (\sqrt{3} \times \sqrt{3})R30°$ surface reconstruction is observed.

In a collaborative effort with E. Bruyer,[†] D. Di Sante,[‡] and S. Picozzi,[†] the energy gained via relaxation of surface slabs were calculated and compared between $\sqrt{3} \times \sqrt{3}$ and 1×1 GeTe supercells.[35] The surface is assumed to be Te-terminated, because the Ge-termination has been calculated to be much less stable.[24] After relaxation, while all surface atoms relax in the same way with the 1×1 cell, two different sites are discriminated in the $\sqrt{3} \times \sqrt{3}$ case, slightly shifted vertically with respect to each other by 8.5 mÅ. Energetically, the two cases only differ by 0.6 meV, which is of the order of the numerical accuracy. Therefore, DFT corroborates that both reconstructions could indeed coexist, given the similar surface energies. This same reconstruction is also encountered during the growth of GeTe on Sb_2Te_3 within the superlattice structure, and will be mentioned again later in Chapter 4.

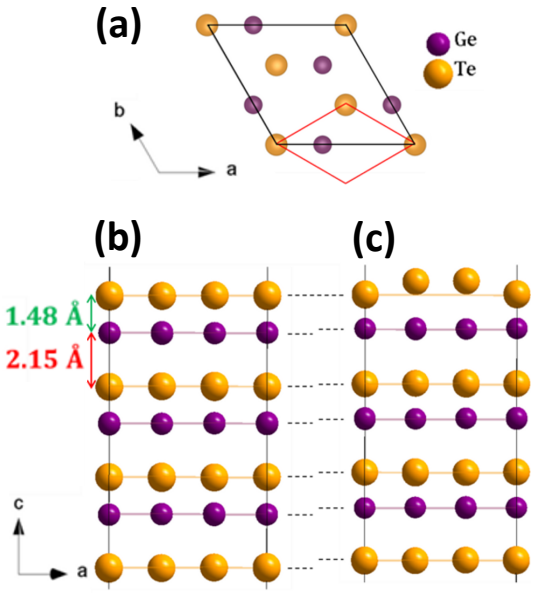

Figure 3.17: Schematic representation of the GeTe slab: (a) Relationship between the 1×1 unreconstructed (red) and the $(\sqrt{3} \times \sqrt{3})R30°$ reconstructed (black) surfaces. (b and c) Close-up on the subsurface layers before and after relaxation, showing the evolution of the interlayer spacing along [111]. The out-of-plane displacement of Te ions at the exact surface are artificially amplified for clarity. Calculations were carried out by the group of S.Picozzi at CNR-SPIN, L'Aquila Italy.

[†]Consiglio Nazionale delle Ricerche CNR-SPIN, L'Aquila, Italy
[‡]Departement of Physical and Chemical Sciences, University of L'Aquila, L'Aquila, Italy

3.3.3 Unusual in-plane lattice spacing at growth onset

As stated in the previous part, the growth of GeTe on the $\mathrm{Si}(111)-(\sqrt{3}\times\sqrt{3})R30°-\mathrm{Sb}$ surface yields a crystalline film from the very beginning of the growth. This conveniently enables the investigation of the crystalline structure of the film in this very early stage of the growth by RHEED. The right hand side of Figure 3.18 (b) shows the evolution of the RHEED intensity during deposition, acquired along a line across the RHEED streaks, as illustrated by the vertical dashed line across the left hand side RHEED image. The data presented here is acquired along the $\mathrm{Si}\langle\bar{2}11\rangle$ azimuth, measuring the d-spacing between $\mathrm{GeTe}\{\bar{2}11\}$ planes, as illustrated in Figure 3.18 (a).

As soon as the deposition starts, the RHEED streaks corresponding to the silicon substrate fade out completely within the first 10 seconds, new streaks appear immediately in their stead. When the integrated intensity of the specular beam is plotted during deposition, as shown in Figure 3.18 (c), oscillations are observed after an abrupt increase and then decrease of intensity due to a transient change of surface conditions. A first minima is found at $t = 50\,sec$, a maxima at $t = 100\,sec$, and a second maxima at $t = 190\,sec$. In a simplified model, these oscillations can be explained by sinusoidal variation in diffusely scattered intensity caused by the increase and decrease of island step edges perimeter as the coverage increases.[66] The period of RHEED oscillations can therefore be used as a measurement of the growth rate, which is estimated at one full layer completed each 100 seconds. One such layer is presumed to consist of one GeTe bi-atomic layer (BL), with a thickness of $0.35\,nm$, which translates into a growth rate of $0.21\,nm/min$. A rapid damping of the RHEED oscillations is observed after two oscillations, showing that the layer by layer growth process is imperfect, additional layers nucleate and coalesce at the same time, before the full completion of the antecedent layers.

The spacing between the RHEED streaks can be measured in the freshly deposited film, and the corresponding lattice spacing can be calculated using the known parameter of silicon as reference. After integrating the intensity along the RHEED streaks, and fitting them by Lorentzian functions, the $\{\bar{2}11\}$ lattice plane spacings are calculated and plotted over time in Figure 3.18 (d). Immediately at growth onset, a value of 2.46 Å is measured, which is larger than the expected value of 2.41 Å for bulk rhombohedrally distorted $\alpha-$GeTe.[104] Synchronized with the first minima in RHEED intensity oscillations, $t = 50\,sec$, the lattice spacing then starts to drop, until the expected value for $\alpha-$GeTe is reached at $t = 200\,sec$, with the completion of the second GeTe BL.

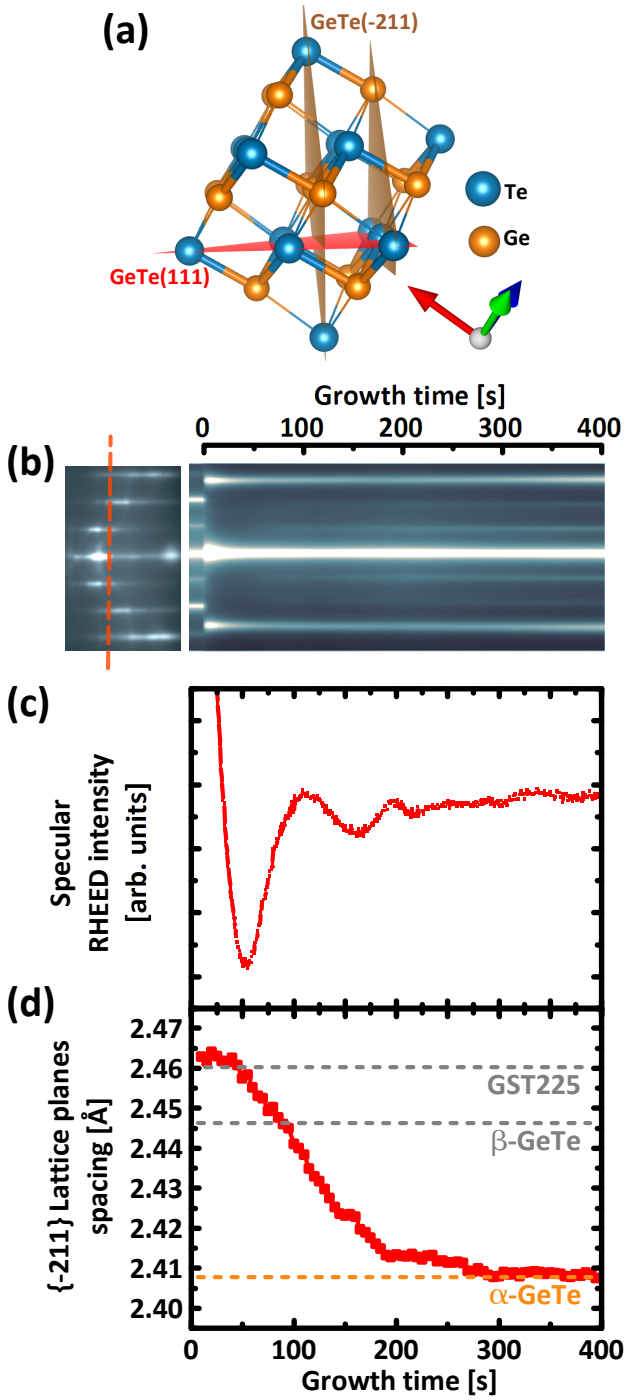

Figure 3.18: (a) Schematic model of α–GeTe crystal with the $(\bar{2}11)$ planes highlighted in brown color. (b) RHEED intensity over time during growth acquired along a line across the $\langle\bar{2}11\rangle$ azimuth RHEED pattern. (c) Integrated specular beam intensity oscillations close to growth onset. (d) $\{\bar{2}11\}$ lattice planes spacing calculated from distances between RHEED streak

The measured higher value cannot be due to relaxation from the silicon substrate lattice because growth does not follow lattice matched epitaxy. And more importantly, the lattice of silicon is much smaller (2.22 Å), relaxation would be expected to occur from a smaller value toward the bulk value, the opposite of what is observed. So growth seems to be initiated with the formation of a phase different than the intended $\alpha-$GeTe. A comparison with literature shows that this initial value matches better with the cubic phase of GeTe at 2.446 Å,[104] or with metastable rocksalt $Ge_2Sb_2Te_5$ at 2.46 Å,[105] as highlighted with horizontal dashed lines in Figure 3.18 (d).

The possibility for this phenomenon to be a kinetic effect is also ruled out by performing a similar experiment with a halved germanium flux, on which the growth rate is entirely dependent of, whereas tellurium is supplied in excess and desorbed. The exact same behavior was observed, only at a slower rate, as expected. This is shown in Figure 3.19: The period of the two first specular RHEED intensity oscillations is doubled; the first minima is found at $t = 100\,sec$, the first maxima at $t = 200\,sec$, and second maxima at $t = 400\,sec$. Exactly the same changes in lattice spacing aforementioned are observed here.

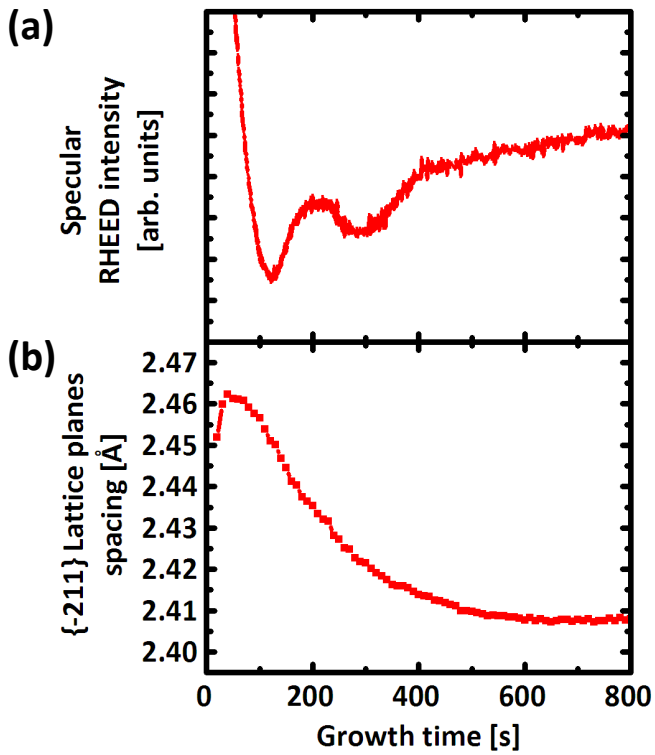

Figure 3.19: (a) Specular beam intensity oscillations close to growth onset in the case of a low Ge flux growth. (b) {$\bar{2}$11} lattice planes spacing calculated from RHEED streak spacing.

To further investigate the growth onset of GeTe on the $Si(111) - (\sqrt{3} \times \sqrt{3})R30° - Sb$ surface, very thin films of a few atomic layers were grown with nominal thicknesses of 0.5, 1, 2, 4, 6, 8, and 16 BLs. Until each growth is interrupted, the larger in-plane lattice spacing on the Sb terminated surface was consistently observed, testifying of the reproducibility of this phenomenon. Moreover, as the growth is interrupted, the RHEED image is "frozen"and does not change further after the deposition is stopped, demonstrating the stability of these thin layers and corroborating that the phenomenon observed is not a dynamic effect. All the samples are capped at RT in the load-lock of the MBE system at a pressure of 10^{-8} *mbar* with 5 *nm* of amorphous Si_3N_4 to protect the film against oxidation.

Courtesy of J. Momand,[†] and B. J. Kooi,[†], these ultra-thin GeTe films were investigated using cross-sectional TEM. Micrographs acquired on the 1 BL thick sample are shown in Figure 3.20. The first one in (a) is a low resolution TEM, where a clear continuous dark line can be observed between the substrate and the capping layer. The contrast in this case extends beyond the boundaries of the material; the dark area is thicker than the actual thickness of the film. But the fact that contrast is generated shows that a fully covering film has indeed been deposited, as corroborated by the complete evanescence of the silicon streaks upon growth in RHEED. A higher resolution micrograph along the $Si\langle\bar{2}11\rangle$ direction (Figure 3.20(b)) reveals that there is crystalline order within the film, as it will be further demonstrated by Raman measurements. A certain roughness can already be discerned, which explains the rather rapid damping of the RHEED oscillations. These micrographs show the capability of creating ultra-thin crystalline GeTe layers using MBE.

Raman spectroscopy is then performed on each of these GeTe films with increasing thickness, the measurements are acquired in $z(y, xy)$-z geometry with a 633 *nm* laser, and shown in Figure 3.21. The features at 225 cm^{-1} and 300 cm^{-1} visible in the silicon reference spectrum respectively correspond to the $2TA(L)$ and $2TA(X)$ modes of silicon.[106] With increasing thickness of the GeTe film, these modes from the silicon substrate become less intense, giving an idea of the penetration depth of the 633 *nm* radiation in GeTe. In the three thinnest samples, except from those silicon modes, only a weak and broad feature can be measured at 150 cm^{-1}. In stark contrast, two much clearer features can be resolved for the thicker samples. Both peaks identified as the (E) and $(A1)$ modes of GeTe at 80 cm^{-1} and 120 cm^{-1} respectively[107] are subjected to a size related mode strengthening similar to what has been observed for GeTe nanocrystals.[28] The extent of the shift is explicitly plotted in Figure 3.22(a). This clear difference between the samples with thickness below and above 4 BLs could be explained by a lack of rhombohedral

[†]Zernike Institute for Advanced Materials, Groeningen, the Netherlands

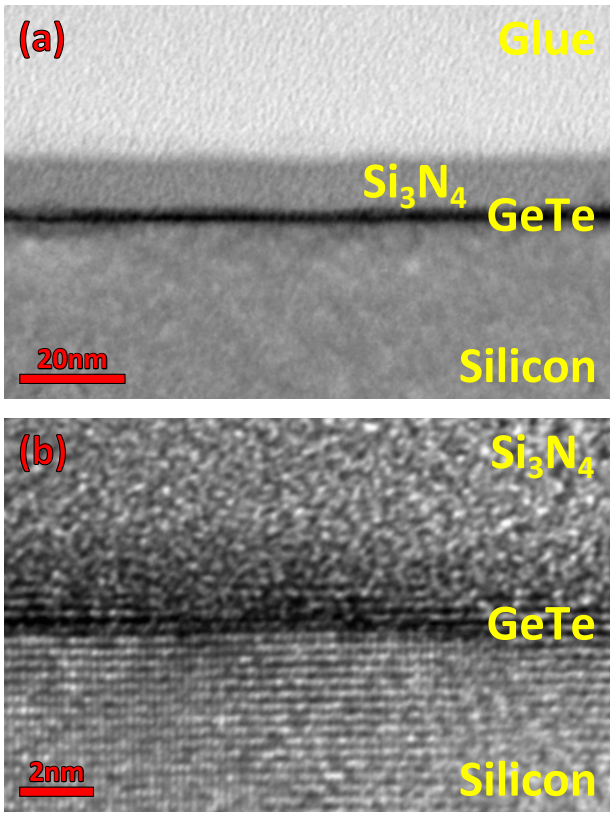

Figure 3.20: (a) Low resolution TEM micrograph of a nominal 1 BL thick GeTe film grown on $Si(111) - (\sqrt{3} \times \sqrt{3})R30° - Sb$. (b) Cross-section HRTEM along $Si\langle\bar{2}11\rangle$ on the same sample as in (a). TEM imaging was carried out by J. Momand and B. J. Kooi from the Zernike Institute for Advanced Materials, and M. Verheijen from the Eindhoven University of Technology.

distortion and a suppression of Peierls distortions in the thinner samples. Indeed, the undistorted GeTe crystal becomes a cubic rocksalt structure, in which case no first order Raman modes are expected.[107,108]

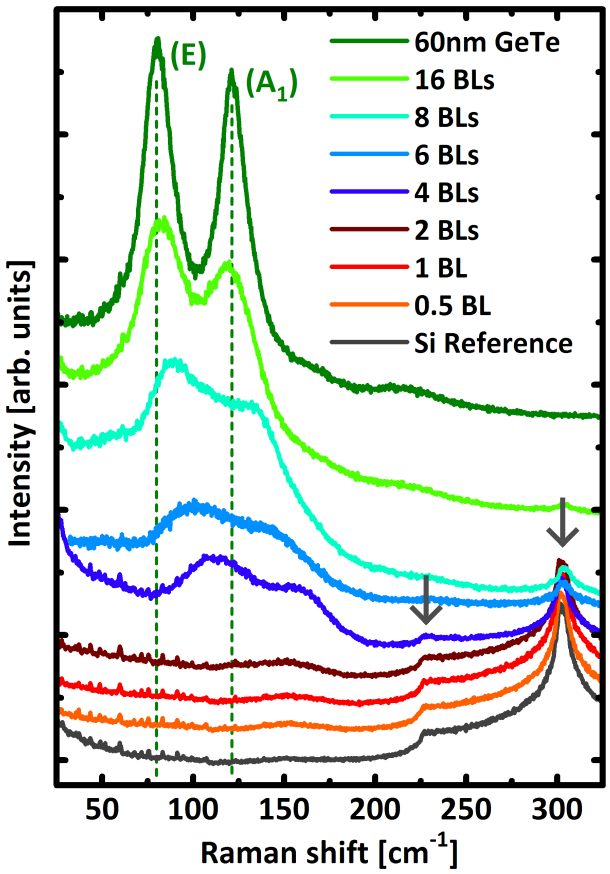

Figure 3.21: Raman spectra acquired on GeTe samples of increasing thickness of 0.5, 1, 2, 4, 6, 8 , 16 BLs grown on $Si(111) - (\sqrt{3} \times \sqrt{3})R30° - Sb$. Measurements on a silicon reference and a thicker 60 *nm* GeTe film are shown as a comparison.

In collaboration with D. Campi[†] and M. Bernasconi[†], the phonons at the Γ-point of GeTe multilayers have been computed by means of Density Functional Perturbation Theory (DFPT),[109] in order to explain the shift of the Raman peaks in the ultra-thin film. Due to the lattice mismatch, the commensurate surface cell of GeTe multilayers grown on $Si(111) - (\sqrt{3} \times \sqrt{3})R30° - Sb$ is too large to be addressed by DFPT methods. Therefore, a thick slab of GeTe is considered in order to model the growth of GeTe multilayers on the Sb-passivated Si surface, with a number of layers that are free to move, and few bottom frozen layers mimicking the surface substrate. The in-plane lattice parameter is either fixed to the theoretical bulk value, or to the experimental value measured by RHEED

[†]Department of Materials Science, University of Milano, Milano, Italy

through MBE growth. With a concentration of holes comparable with experiments,[110] the position of the Raman peaks calculated theoretically for the bulk at zero temperature are at 84 and 130 cm^{-1}. Those values are plotted in Figure 3.22(c) with empty symbols. The agreement with experiments is good taking into account that at room temperature we expect a red shift of the frequency computed at zero temperature.[107]

The DFPT Raman spectrum in backscattering configuration for non-polarized light is reported in Figure 3.22(b) for the supported 4 BL (open symbols). The displacement patterns of the modes mostly contributing to the peak at 120 and 164 cm^{-1} are given in of Figure 3.22(c). The spectrum compares well with the experimental one, considering that the redshift due to temperature was not included in the calculations. Configurations in which the free layers are shifted in the surface plane with respect to the bottom frozen layers ($AB-AB-CA-BC-$) in order to destroy the resonant bonding and reduce the coupling between the free layers and the frozen substrate. The effect on phonon frequency for the 4 BL is actually marginal ($< 2\,cm^{-1}$). Thus the DFPT results corroborate the observation of the formation at growth onset of a phase different than α-GeTe, which then turns into the αphase for the 4 BL and beyond.

On the other hand, the frequency of the A_1 and E modes for the supported 1 and 2 BL are in the range $136-140\,cm^{-1}$ and $184-195\,cm^{-1}$ with variations depending on the choice of the in-plane lattice parameters (experimental or bulk-like) and the stacking of the frozen layers with respect to the free ones; modes in these latter frequency ranges have no experimental counterpart in the Raman spectrum.

Dispelling a common misconception, Gaspard *et al.* have predicted that crystalline periodicity is not necessary for Peierls distortions to occur,[21] the most convincing evidence supporting this claim is that Peierls distortions were observed in liquid GeTe close to the melting point.[111] Therefore the lack of out-of-plane long range periodicity in a very thin GeTe film should a priori not inhibit Peierls distortions, but the proximity of the interface and the surface could prevent Peierls distortions from being expressed normally.

And even if Peierls distortions do occur, a high degree of ordering of the short and long bonds is needed in order to observe a net deformation of the overall crystal structure. If short and long bonds are disorderly distributed, the crystal will be seen as being cubic in average. From a theoretical standpoint, Gaspard *et al*. have also predicted that the ordering of the bonds was energetically favorable in the idealized case.[21] But experimental data shows that these bonds can be found in a disordered configuration: For instance, the initial belief that the rhombohedral to cubic transition from $\alpha-$GeTe to $\beta-$GeTe was purely of a displacive nature[104] has been more recently challenged.[32] The more re-

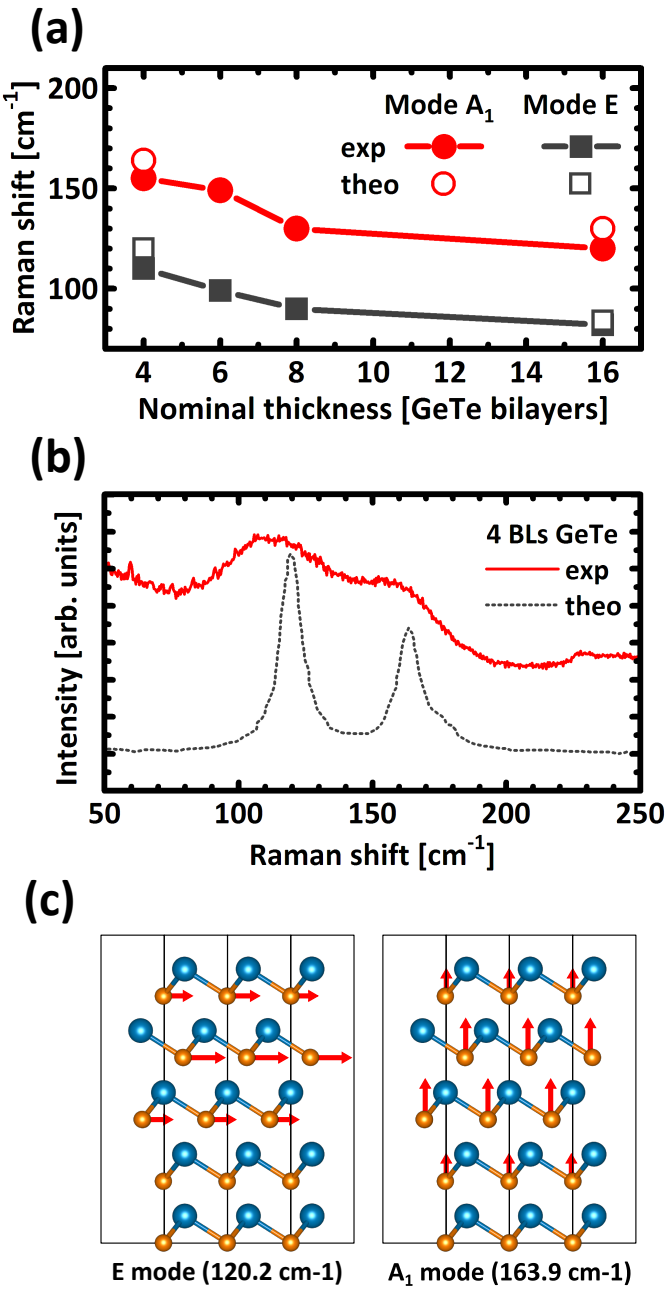

Figure 3.22: (a) GeTe $(A1)$ and (E) mode strengthening with decreasing film thickness, theoretical calculated values for 4 BL and bulk are plotted with open symbols. (b) Raman spectrum acquired on 4 BL GeTe sample grown on $Si(111) - (\sqrt{3} \times \sqrt{3})R30° -$ Sb (line) compared with a theoretical analogous spectrum calculated at $0K$ (dashed line). GeTe $(A1)$ and (E) modes are visible. (c) Displacement patterns for the two most active Raman modes (E left, $A1$ right) of the 4 BL supported on the bulk. All calculations were performed by the group of M. Bernasconi from the University of Milano.

cent EXAFS data could only be conciliated with the previous XRD data using an order-disorder transition model. A similar interpretation was also given by Biquard *et al.* in the case of nitrogen and carbon doping into GeTe, which would cause the loss of ordering of the Ge–Te bonds, such that the XRD spectrum would seem to correspond to a cubic structure by an averaging effect.[112] In the present case, because of the influence of the interface and surface, a certain degree of disorder in the bonding cannot be excluded in the very thin films, making the in-plane lattice spacing larger in average. Then, as the growth continues, these bonds with the completion of the second GeTe BL have the chance to reorganize towards the more favorable ordered configuration.

As mentioned in chapter 3.1.2, intermixing of GeTe with Sb into an initial GST layer can also not be completely excluded, and it could be a possible interpretation for both RHEED and Raman data, but the process that supplies the Sb contamination is unclear. A dedicated secondary ion mass spectrometry experiment would be needed to assess the amount of Sb contamination and its precise localization. But meanwhile, it is acknowledged that even a small amount of Sb can potentially induce structural changes into GeTe. And because the level of contamination is assumed to be minimal, intermixing into GST can at most only partly account for the structural changes described above.

As a side note, the concentration and localization of Ge vacancies could also have an impact on the structure. Deringer *et al.* have predicted that it would be energetically favorable for Ge vacancies to diffuse away from the interfaces, into the bulk.[24] They have also predicted that the diffusion of these vacancies is indeed energetically plausible, by the hopping of Ge atoms between vacancies.[38] But these calculations cannot be readily applied to a film so thin that it has essentially no bulk. The very existence of Ge vacancies in these very thin films is also not demonstrated yet.

To conclude this part, an in-plane lattice spacing larger than expected when depositing GeTe on $\mathrm{Si}(111) - (\sqrt{3} \times \sqrt{3})R30° - \mathrm{Sb}$ was observed. The presence and influence intermixing with Sb cannot be excluded, but the viability of Peierls distortions and their coherent ordering in such a thin film are designated as the fundamental physical mechanism responsible for the apparent larger in-plane lattice spacing. If Peierls distortions cannot be fully manifested in an orderly fashion within the constrained volume at growth onset, the GeTe crystal may only acquire its ferroelectric properties as growth proceeds, once the bonds are Peierls-dimerized and ordered into layers. For scaling purposes, this suggests that special care should be taken in the selection of the bottom electrode, as the interface will play a decisive role for the ferroelectric properties of the ultra-thin film.

3.4 Regarding the calculation of growth rates

In the estimation of the growth rate, some differences appear between the value obtained from the RHEED oscillations and the ones calculated from XRR. The spectrum measured on a GeTe film grown for 400 *sec* is shown in Figure 3.23, and on a thicker film grown for 150 *min* in Figure 3.24. Both samples are capped with $\sim$ 10 *nm* of Si_3N_4. Fitting is performed using a simple model two layers with specular interfaces, the parameters used for both spectra are reported in Table 3.2 and 3.3 respectively.

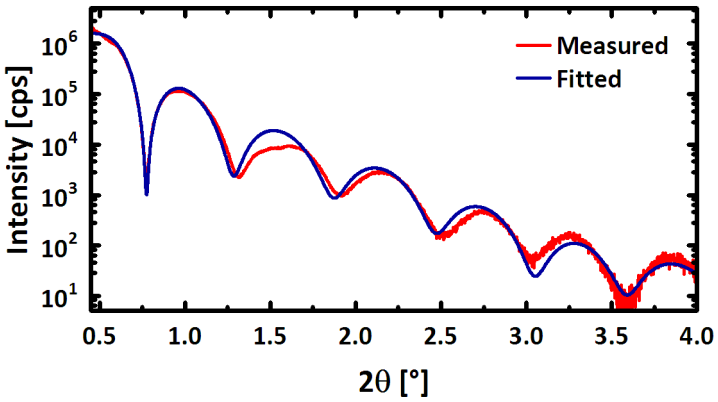

Figure 3.23: XRR spectrum acquired on a GeTe film grown for 400 *sec* on the Sb-passivated silicon, along with fitted spectrum. The sample is capped with Si_3N_4.

Layer	Density $[g/cm^3]$	Thickness $[nm]$	R_{RMS} $[nm]$
Si_3N_4 cap	3.38	12.24	0.4
GeTe film	6.16	2.6	0.35
Si substrate	2.33	–	0.3

Table 3.2: Fitting parameters used for fitting presented in Figure 3.23.

Layer	Density $[g/cm^3]$	Thickness $[nm]$	R_{RMS} $[nm]$
Si_3N_4 cap	3.31	10.54	4.19
GeTe film	6.56	45.48	4.77
Si substrate	2.33	–	0.45

Table 3.3: Fitting parameters used for fitting presented in Figure 3.24.

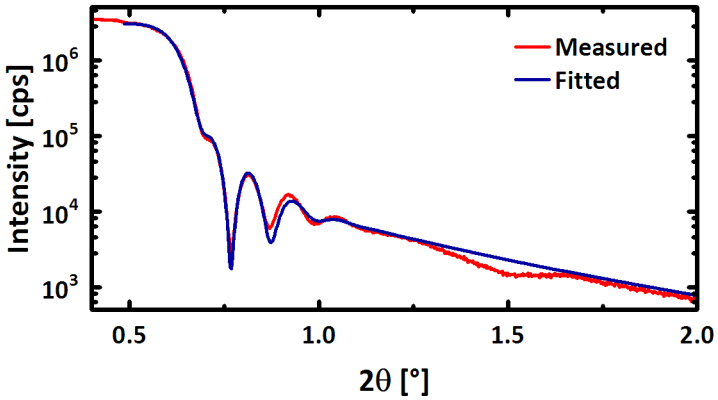

Figure 3.24: XRR spectrum acquired on a GeTe film grown for 150 *min* on the Sb-passivated silicon, along with fitted spectrum. The sample is capped with Si_3N_4.

Comparing the different values, the RHEED intensity oscillations suggest that the growth rate near growth onset is 0.21 *nm/min*. However XRR on the film grown for 400 *sec* yielded a growth rate of 0.39 *nm/min*, nearly the double. As for the growth rate calculated from the much thicker 60 *nm* film, a value of 0.30 *nm/min* is obtained. This shows that the growth rate does not remain constant during the whole deposition. It can be expected that the growth slows down with increasing thickness: Because the sample is heated by infrared radiation, and because the silicon substrate is mostly transparent to the infrared compared to GeTe, absorptivity increases during growth, leading to an increase in surface temperature and desorption.[113] As for the very slow initial growth rate , it could be due to difficulties for the material to nucleate and stick on the passivated surface, the growth would then accelerate as soon as the first 2 BLs are formed. The fact that oscillations are only observed during the deposition of these first 2 BLs could be also linked with this acceleration in the growth.

Overall, the quality of the fitting could only barely be satisfactory. As shown in Figure 3.23 and 3.24, the periodicity of the oscillations match well, but the intensities and shapes are off. This could be due to some inhomogeneities in the film due to a non-homogeneous temperature across the substrate surface. The first few atomic layers could be particularly sensitive to temperature, the smallest difference leading to relatively big differences in the growth rate. As a technical precept, the acquisition of XRR data on several small pieces of the same sample should be advised instead of one single measurement on the whole 2×2 *cm* piece. This would yield spectra that are easier to fit, and give a better idea of the homogeneity in the sample.

XRD can also provide information about the film thickness and growth rate through the spacing of Laue fringes around the GeTe(111) peak, as shown in Figure 3.25. the film thickness is also determined from the XRR spectrum acquired on the same sample for comparison. A discrepency is commonly observed between the value obtained by these two methods. In this specific case, a thickness of 30.7 nm is calculated from the spacing between the Laue fringes, while a larger value of 33.5 nm is obtained by fitting the XRR spectrum.

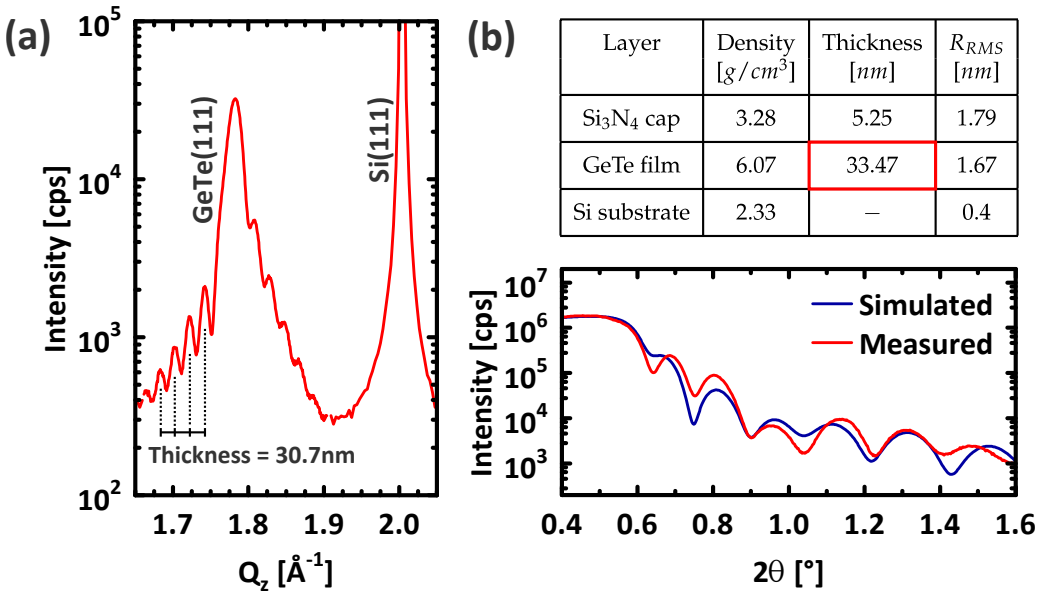

Figure 3.25: (a) Thickness calculation from Laue fringes in symmetric $\omega - 2\theta$ XRD scan around the GeTe(111) reflection. (b) Thickness obtained by fitting Kissig fringes from XRR measurements on the same sample.

While Laue finges may look similar to Kiessig fringes measured by XRR, they are of a completely different nature. Kiessig fringes in XRR stem from a constructive interaction between X-rays that are reflected from the interfaces and surface of the film, due to the changes in density and refractive index. These fringes are measured regardless of the crystallinity or texture in the film. In contrast, Laue fringes measure the size over which specific reflections are coherent. In real space this corresponds to the size over which the periodicity of specific lattice planes is respected. Therefore, disordered areas at interfaces and rough surfaces are invisible to Laue fringes while they are still accounted for by Kissig fringes. And for this reason, the thickness obtained from XRD fringes is often slightly lower than the one obtained from XRR.

3.5 Summary and conclusion

In this chapter, the differences in the epitaxy of GeTe on three differently reconstructed Si(111) surfaces were investigated. In Table 3.4 the main results are summarized.

	$Si(111)-(7\times7)$	$Si(111)-(\sqrt{3}\times\sqrt{3})R30°-Sb$	$Si(111)-(1\times1)-H$
Surface passivation	partial	full	full
Twisted domains	Yes	fully suppressed	fully suppressed
Twin domains	Yes	strongly suppressed	partially suppressed
Amorphous growth onset	Yes	No	Yes
Cubic GeTe at growth onset	No	Yes	No

Table 3.4: Summary of results discussed in Chapter 3.

Two of these reconstructions leave a fully passivated surface, whereas the $Si(111)-(7\times7)$ still exhibits dangling bonds. These are responsible for the domain matched twisted domains that are otherwise suppressed on the passivated surfaces. The latter cases are better explained by vdW epitaxy, which is surprising for GeTe since it is not commonly considered as a 2D material. This behavior is nonetheless justified by the relative weakness and flexibility of resonant dangling bonds, and the further weakening of one side of the bonding p-orbital due to Peierls dimerization.

Another surprising observation is the suppression of twinned domains when GeTe is grown on the passivated surfaces. Because the interaction with such surfaces should be weak, one could expect the twinned domains to be more readily formed. These counter-intuitive results could arise from point defects in the surface termination, pinning the film preferentially into one domain. Or in the case of the Sb passivation, the top surface also adopts a 3-fold symmetry, which could prevent twinning with the film of the same symmetry. Intermixing of GeTe with Sb cannot be completely excluded, and may also play a role in the determination of the epitaxial relationship.

Both on $Si(111) - (7 \times 7)$ and $Si(111) - (1 \times 1) - H$, an amorphous growth onset was encountered. The fact that this is observed both on a passivated and non-passivated surface shows that this property is not decisive in the occurrence of the phenomenon, although it may still play a role. This amorphous growth onset is attributed to the necessity for a certain long-range order for resonant bonding to be fully expressed, and its lesser stability in an ultra-thin film dominated by its interface and surface energy. There is also an electronic mismatch between the 4-fold coordinated covalent Si and the 3-fold coordinated crystalline GeTe. Instead, the covalently bonded amorphous GeTe offers a better matching interface.

In the case of the $Si(111) - (\sqrt{3} \times \sqrt{3})R30° - Sb$ surface, this amorphous transition is avoided, meaning that the interface is able to stabilize the resonant bonds. Either Sb itself is promoting their formation, or the electronic mismatch is reduced because the surface atoms are 3-fold coordinated with this reconstruction. Because GeTe is directly deposited crystalline, RHEED can be used to probe the earliest stage of the growth, where another interesting phenomenon is observed: The in-plane lattice spacing is larger than expected during the deposition of the first two BLs. Raman measurements show that all modes are suppressed, which indicates that the crystal structure at this stage could be cubic, implying that the material does not possess its ferroelectric properties yet.

All these results show that GeTe performs epitaxy in a quite particular way. It can neither be assimilated to a 3D material, nor to a 2D material. On $Si(111) - (\sqrt{3} \times \sqrt{3})R30° - Sb$, GeTe forms twisted domains with the unreconstructed $Si(111) - (1 \times 1)$ surface, suggesting a 3D behavior. On the passivated surfaces, twinning is also reduced, which shows a certain strength in the interaction with the surface. But then, twisted domains are suppressed like in the case of vdW epitaxy of 2D materials.

This ``hybrid´´ behavior is clearly due to resonant bonding, these bonds that are neither covalent, nor ionic. Stronger than vdW forces, but weaker than covalent bonds, resonant bonding keeps the atoms in a stable but flexible configuration. One can easily conceive how this malleable network is the ideal structure for a phase-change material.

4 Epitaxy of GeTe / Sb_2Te_3 superlattice structures

In the quest for the best material candidates in phase change memory (PCM) applications, GeTe / Sb_2Te_3 chalcogenide superlattice structures (CSL) have boasted better performances compared to their homogeneous GST counterparts.[10] Not only did the CSL cells operate at a lower current, their cyclability improved, showing very little changes in their properties after millions of cycles. These superior performances have been ascribed to a reduced configuration entropy in the crystallization of GeTe, enforced by its confinement between the Sb_2Te_3 layers. The interface with these layers should also provide GeTe with a template for crystallization, promoting less costly heterogeneous nucleation. Following this line, number of publications have been proposed, refining the models describing the switching mechanism,[49,51,114] or investigating the beneficial role of the interfaces.[115]

In the present work, to investigate and verify these models, GeTe and Sb_2Te_3 heterostructures are grown by MBE with the highest level of texturing, showing practically no configuration entropy. In these films of the highest degree of ordering achievable experimentally, the interfaces are clearly imaged using scanning transmission electron microscopy (STEM) in high-angle annular dark field mode (HAADF), with the individual atomic columns discriminated by their isotopic mass.

Combined with more global characterization methods, such as XRD and Raman, attention is called to the tendency of GeTe and Sb_2Te_3 to intermix at the interface into GST. In light of the results presented here, it seems thermodynamically unlikely for the two materials to maintain a clear and well defined interface between them, as it is suggested in some of the existing models in the literature. Beyond their applications as phase change materials, and topological insulators,[116] CSLs could also be used to engineer a highly tunable strain within the sublayers, as evidenced by in-situ RHEED and in-situ XRD data collected using synchrotron radiation.

4.1 Growth and characterization of superlattice structures

4.1.1 Characterization by X-ray diffraction and Raman spectroscopy

In the previous chapter, we have shown how the use of a passivated surface improved the crystalline quality of both GeTe and Sb_2Te_3 epitaxial films. While Sb_2Te_3 can be considered as a *bona fide* case of 2D material performing vdW epitaxy on the passivated silicon, the same results with GeTe came more as a surprise. The latter was explained by the weakness and flexibility of the Peierls distorted resonant ``dangling bonds'' that allowed GeTe to mimic 2D materials.[35]

Interestingly, these improvements achieved in the two separate materials can be readily applied to CSL structure, with both materials stacked on top of each other. This is illustrated in Figure 4.1 (a), where XRD $\varphi-$scans on pure Sb_2Te_3 films are compared with CSLs that start with Sb_2Te_3 as their first sublayer. Growth of Sb_2Te_3 on the $Si(111)-(7\times7)$ surface yields two twisted domains at $\pm5°$ (dark red). And if Sb_2Te_3 is used as the first layer in a CSL grown on the same surface, the same twisted domains are found throughout the whole structure (dark blue). Similarely, twisted domains are suppressed if Sb_2Te_3 is grown on $Si(111)-(\sqrt{3}\times\sqrt{3})R30°-$Sb (light red), and they are suppressed as well for a CSL starting with Sb_2Te_3 on the same passivated surface (light blue). Therefore, it is concluded that the epitaxial relationship is decided with the growth of the initial sublayer, these in-plane domains are then propagated throughout the whole CSL. The crystalline quality of the CSL in terms of in-plane texturing is only slightly lower than that of the Sb_2Te_3 single layers. (FWHM of 2.8° for the CSL, and 1.8° for the Sb_2Te_3 film)

The same applies to CSLs starting with GeTe as their first layer. Growth of GeTe on the Sb terminated surface suppresses the twisted domains, preventing their formation in the rest of the CSL. One noteworthy difference resides in that twinned domains are strongly suppressed in pure GeTe, whereas they are formed again propagated later during growth in the CSL, probably during the deposition of the Sb_2Te_3 layers. This is shown in the two $\varphi-$scans of Figure 4.1 (b). A direct visualization of these defects is going to be shown later, with Figure 4.8.

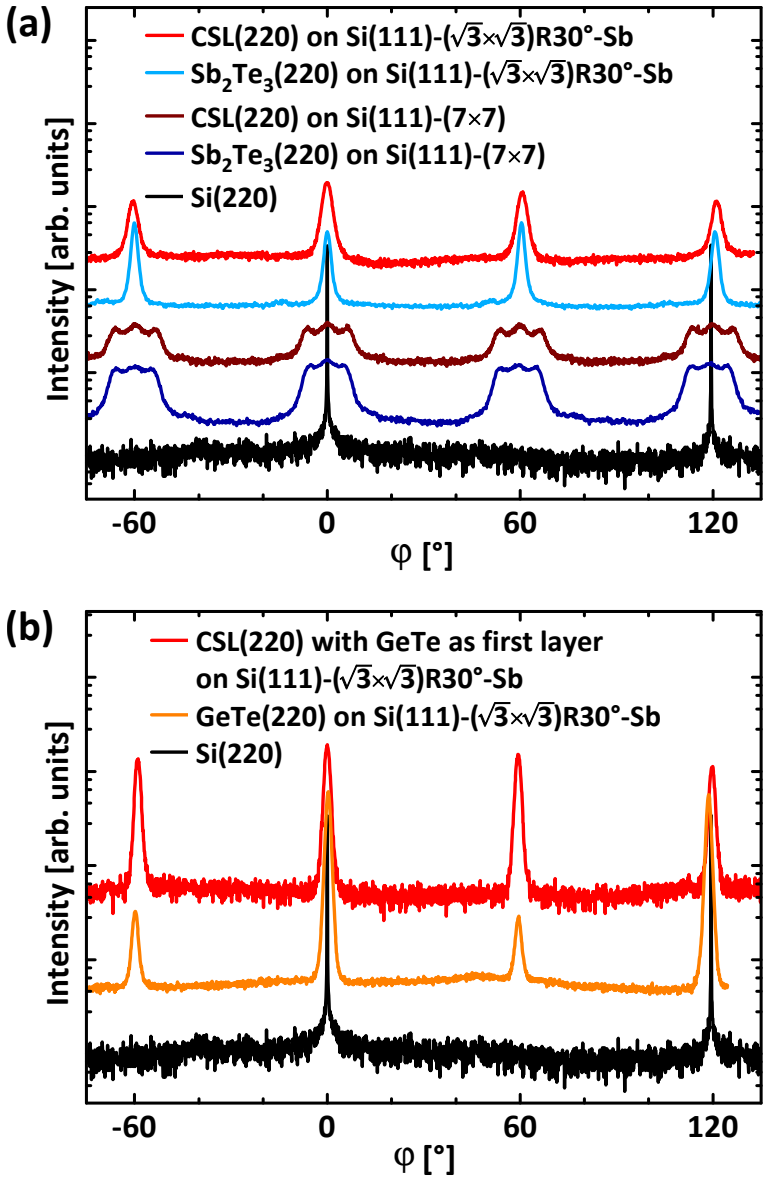

Figure 4.1: (a) XRD $\varphi-$scan of Sb_2Te_3 films grown on $Si(111)-(7\times 7)$ and $Si(111)-(\sqrt{3}\times\sqrt{3})R30°-$ Sb, showing the $Sb_2Te_3\{220\}$ reflections. The same rotational domains are found in CSL structures grown with Sb_2Te_3 as a first layer. Substrate $Si\{220\}$ reflections are shown as a reference. (b) Comparison between XRD $\varphi-$scans on a CSL structure starting with a first layer of GeTe, and a pure GeTe film grown on the same $Si(111)-(\sqrt{3}\times\sqrt{3})R30°-$ Sb surface.

A CSL with GeTe as its first layer is in fact non-trivial to engineer using other methods than MBE. For deposition techniques yielding amorphous films, such as RF sputtering or physical vapor deposition, a ``buffer layer'' of Sb_2Te_3 is often applied, in order to utilize the intrinsic tendency of the material to texture itself in the out-of-plane direction, owing to its 2D nature. This method allows for enhanced out-of-plane texturing in those polycrystalline CSL films after annealing.[49] Therefore, it is uncommon to find CSLs starting with GeTe in the literature, this advantage offered by a first Sb_2Te_3 layer being too precious to forgo. By MBE, growth can be initiated with GeTe just as well as with Sb_2Te_3, but lower interface roughness and narrower peaks were still obtained for the CSL starting with Sb_2Te_3.

To investigate the out-of-plane epitaxial relationship between the CSL film and substrate, symmetric $\omega - 2\theta$ XRD scans are performed. One such measurement acquired on a $10\times[Sb_2Te_3(6\,nm)/GeTe(4\,nm)]$ CSL (CSL 6/4) is shown in Figure 4.2, along with reference spectra from GeTe and Sb_2Te_3 thin films. All spectra are again plotted in reciprocal lattice units as in (3.3), and the sharpest peaks at $Q_z = 2.00$ and $4.00\,\text{Å}^{-1}$ are identified as the first and second order Si(111) and (222) reflections from the silicon substrate.

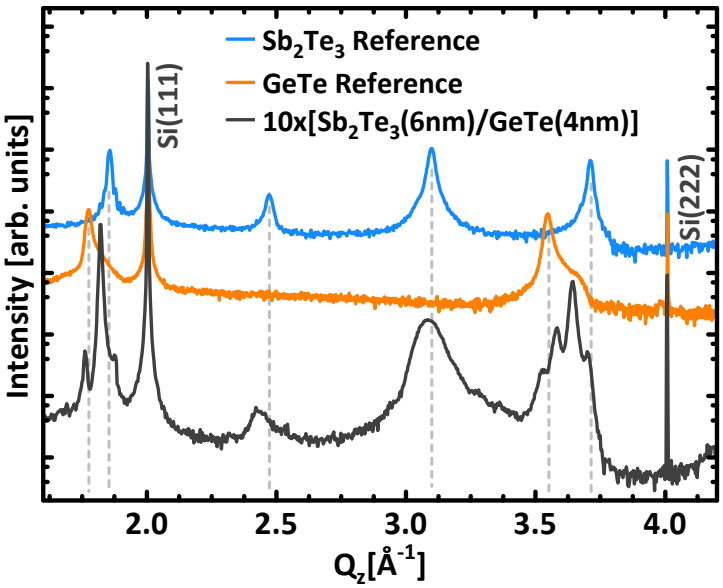

Figure 4.2: Symmetric $\omega - 2\theta$ XRD scan from the CSL 6/4, with reference spectra from GeTe and Sb_2Te_3 thin films.

In the bulk references, the GeTe(111) reflection at $Q_z = 1.805\,\text{Å}^{-1}$ and Sb_2Te_3(00.9) at $Q_z = 1.86\,\text{Å}^{-1}$ originate from the average out-of-plane periodicity of the Te sublattice in these crystals. The second order reflections are measured for GeTe(222) at $Q_z = 3.61\,\text{Å}^{-1}$ and Sb_2Te_3(00.18) at $Q_z = 3.72\,\text{Å}^{-1}$. Similarely, the groups of peaks centered around $Q_z = 1.82$ and $3.64\,\text{Å}^{-1}$ originate from the equivalent planes in the CSL, they represent

the average out-of-plane periodicity of the Te sublattice. From this point, these peaks are labeled CSL(111) and CSL(222). Because GeTe and Sb_2Te_3 are periodically stacked on top of each other in the CSL, the X-rays do not see the two separate materials but considers them as one single structure with incommensurate compositional and structural modulation in the out-of-plane direction. The position of these peaks, which is always going to be somewhere between the analogous reflections of GeTe and Sb_2Te_3, can give an indication about the composition of the CSL. For example, if the CSL(111) peak is very close to the expected position of Sb_2Te_3(00.9), the CSL is likely to be Sb_2Te_3 rich.

Around the CSL(111) and CSL(222) reflections, a group of incommensurate satellite peaks are gathered. The distance between these represents the superlattice periodicity; the thickness of one GeTe sublayer plus one Sb_2Te_3. Only satellites up to the 2^{nd} order can be clearly discriminated, while higher order peaks are strongly attenuated. This indicates that the structure suffers from non-negligible fluctuations in the CSL periodicity. As discussed in chapter 3.4, the surface temperature is likely to rise during deposition, leading to a reduced growth rate. Therefore, a systematic deviation in the sublayer thicknesses can be expected. Such linear deviations have been shown to have the most crippling effect on the intensity and width of the satellite peaks, and especially for the higher order ones.[117] Systematic deviations also cause broadening of the satellite peaks. Random fluctuation can also be at play, as the roughness increases with the number of CSL repetitions.

The next features that need to be identified are the broad features in the range between $Q_z = 3$ and $3.5\,\text{Å}^{-1}$. This portion of the spectrum is better shown in Figure 4.3 (b). The origin of these reflections can be explained by understanding the link between the crystalline structure of Sb_2Te_3 and its XRD spectrum. As illustrated in Figure 4.3 (a), the Sb_2Te_3(00.12) and Sb_2Te_3(00.15) reflections divide $\Delta1'$, the spacing between Sb_2Te_3(00.9) and Sb_2Te_3(00.18), into three equal parts $\Delta3'$. As explained above, $\Delta1'$ corresponds to the average periodicity of the Te sublattice. The presence of these peaks at a third of $\Delta1'$ in reciprocal space correspond in real space to periodic structures that are three times larger than the Te sublattice. For Sb_2Te_3 these structures are evidently the vdW gaps, separating each QL, each three Te layers. Because the working principle of XRD is based on the diffraction of X-rays by periodic structures in the electronic density of the crystal, it is not surprising that these regularly spaced and electronically depleted vdW gaps contrast clearly from the rest of the resonantly bonded crystal, and thus diffract strongly.

Now onto Figure 4.3 (b), following a similar reasoning, the additional features appear approximately at distances $\Delta4'$, $\Delta5'$, and $\Delta6'$ from the CSL(222) reflections. These distances coincide with $1/4$, $1/5$, and $1/6$ of the distance $\Delta1'$ respectively. Therefore, in real space,

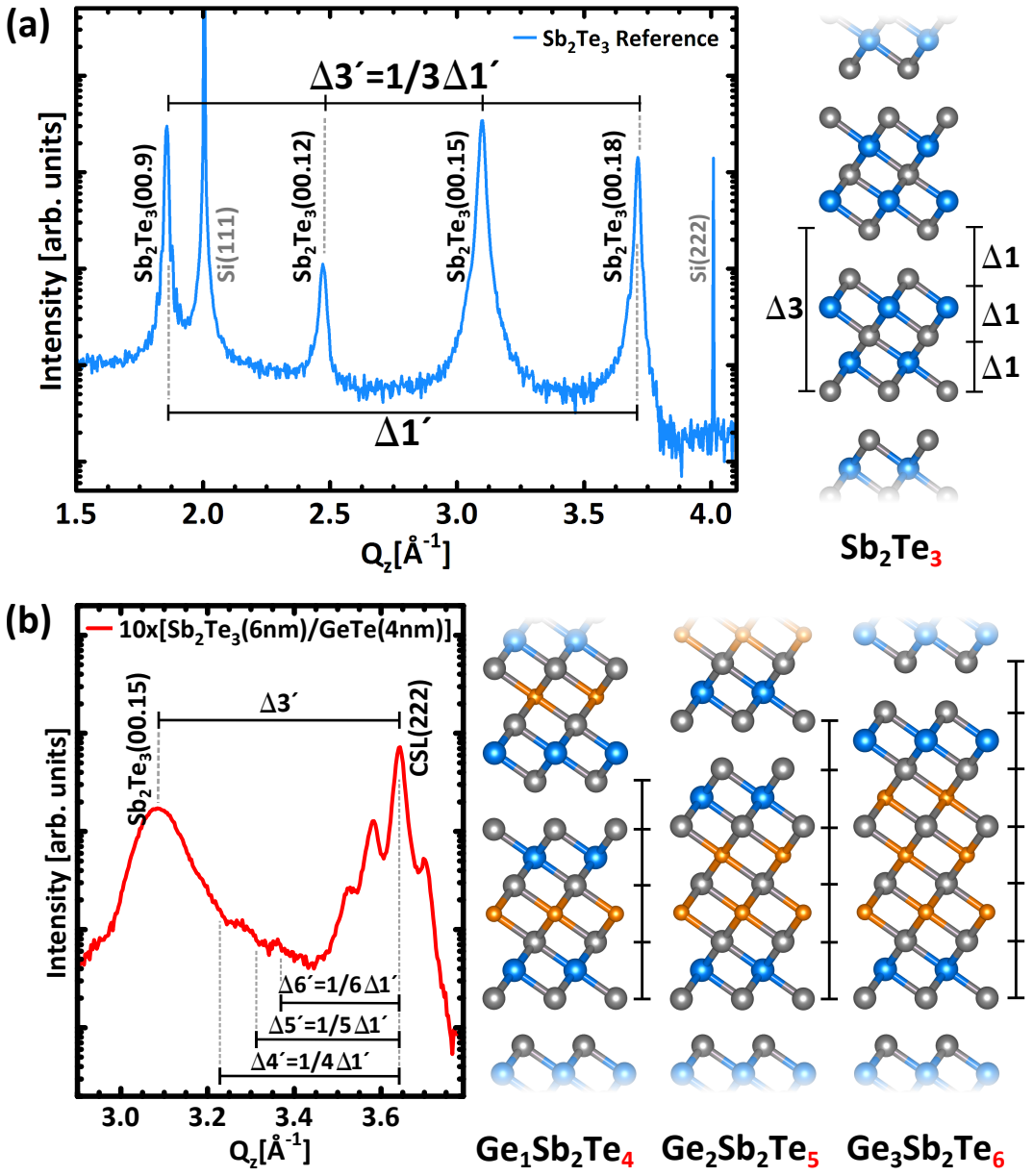

Figure 4.3: (a) Symmetric $\omega - 2\theta$ XRD spectrum from reference Sb_2Te_3, with the spacing between consecutive peaks $\Delta 3'$ highlighted as the third of $\Delta 1'$, the distance between Sb_2Te_3(00.9) and Sb_2Te_3(00.18). Corresponding periodic structures in the Sb_2Te_3 crystal are shown on the right hand side. (b) Zoomed viewgraph of Figure 4.2 around $Q_z = 3$ and $3.5\,\text{Å}^{-1}$, showing the additional features at distances $\Delta 4'$, $\Delta 5'$, and $\Delta 6'$ from CSL(222), corresponding respectively to 1/4, 1/5, and 1/6 of $\Delta 1'$. Corresponding GST structures are shown on the right hand side.

these features are likely to originate from vdW gaps appearing each 4, 5, or 6 Te sublattices; in other words, structures of the same size as hexagonal $Ge_1Sb_2Te_4$, $Ge_2Sb_2Te_5$, and $Ge_3Sb_2Te_6$.[118] Such structures are depicted in Figure 4.3 (b). These features are the first hints showing that the film deposited may not be exactly the intended GeTe / Sb_2Te_3 superlattice, intermixing is likely to occur between the two compounds.

Understandably, the interpretation presented here is simplified to highlight the link between these features and the distances between vdW gaps. The measured peaks are however extremely broad and shifted with respect to the proposed positions. In fact, the position of these features should not be expected to match perfectly $\Delta 4'$, $\Delta 5'$, and $\Delta 6'$, because the average Te sublattice periodicity in these GST blocks differs from the average of the whole CSL, they are not perfect commensurate structures. As for the broadness of the peaks, it is worth to keep in mind that XRD is sensitive to repeated periodic structures (in the electon density), whereas these GST blocks are intercalated between Sb_2Te_3 quintuple layers, and never successively repeated. Therefore, the Fourier transform of such structures can only yield broad features, even in an ideal case. In addition to this, there is of course the effect of thickness fluctuations. The fact that all three $Ge_1Sb_2Te_4$, $Ge_2Sb_2Te_5$, and $Ge_3Sb_2Te_6$ block sizes are found is quite telling of the level of dispersion and roughness still present in these CSLs.

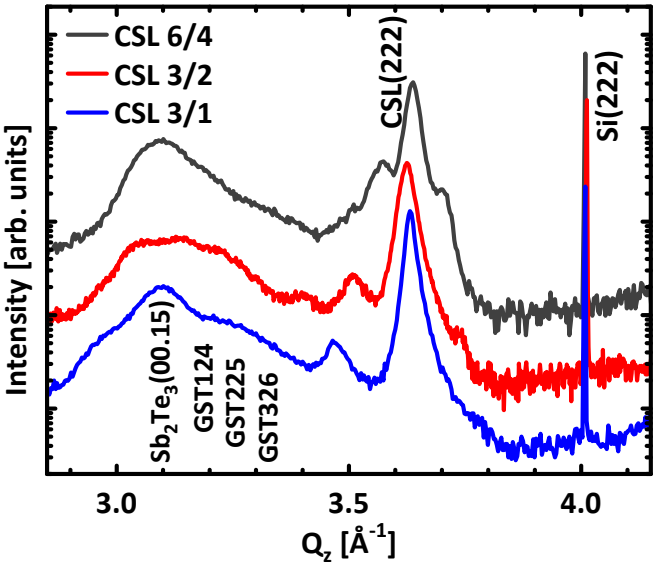

Figure 4.4: Comparison between XRD spectra acquired on CSL 6/4, 3/2, and 3/1.

Equipped with the knowledge to interpret the XRD spectra of these structures, CSLs grown with different stackings and sublayer thicknesses can be compared, the intermixing can be assessed in each case. Because the phase-change properties of CSLs are predicted to be linked to the interfaces between GeTe and Sb_2Te_3, an effort was devoted to

reduce the thickness of each sublayers, increasing the proportion these interfaces occupy in the film. Three selected CSL are shown in Figure 4.4, with sublayers thicknesses reduced from CSL 6/4 down to 3/1, all of which start with Sb_2Te_3 as their first layer. As intended, the superlattice satellite peaks shift away from the main peak with decreasing thickness. More surprisingly, although CSL 6/4 and 3/2 share the same GeTe/Sb_2Te_3 ratio, the position of the CSL(222) peak changes, indicating that the average composition differs. Therefore, the relationship between the out of plane lattice spacing and the sublayer thicknesses may not be simply linear. As for the Sb_2Te_3 and GST reflections, the relative intensity of these feature changes with the stacking. GST reflections seem to become more intense as the sublayer thickness decreases, showing that intermixing is localized at the interfaces. The intensity of these reflections also seem to be further increased in CSL 3/2, that is more rich in GeTe. And this is already a first hint that the intermixing is occurring primarily during the deposition of GeTe.

Intermixing is further investigated by Raman spectroscopy, which can discriminate between the different materials, regardless of their arrangement into the CSL. The spectrum acquired on a $15\times[Sb_2Te_3(3\,nm)/GeTe(1\,nm)]$ CSL (CSL 3/1) is shown in Figure 4.5 (black curve), along with reference spectra acquired on GeTe (orange), Sb_2Te_3 (blue), and $Ge_3Sb_2Te_6$ (red) films grown by MBE as well. Strong similarities are immediately observed between the CSL and Sb_2Te_3, all four modes at 46.3, 69.2, 111.6, and 166.4 cm^{-1} are reproduced. These two spectra are distinguished from each other by overall broader modes for the CSL. The mode at 69.2 cm^{-1} is also visibly less intense, while the mode at 166.4 cm^{-1} is strengthened to 170.4 cm^{-1}.

In contrast, the two modes from GeTe at 80.1 and 121.4 cm^{-1} are not observed at all in the CSL spectrum. Instead, the asymmetric shoulder at 103.8 cm^{-1} is assigned to the GST Raman mode found at the same position. In this specific case, with GeTe sublayers with a thickness of only 1 nm, the Raman data seems to indicate that all the GeTe deposited is intermixed into GST. All the Raman modes observed are summarized in Table 4.1.

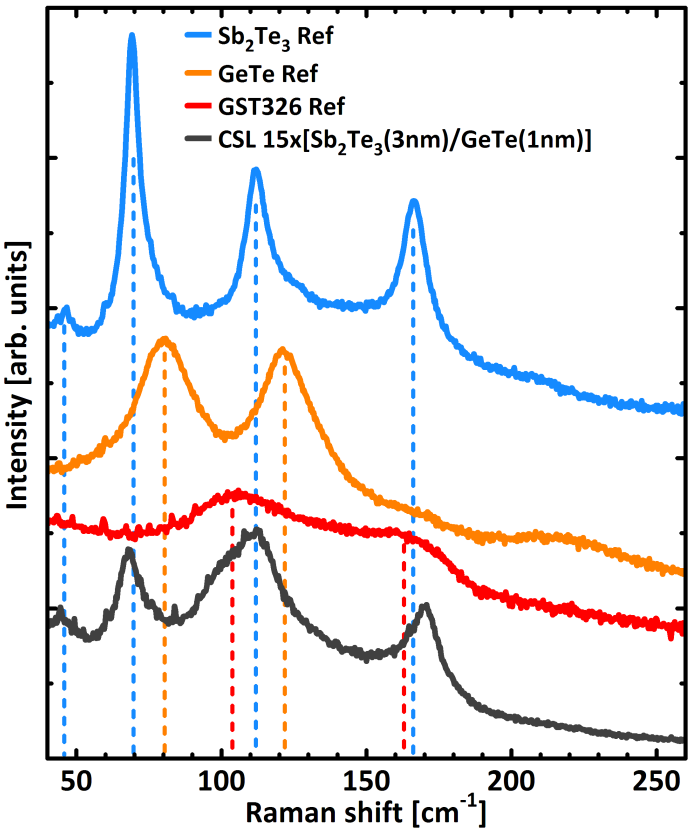

Figure 4.5: Raman spectrum acquired on the CSL 3/1 with a 633 nm laser in $z(y,xy)-z$ geometry. Spectra are acquired on GeTe, Sb_2Te_3 and $Ge_3Sb_2Te_6$ films and shown as reference.

	Raman modes $[cm^{-1}]$			
Sb_2Te_3 [119]	$E_g(1)$	$A_{1g}(1)$	$E_g(2)$	$A_{1g}(2)$
	46	69	112	166
GeTe [32,107]	-	E	A_1	-
	-	80	121	-
GST [120]	-	-	E_g	A_{1g}
	-	-	105	161
CSL	$E_g(1)$	$A_{1g}(1)$	$E_g(2)$	$A_{1g}(2)$
	45	68	105 111	161 170

Table 4.1: Table listing Raman modes observed in crystalline Sb_2Te_3, GeTe, $Ge_3Sb_2Te_6$, and CSL 3/1 films. Each Raman mode is associated to its corresponding Mulliken symbol.

4.1.2 Evidence of intermixing through scanning transmission electron microscopy

In light of these results, the CSLs are characterized by STEM to resolve the structure and understand how intermixing occurs. In collaboration with J. Momand,[†] M. Verheijen,[‡] and B. J. Kooi,[†] cross-sectional STEM micrographs are acquired in HAADF mode on the CSL 3/1, as exemplified by Figure 4.6. The HAADF detector is sensitive to the weight of the species in the atomic columns, allowing to clearly distinguish the lighter Ge atoms from the heavier and brighter Sb or Te.

As illustrated in Figure 4.3, Sb_2Te_3, GeTe, and GST all share a similar structure with one sublattice filled with Te, and the other one containing Sb, Ge, or vacancies. In the CSL, this Te sublattice is shared throughout the whole structure. The fact that contrast can be perceived on the other sublattice already demonstrates that Ge, Sb, and vacancies are preferentially arranged into separate layers. In this configuration, the empty vdW gaps contrast strongly, as they do not produce any intensity. In this figure, the number of Te layers in-between vdW gaps is counted and noted in blue. The blocks of five bright atoms, counted as three Te layers, are undoubtedly identified as the Sb_2Te_3 blocks. The alternated dark and bright spots are the areas where GeTe is concentrated. The peculiarity about these GeTe blocks is that they don't have a direct interface with Sb_2Te_3, they seem to be encapsulated by $-[Te-Sb-Te]$ endpoints, effectively recreating the structures of hexagonal GST compounds.

It is noteworthy to be reminded that the intended structure consisted in 1 nm of GeTe and 3 nm of Sb_2Te_3, as illustrated in Figure 4.7. Each Sb_2Te_3 QL being 1 nm thick, three of them are expected to be deposited in the structure. But in the micrograph, these blocks are observed by pairs only. One Sb_2Te_3 layer forms bonds with GeTe and intermixes into GST, maintaining vdW interfaces in the whole CSL.

While this gives a representative description of the CSL, fluctuations and defects are observed. The thickness of the GST compounds varies between that of $Ge_1Sb_2Te_4$ (labeled as 4), $Ge_2Sb_2Te_5$ (5), and $Ge_3Sb_2Te_6$ (6) (and even $Ge_4Sb_2Te_7$, labeled as 7), which is consistent with the additional features observed by XRD in Figure 4.3. There are also imperfections in the formation of vdW gaps, as highlighted in Figure 4.6 by the red frames a and b. While they seem to be quite consistently continuous between the Sb_2Te_3 blocks, discontinuities are often observed at the interfaces with the GST blocks (Figure 4.6 red

[†]Zernike Institute for Advanced Materials, Groeningen, the Netherlands
[‡]Eindhoven University of Technology, Eindhoven, the Netherlands

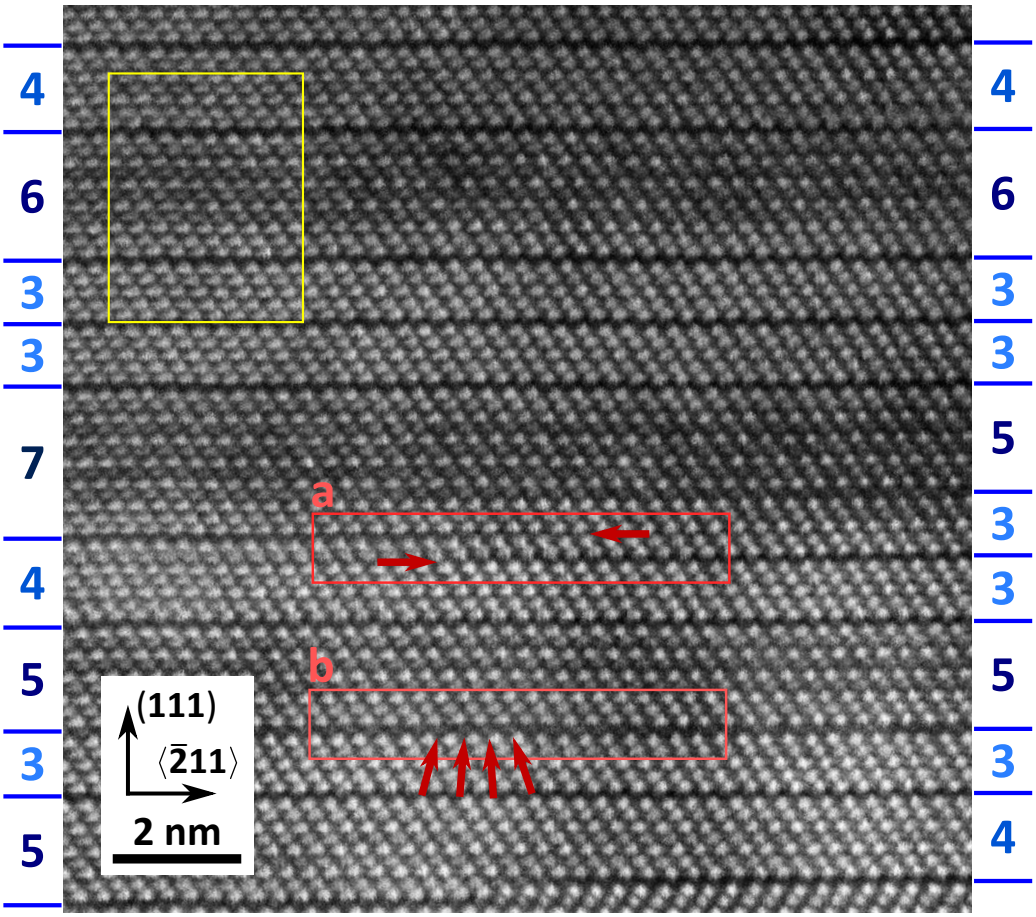

Figure 4.6: Cross-sectional STEM micrograph in HAADF mode from the CSL 3/1 (STEM imaging was carried out by J. Momand and B. J. Kooi from the Zernike Institute for Advanced Materials, and M. Verheijen from the Eindhoven University of Technology). The vdW gaps are underlined by blue horizontal lines both on the left and right sides of the image, the number of Te sublayers between vdW gaps is counted. Darker shades of blue indicate a thicker block. The red frames a and b highlight the two kinds of defects in the vdW gaps. The yellow frame is discussed in Figure 4.8.

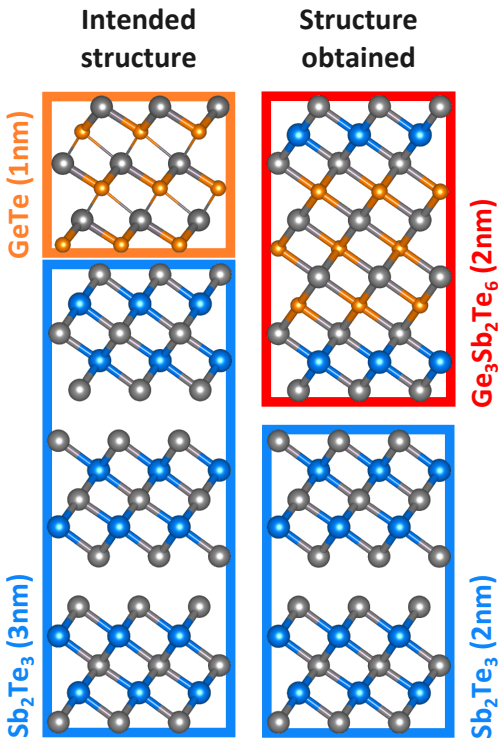

Figure 4.7: Schematic models of the structure initially intended, and a representative model of the CSL obtained, observed by STEM.

frame *a*). There are also instances where the vdW gaps don't seem to be completely empty, some intensity can still be resolved (Figure 4.6 red frame *b*). Those two defects could be interpreted as being one and the same discontinuity but viewed from another perspective, along the depth of the cross-section. Because of these defects, the thickness of the blocks can change, leading to different numbers of Te sublattice counted on each side of the image. Such defects can be expected to greatly impact the superstructure reflections linked to these vdW gaps in the XRD spectrum.

4.1.3 Growth model for GeSbTe alloy formation in superlattices

Coming back to the TEM image of Figure 4.6, an asymmetry in the $-[Te-Sb-Te]$ endpoints of the GST blocks is observed, as illustrated in the intensity profile of Figure 4.8. While the endpoints toward the bottom contains three atomic layers of equal intensity, the one on top has a darker layer in-between the two brighter Te layer. Yet the intensity of that layer is still higher compared to one of the Ge layers inside the GST block. This indicates that the bottom endpoint contains pure Te and Sb, whereas the top one has some Ge intermixed on its Sb sublattice. This phenomenon is consistently found throughout the CSL structure, especially when the Sb_2Te_3 block right underneath does not show apparent defects.

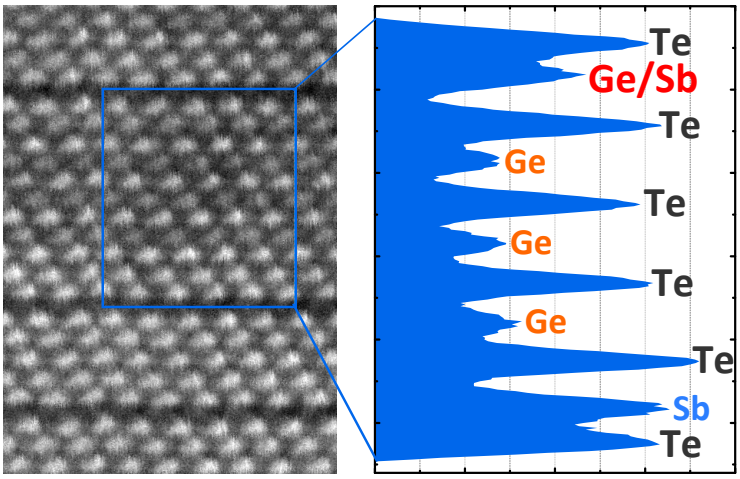

Figure 4.8: Detailed view of area delimited by yellow frame in Figure 4.6, with the intensity profile across a GST block, integrated horizontally in the blue frame (TEM imaging was carried out by J. Momand and B. J. Kooi from the Zernike Institute for Advanced Materials, and M. Verheijen from the Eindhoven University of Technology).

On the basis of these observations, a growth model is proposed, explaining step by step the formation of the GST blocks in the CSL. This model is schematically shown in Figure 4.9. On the left hand side, the diagram starts with two layers of Sb_2Te_3. As the deposition of GeTe is initiated, the impinging GeTe is able to bind with the topmost Sb_2Te_3 block. This could happen either directly, despite the passivated vdW surface, or possibly at defect sites or from the sides of Sb_2Te_3 layers that are not fully completed. Once bound, the top surface is most likely Te terminated, as the Te surface has been predicted to be much more stable than a Ge surface.[24] At this point, a GST compound is already formed, but the Ge atoms sit at the edge of the GST structure, whereas it would be more favorable energetically for them to be at the center.[118] Considering that growth is performed at a temperature of 230 to 250°C, enough thermal energy is provided for Ge and Sb atoms to exchange their positions, pushing some Sb toward the newly formed surface. An analogy can be drawn with the use of Sb as a surfactant for the growth of pure Ge.[121] This process continues as more GeTe is deposited, resulting into a natural GST structure at the end of the deposition of what was first intended as a GeTe sublayer. This structure then conveniently possesses a weakly interacting top surface that can host the growth of the following Sb_2Te_3 sublayer.

According to this model, the formation of GST would mainly occur when GeTe is deposited on top of Sb_2Te_3, and only the topmost QL of Sb_2Te_3 would intermix with GeTe. The asymmetrical contrast observed in Figure 4.8 is well accounted for in this model: The top $-[Te-Sb-Te]$ endpoint contains an intermixed Ge/Sb layer because of the imperfect exchange process between Ge and Sb, as not all the Ge atoms are able to reach the

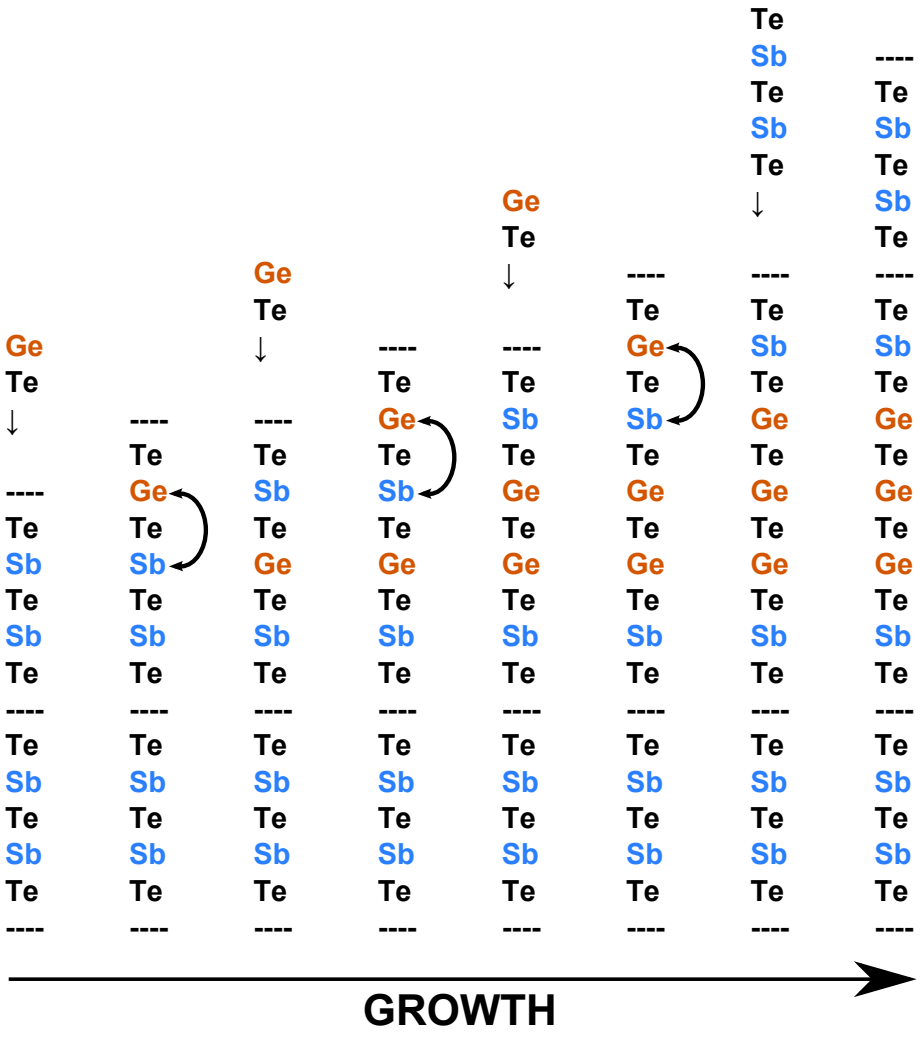

Figure 4.9: Schematic step by step model of the process by which ordered GST is formed during the deposition of GeTe onto Sb_2Te_3 in the CSL structure.

center of the structure. The bottom endpoint does not suffer from intermixing, because once the Ge atoms have reached the center of the structure, there is no driving force to push them further down.

4.1.4 Superlattice annealing experiments

To exacerbate and study this tendency for GeTe and Sb_2Te_3 in the CSL to intermix into GST, an annealing experiment is devised where pieces of the same CSL 3/1 are brought to 250, 300, or 400°C for 30 minutes in each case, using a rapid thermal annealing equipment. Figure 4.10 (a) reports a symmetric XRD $2\theta - \omega$ scan for each of the pieces after annealing. With increasing annealing temperature, the XRD features related to Sb_2Te_3 and the CSL satellite peaks both disappear. Instead, the features linked to $Ge_1Sb_2Te_4$ are strengthened, until they become the only features observed after the annealing at 400°C. Higher order superstructure peaks are also detected, like GST(00.16) and (00.24) at $Q_z = 2.78$ and 4.11 $Å^{-1}$. Figure 4.10 (b) shows a high resolution STEM cross-sectional image of the resulting structure after annealing at 400°C. All the Sb_2Te_3 have indeed disappeared, removing the superlattice modulation from the structure. The entire CSL has transformed into hexagonal $Ge_1Sb_2Te_4$ with only few defects. As a side note, the twinning that can occur within the Sb_2Te_3, CSL, or GST structures is well illustrated in this micrography, in the top two GST blocks and the bottom one (as highlighted by yellow chevrons).

While intermixing has been supposed to be limited during growth to only the topmost Sb_2Te_3 block, the annealing clearly allowed the Ge atoms to diffuse further down into the other QLs. This highlights an intrinsic thermodynamic tendency toward intermixing, above a certain energetical barrier. Interestingly, the hexagonal $Ge_1Sb_2Te_4$ structure obtained by annealing also corresponds to the average composition expected of the CSL 3/1. Further annealing experiments on other CSLs of $Ge_2Sb_2Te_5$ or $Ge_3Sb_2Te_6$ average composition could quickly tell whether the CSL intermixes toward its average composition, or if $Ge_1Sb_2Te_4$ is just the more stable structure. The former case would be especially interesting, because the control of the GST composition is a delicate operation in MBE growth. Considering the very high quality of the GST film obtained presently, the growth and annealing of a CSL could be a viable technique to produce high quality hexagonal GST films. This annealing experiment has also important technical implications for CSLs: The active region should not be subjected to effective temperatures above 300°C downstream on the process lines for the fabrication of devices. Otherwise, the intercalation of diffusion barriers should be considered between each sublayer.

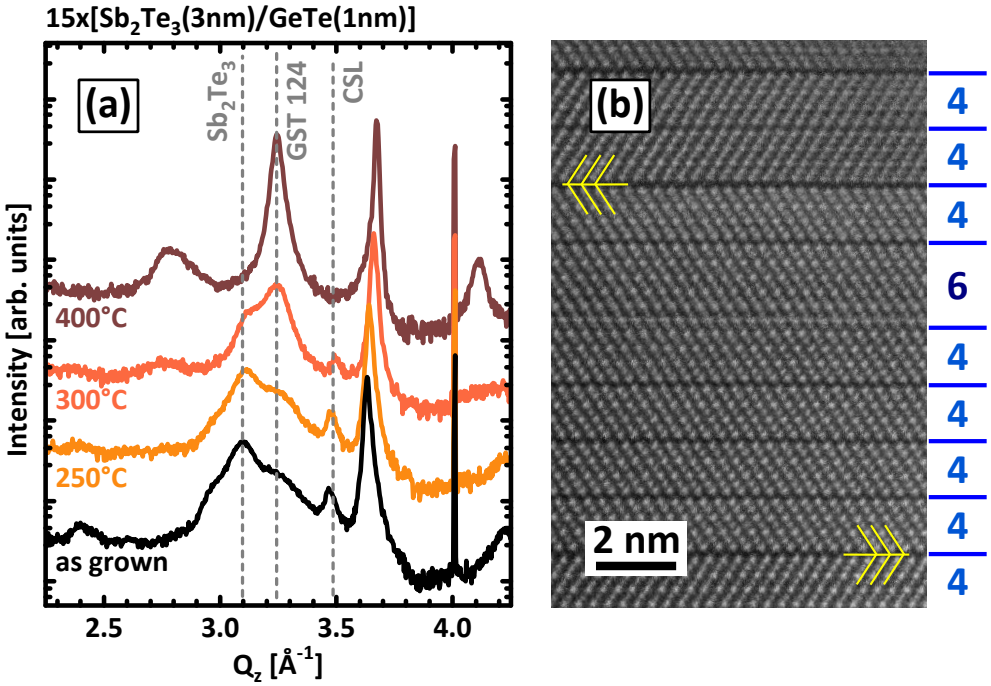

Figure 4.10: (a) Symmetric $2\theta - \omega$ XRD scans on different pieces of the same CSL, as grown, and after annealing at 250, 300, or 400°C for 30 min. (b) HR-STEM cross-section micrography of the CSL after the 400°C annealing. Twinning is evidenced with yellow arrows (TEM imaging was carried out by J. Momand and B. J. Kooi from the Zernike Institute for Advanced Materials).

4.1.5 Interrupted growth experiments

The question of intermixing is very important because there are several models describing how switching occurs in the CSL, and some of them are based on the assumption that there is a well defined interface between GeTe and Sb_2Te_3. The four leading model structures at the time of redaction are reproduced in Figure 4.11.[51] Compared with the STEM data of Figure 4.6, the model that corresponds the best is the Kooi model,[122] with its characteristic $-[Te-Sb-Te]$ endpoints encapsulating the GeTe layers. Close to defective vdW layers, structures similar to the ferro-GeTe model cannot be excluded, but the Kooi structure remains the more representative model.

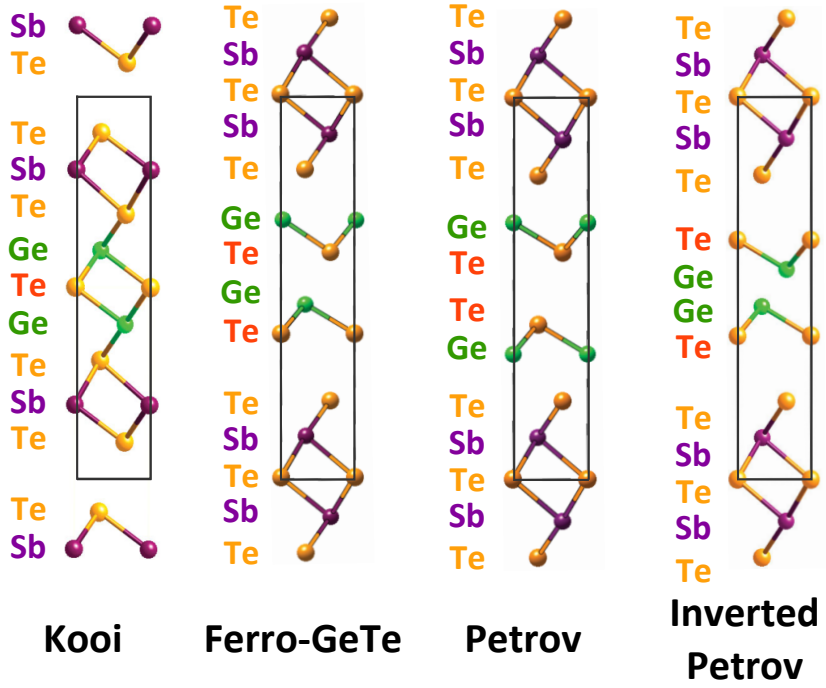

Figure 4.11: CSL model structures for CSL with 2 BLs of GeTe between Sb_2Te_3 blocks (Figure adapted from Tominaga *et al.*[51]).

The two other models make the assumption of GeTe blocks separated by vdW gaps from Sb_2Te_3, homopolar Ge−Ge bonds, or vdW gaps inside the GeTe block. None of these features are observed by TEM in the MBE grown CSL. Admittedly, the Petrov and inverted Petrov models can only make sense when considering a GeTe block with specifically 2 BLs, while the investigated CSL is intended to contain GeTe blocks that are 3 BLs thick. Nevertheless, as shown in Figure 4.6, 2 BLs thick GeTe blocks do very well occur in the studied structure because of dispersion and defects in the periodicity. And when these 2 BL thick GeTe blocks do occur, the Kooi structure predominates again. The other structures could maybe be obtained using other fabrication methods or recipes. Yet, the CSL

annealing experiments shown in Figure 4.10 still demonstrated that the formation of Kooi structures is the most favorable thermodynamically. The other models would have to be considered meta-stable.

In an attempt to prevent intermixing in the CSL during growth, interruptions are implemented in the recipe between the deposition of each sublayer. The new growth procedure is schematically presented in Figure 4.12. After the deposition of each sublayer, the Ge or Sb shutter is closed, while the Te shutter is left open. The initial idea is that subjecting the sample to a Te flux will help all the remaining Ge or Sb species from the previous sublayer to react before the surface is exposed to the other species of the next sublayer. In other words, avoid that unreacted Ge, Sb, and Te species are found at the surface all at the same time. Such interruptions of 2, 5, and 10 minutes were applied, and symmetric $2\theta - \omega$ XRD scans on each of these resulting CSLs are shown in Figure 4.13.

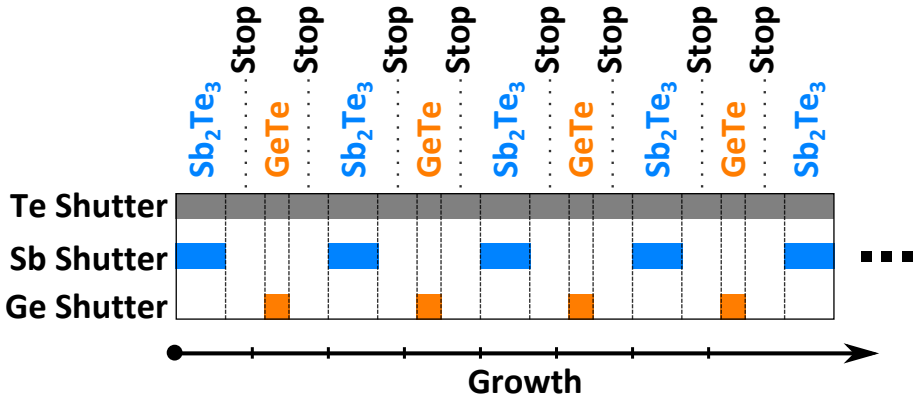

Figure 4.12: Schematic showing the growth procedure with interruptions between the deposition of each sublayer.

Growth interruptions certainly have a visible effect on the XRD spectrum and underlying structure of these CSL. The position of the CSL(222) peak is shifted towards higher Q_z values, indicating that the average composition is richer in Sb. The spacing between the CSL satellite peaks shrinks from $\Delta 1' = 0.162$ to $\Delta 2' = 0.134\,\text{Å}^{-1}$, which corresponds to a substantial increase in the average CSL periodicity in real-space from 3.9 to 4.7 nm. Together with the Sb rich composition, this indicates that growth interruptions could incentivize the completion of unfinished Sb_2Te_3 layers. The intensity ratio between the reflections from the different GST compounds is changed, favoring the $Ge_1Sb_2Te_4$ composition, which also falls in line with a Sb rich average composition in the CSL. An increase in Sb content also translates into more frequent vdW gaps, since hexagonal $Ge_1Sb_2Te_4$ has one vdW layer each seven atomic layers, versus eleven for the Ge rich $Ge_3Sb_2Te_6$. This increased frequency of vacancy layers also contributes to the increase in the GST sublayer thickness.

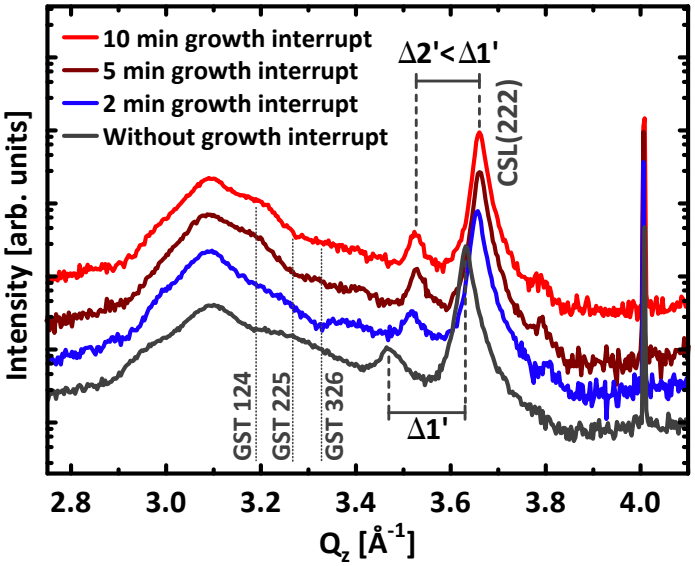

Figure 4.13: XRD symmetric $2\theta - \omega$ spectra acquired on CSLs 3/1 grown with growth interruptions of 2, 5, and 10 minutes between each sublayer. The spectra for the CSL 3/1 without growth interruption is also shown for comparison.

Regarding the initial objective to suppress intermixing, growth interruptions do not seem to be the right solution. Reflections from GST compounds are still clearly measured. Nevertheless, their implementation after the growth of Sb_2Te_3 sublayers could yield a positive effect, by completing existing QLs and fixing the Sb atoms. But following the deposition of GeTe, growth interruptions are unjustified. They could even cause a detrimental etching of the freshly deposited GeTe.[123]

In addition, the experiment did highlight some noteworthy considerations: The deposition of GeTe on top of Sb_2Te_3 is likely to differ depending on whether the last QL is fully completed or not. As hinted in Figure 4.6, there are instances where two successive GST blocks are found in the CSL, which is incompatible with the idealized growth model presented in Figure 4.9. This could be caused by the interaction of GeTe with both an unfinished Sb_2Te_3 QL, and the partially uncovered QL below. The fact that layer by layer growth cannot be guaranteed in the CSL implies that there could also be two or more stacked QLs coalescing at the same time. In any case, it would still be beneficial to use a tool such as a well calibrated QMS to determine and adjust the exact growth rate, in order to aim for the full completion of each sublayer.

Preventing intermixing while maintaining the outstanding crystalline quality of the MBE grown CSL remains a major step that would help to validate or dispute the current models describing the structure and switching mecanism inside these CSL. Another possible solution to explore would be the growth at lower substrate temperatures, down to

150 − 200°C for example. The temperature could first be increased to grow a first layer of Sb_2Te_3 and ensure a good epitaxy on silicon, to be then lowered afterwards for the deposition of the subsequent layers.

4.1.6 X-ray reflectivity for superlattice characterization

XRR is a valuable tool to determine the density, thickness, and roughness of the different materials composing a thin film. But applied to the CSLs, the technique involves one major *caveat* that is important to mention: The densities of GeTe and Sb_2Te_3 are too similar (6.07 and 6.27 g/cm^3 respectively), the one of GST compounds is also somewhere in-between those values. In these conditions, the different sublayers cannot be discriminated using XRR and only the total thickness can be measured. An average thickness of the repetition unit can then be deduced, knowing the number of periods. To illustrate this issue, the XRR spectrum is acquired on the CSL 3/1, and reproduced three times in Figure 4.14. It is first fitted in Figure 4.14 (a) using the intended structure with 3 nm of Sb_2Te_3 and 1 nm of GeTe. In Figure 4.14 (b), the structure resolved by TEM is used, which corresponds to 2 nm of Sb_2Te_3 and 2 nm of $Ge_3Sb_2Te_6$, where one QL of Sb_2Te_3 (1 nm) intermixes with the 1 nm of deposited GeTe into the 2 nm of GST (as shown in Figure 4.7). Finally in Figure 4.14 (c), a ``tongue-in-cheek´´ example is shown where the whole CSL is fitted with only one single GST slab with the same total thickness than the other two CSL structures. Despite these very different models, all three simulated spectra fit the data similarly well. XRR does not corroborate one model over the others. Being aware of this limitation, XRR can still be used to measure reliably the total thickness, and give an estimate of the interface roughness between the film and the substrate, or with the capping layer.

To access the thickness of each sublayer, TEM can provide a more reliable answer. Using XRR, the growth rates of each compound in the CSL can also be deduced for a given set of growth parameters, by growing one series of calibration samples where only the deposition time of one of the compounds is changed. The total thickness in each sample measured by XRR can then be plotted versus the adjusted growth time, and fitted linearly. The growth rates of the two compounds are then simply given by the slope and the intercept of the fit.

Layer		Density $[g/cm^3]$	Thickness $[nm]$	Roughness $[nm]$
Si_3N_4 capping		3.1	11.94	1.1
$15\times$	GeTe	6.07	0.96	1.28
	Sb_2Te_3	6.27	2.8	1.03
Si substrate		2.33	–	0.25

Layer		Density $[g/cm^3]$	Thickness $[nm]$	Roughness $[nm]$
Si_3N_4 capping		3.1	11.9	1.1
$15\times$	$Ge_3Sb_2Te_6$	6.13	1.96	1.28
	Sb_2Te_3	6.27	1.8	1.1
Si substrate		2.33	–	0.25

Layer	Density $[g/cm^3]$	Thickness $[nm]$	Roughness $[nm]$
Si_3N_4 capping	2.97	11.8	1.1
$Ge_3Sb_2Te_6$	6.12	56.4	1.13
Si substrate	2.33	–	0.25

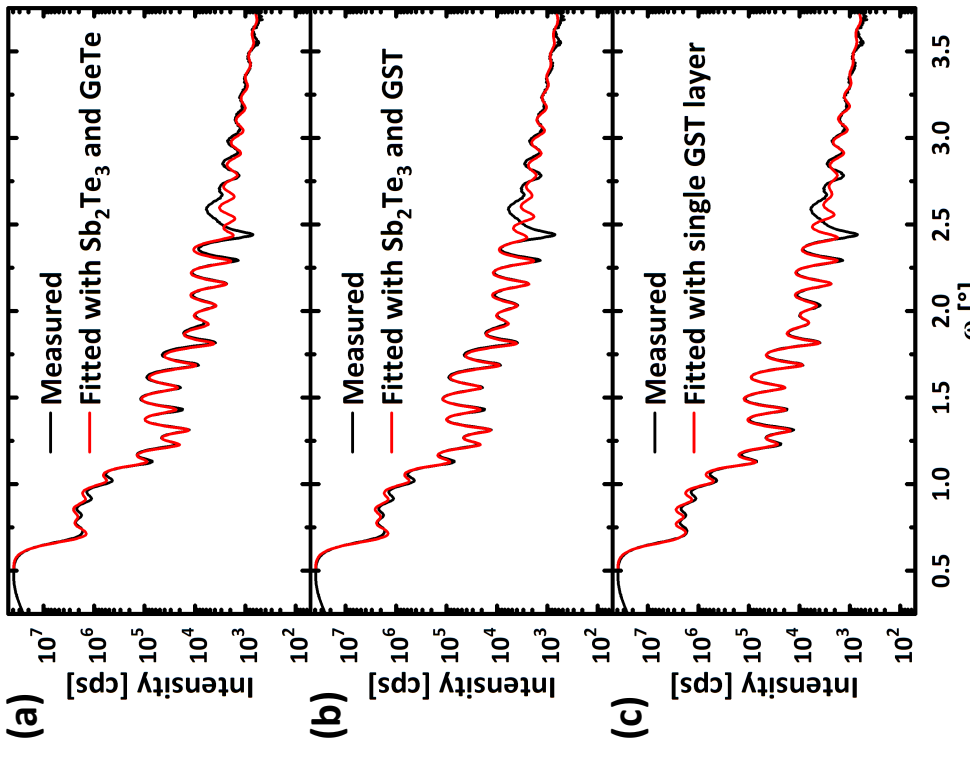

Figure 4.14: XRR spectrum of the CSL 3/1, fitted with (a) Sb_2Te_3 and GeTe, (b) Sb_2Te_3 and GST, or (c) only with one block of GST.

4.2 The case of in-plane lattice spacing variations during superlattice growth

Using RHEED, the in-plane lattice spacing at the surface of the film can be calculated from the RHEED streak spacing and monitored during growth. Applied to CSLs, a changing lattice spacing is observed, depending on which sublayer is being deposited. This is illustrated in Figure 4.15 for the CSL 3/3. The first Sb_2Te_3 is grown fully relaxed on the passivated surface,[84] and a value matching the Sb_2Te_3 reference is measured. As the deposition of GeTe is initiated, the lattice spacing starts to shrink towards the lower value of GeTe, or GST compounds. But before a plateau is reached, growth is switched to the deposition of Sb_2Te_3, the lattice spacing expands back. And before the value for Sb_2Te_3 is reached again, growth is switched back once more to the deposition of GeTe, and so forth. From the second repetition onward, the lattice spacing follows a stationary oscillation between the two extreme values at the end of the growth of each sublayer.

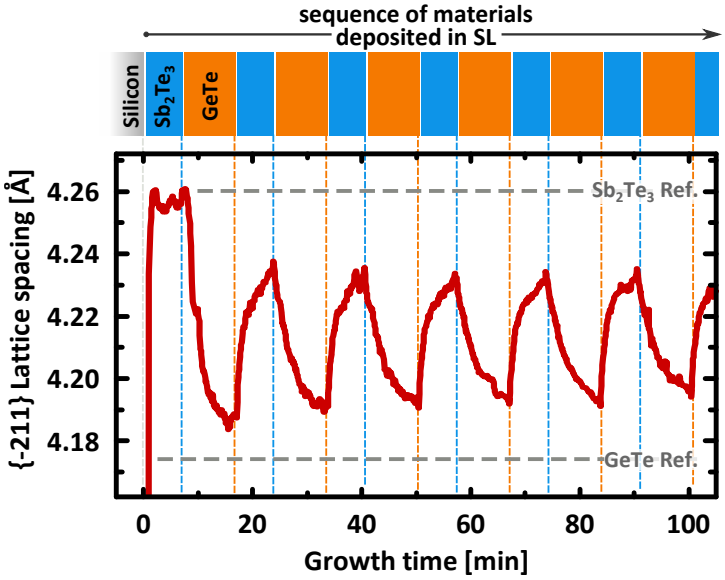

Figure 4.15: <$\bar{2}$11> in-plane lattice spacing oscillations over time calculated from RHEED pattern acquired during CSL 3/3 growth.

In an ideal pseudomorphic 3D case, the epilayers are first strained to adapt to the lattice of the substrate. The value measured by RHEED would therefore not be expected to change until the critical thickness for plastic deformation is reached, at which point the film would relax, but accommodated by dislocations. On the other hand, in the case of 2D materials, the lattice spacing should rapidly jump from one fully relaxed value to the other in a step-function fashion, as illustrated in the left-hand side panel of Figure 4.16. In

the CSL, which is nominally considered as a 2D system, the way that the in-plane lattice spacing changes during growth is highly unusual, as it differs from both these 2D and 3D cases.

To be more precise, it is the behavior between the sublayers inside the CSL that differ from the stereotypical 2D and 3D models. At the interface between the very first Sb_2Te_3 sublayer and the passivated silicon substrate, a true 2D behavior is observed, with the in-plane lattice spacing measured by RHEED directly jumping from silicon to the fully relaxed value of Sb_2Te_3. But the two materials are clearly mismatched at this interface; the critical thickness for plastic relaxation is of the order of one atomic layer, and the film will not try to conform to the lattice of the substrate. A similar scenario would also occur in highly mismatched 3D heteroepitaxy, but would lead to a case of domain matched epitaxy with formation of in-plane rotational domains to alleviate strain. Here, owing to the passivation of the substrate and to the 2D nature of Sb_2Te_3, such domain matched orientations are suppressed.

Therefore, it would be more correct to compare the observations in the CSL with the hypothetical scenario of a 3D heterostructure that is free-standing on a passivated surface. Such cases have not been observed experimentally in the literature to our knowledge, but the expected behavior can easily be predicted in a "Gedankenexperiment": the very first sublayer is deposited fully relaxed, since its in-plane lattice parameter is not dictated by the substrate. And when the second dissimilar 3D material is deposited on top of this first layer, within the elastic domain, both layers are going to strain each other toward a common equilibrium lattice parameter, depending on the thickness of each layer, their crystalline parameters, and their elastic properties. If the growth of such a structure is monitored in real-time by RHEED, the lattice spacing would also oscillate, similarly to the case of the CSL observed experimentally. However, because additional layers will have a decreasing influence on the whole growing structure, as the thickness of the last deposited layer represents an ever smaller proportion of the total film thickness. These oscillations in the lattice-spacing would be quickly dampened. The right-hand side panel of Figure 4.16 shows the lattice spacing variations simulated for the 3D freestanding heterostructure. The details of the model used for the simulation will be described later below, the important point that this simulation shows is the envelope of the dampened oscillations following a shape similar to a power function $y = x^{-1}$. In the case of the CSL investigated, no such dampening is observed. Therefore, although similarities are observed, they cannot be directly assimilated to a case of freestanding 3D heterostructures.

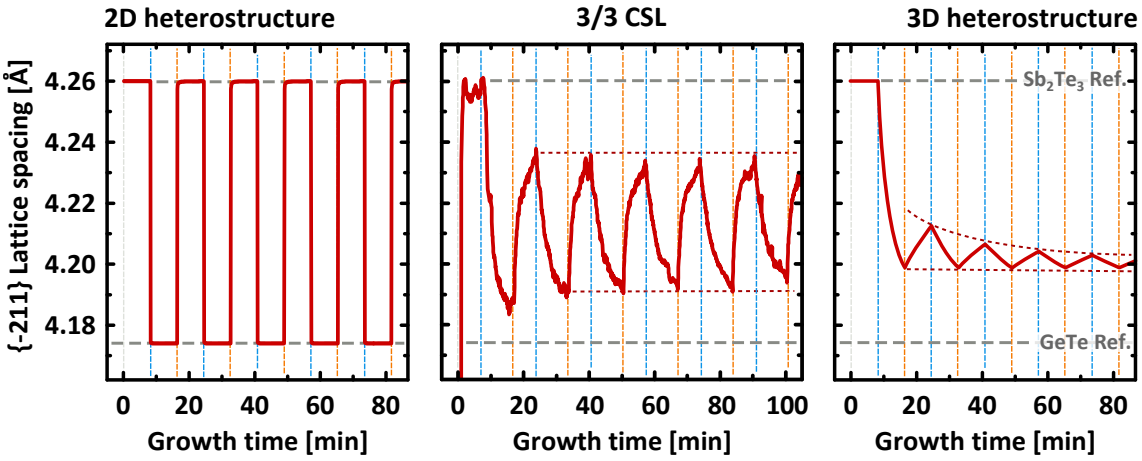

Figure 4.16: Comparison between the lattice spacing oscillations observed by RHEED on the CSL 3/1, and the predicted cases for superlattices composed of 2D and 3D materials. These latter cases are simulated using the spring model imagined by F. Lange and M. Wuttig from the Physikalisches Institut in Aachen.

In order to show that the described phenomenon is reliably reproduced, CSLs with different stacking sequences are grown and monitored with RHEED in the same way. In Figure 4.17 the cases of CSL 3/3, 6/1, and 6/3 are presented. The same kind of oscillations are observed, but the amplitude of the oscillation and central value change depending on the stacking sequence: More specifically, the amplitude of the variation increases with thicker sublayers, and the average value shifts toward the reference values of the compound the CSL is most rich in. On the right-hand side, the distribution of these data points is also shown, with respect to spacing measured. This last panel is to be compared with the data from Figure 4.18. For the moment, it should simply be noted that the measured values during growth by RHEED follow bimodal distributions, and this is especially evident in the case of CSL 3/3 and 6/3.

The next step is to check whether this surface effect observed by RHEED during growth has any influence on the final structure of the CSL after growth. In order to probe the crystalline structure in a purely in-plane direction, the 4 CSLs shown in Figure 4.17 are investigated using grazing-incidence XRD (GID). These measurements have been performed at the ESRF synchrotron by T. Krause[†], G. Li Destri[‡], and M. Hanke[†], looking directly at the in-plane $\{\bar{4}22\}$ reflections, as shown in Figure 4.18.

[†]Paul-Drude-Institut, Berlin, Germany
[‡]European Synchrotron Radiation Facility, Grenoble, France

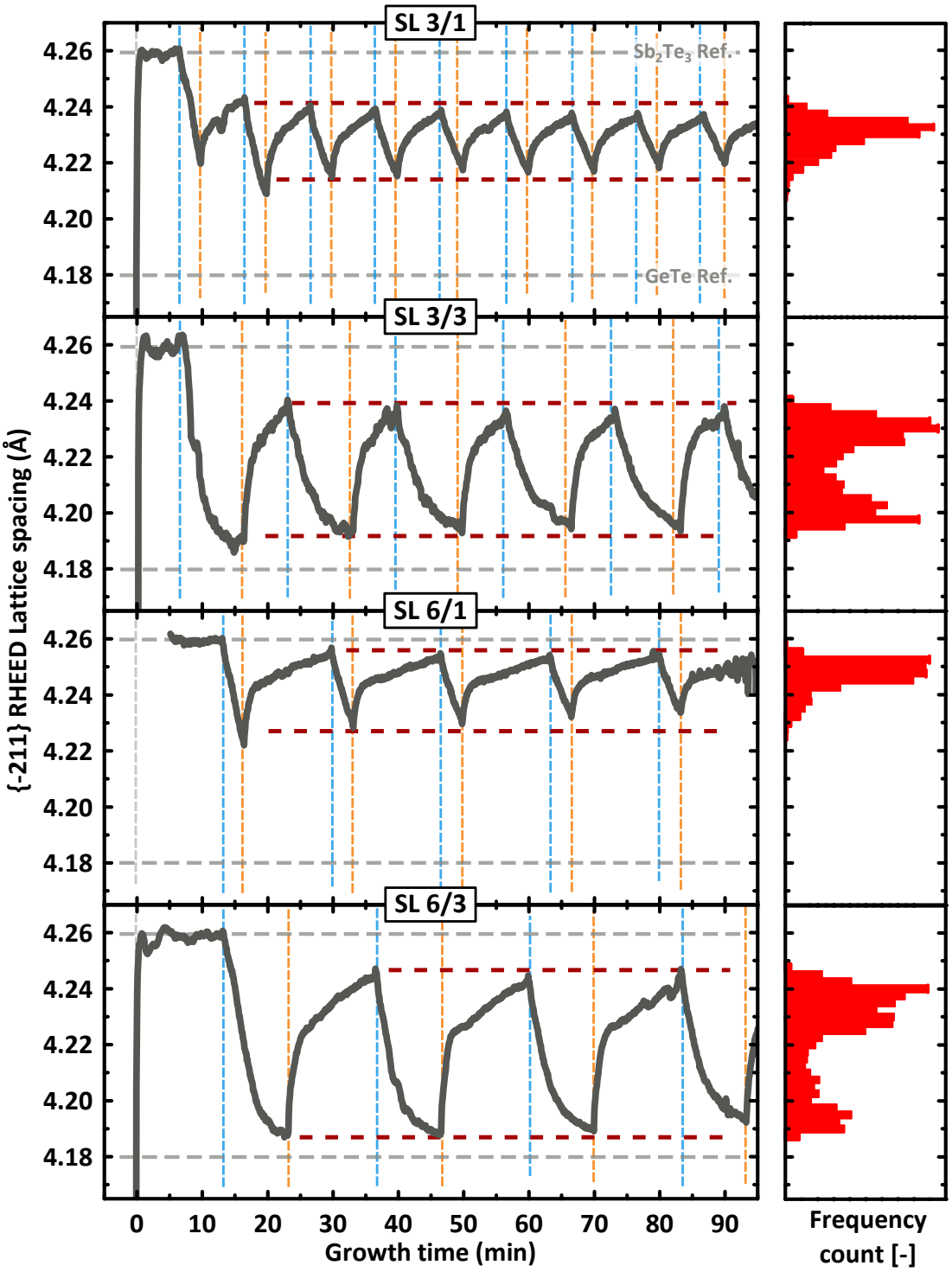

Figure 4.17: RHEED streak spacing oscillations during growth in CSL 3/1, 3/3, 6/1, and 6/3. Depending on the stacking, the average value and amplitude of oscillation changes. In the right hand side panel, the frequency distribution of the measured data points in each case is shown.

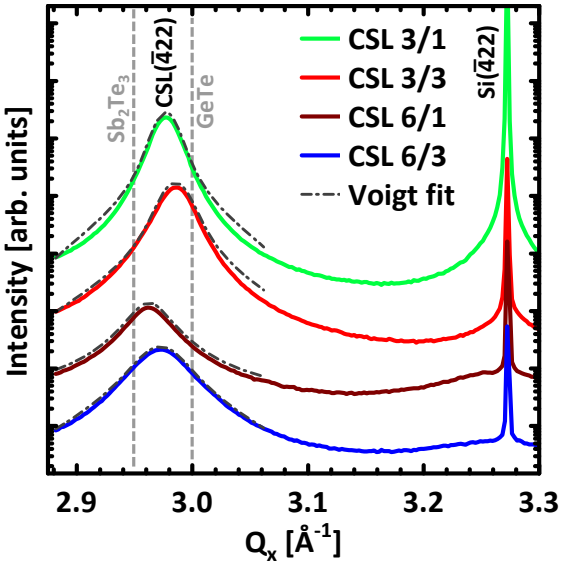

	X_c [Å^{-1}]	FWHM [Å^{-1}]
3/1	2.977	0.025
3/3	2.985	0.031
6/1	2.962	0.037
6/3	2.972	0.048

Figure 4.18: GID spectra around the in-plane CSL{4̄22} reflections for the CSL 3/1, 3/3, 6/1, and 6/3. Each spectra is fitted with a Voigt function, yielding the parameters shown in the right hand side table (GID measurements were carried out by T. Krause and M. Hanke from the Paul-Drude-Institut, and G. Li Destri from the European Synchrotron Radiation Facility).

These spectra feature the substrate peak at $Q_x = 3.27\,\text{Å}^{-1}$, and one peak around $Q_x = 2.97\,\text{Å}^{-1}$ that originates from the CSL. In contrast with the bimodal distribution of the RHEED data acquired during growth (Figure 4.18), the GID reflections are embodied by one single peak. The narrow FWHM of the substrate peak shows that the GID technique has the resolution necessary to discern Sb_2Te_3 from GST, if they were relaxed. This means that the material probed by RHEED at the surface during growth is altered as it is overgrown. This would not be expected to occur in an ideal case of 2D heterostructure, where each relaxed sublayer would keep its own lattice parameter, yielding distinct reflections in the GID spectrum. In fact, the presence of one single reflection is more reminiscent of a case of 3D heteroepitaxy, where the different materials stretch or compress toward one common lattice parameter.

At this point, possible explanations to the observations presented above are evaluated. The first possibility is that the relaxed lattice parameter is shifting due to a change in the composition of the compound induced by intermixing. Indeed, intermixing during the growth of CSLs has been observed and demonstrated in the previous chapter. During deposition, the top surface inevitably gets alternatively more rich in Sb_2Te_3 or GeTe, depending on which material is being deposited. And one could imagine that the in-plane lattice spacing simply shifts one way or the other, as the materials intermix into GST. However, STEM imaging in HAADF mode (Figure 4.6) shows that intermixing is limited

to the interface between GeTe and Sb_2Te_3. With this method, the contrast from the difference in atomic weight between Ge and Sb clearly shows that highly pure Sb_2Te_3 QLs are deposited, only one QL per CSL repetition is intermixed into GST.

Knowing that STEM is a very local technique, and that it involves an elaborate sample preparation procedure that could alter the structure in the sample, those results are corroborated by the XRD and Raman analysis. XRD (Figure 4.3) clearly demonstrates the co-existence of pure Sb_2Te_3 and intermixed GST compounds of different compositions in the CSL, the presence of superlattice features further strengthens this point, and demonstrates that the whole structure is not homogeneously intermixed. In order to appreciate the difference in the spectra of fully intermixed alloys and the MBE grown CSLs, the best example comes from the annealing experiments presented in Figure 4.10. Indeed, only after 30 min of annealing at 400°C did the CSL 3/1 turn into a homogeneous alloy, as evidenced by the sole presence of regularly spaced GST 124 Bragg reflections. All the Sb_2Te_3 reflections and superlattice satellite peaks vanished. This experiment also demonstrates that full intermixing is also not likely to occur at the growth temperature of only 250°C. The co-existence of Sb_2Te_3 and GST compounds in the CSL was then further demonstrated by the Raman spectrum acquired on the CSL 3/1 (Figure 4.5), where the Sb_2Te_3 vibrational modes are unmistakably identified. By cross-checking between these three characterization techniques, it is clear that the structure resolved by STEM indeed corresponds to the CSL as grown.

Because of the proven presence of Sb_2Te_3 QLs in the CSL, intermixing has to be ruled out as the only explanation to the changing lattice spacing. Certainly, intermixing is occurring at the interfaces, and could contribute to the specific shape of the measured oscillations, especially every time the deposition is switched from one material to the other. However, intermixing cannot explain why the in-plane lattice spacing measured by RHEED never recovers to the value of relaxed Sb_2Te_3, even in the CSL 6/1 and 6/3 cases (Figure 4.17) where 6 nm of the material is deposited, ensuring that the whole surface should be covered, regardless of roughness or defects. And in the GID measurements as well (Figure 4.18), no features can be assigned to fully relaxed Sb_2Te_3. If those persisting Sb_2Te_3 QLs are in fact present in the final structure, something else is preventing them from adopting their relaxed lattice parameter.

This brings us to a second possible explanation for the observed phenomenon: Despite being considered as a stack of 2D materials, the different sublayers in the CSL could be partially coupled and strained, similarly to the coupling in the freestanding 3D heterostructures described above. However, in contrast to the ideal 3D case, this coupling

has to be only partial, because the predicted decay in the amplitude of the lattice spacing variation with increasing film thickness is not observed. The relatively weaker coupling can be understood from the fact that it would be occurring across the weaker vdW bonds.

In order to investigate the possible existence of strain and this partial coupling in CSLs, F. Lange[†] and M. Wuttig.[†] conceptualized and created a model considering the atomic layers in the system as a ensemble of balancing springs setup in parallel, each of them having their own relaxed length $a_{Mat.A/Mat.B}$ and spring constant $k_{Mat.A/Mat.B}$. This model is illustrated in Figure 4.19. In the purely 2D case, depicted in the left-hand side schematic, the materials within the blocks are rigidly coupled in the z-direction, but uncorrelated in-between them. Each spring simply adopts its own relaxed length. In contrast, for a purely 3D model, all springs are rigidly coupled also across the different materials, they would all be compressed or stretched toward a common equilibrium length. Within the limits of the elastic domain, the sum of the forces $F_{Tot}(x,d)$, with d the total thickness, is computed by integrating all forces generated in every sublayer of material A or B (Equations 4.1 and 4.2).

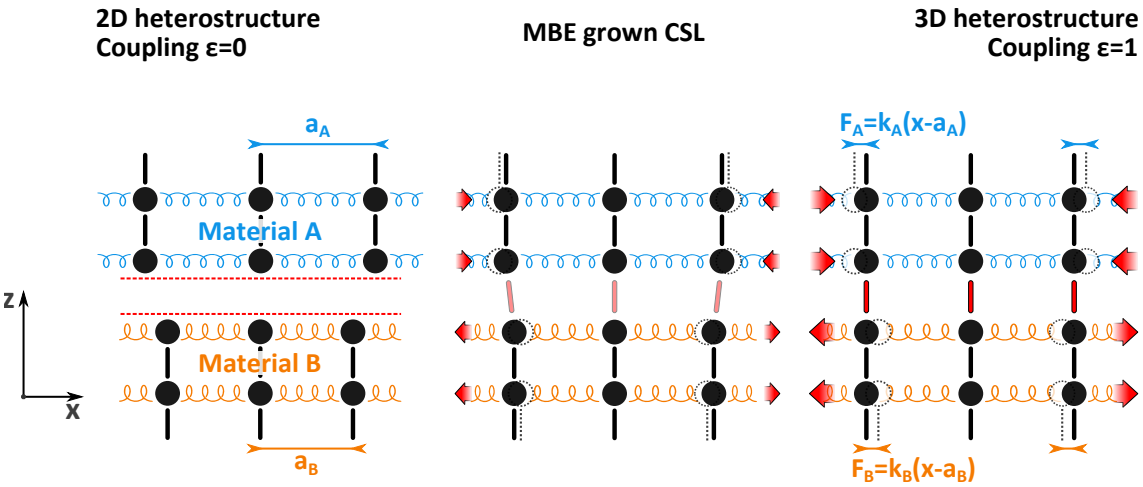

Figure 4.19: Schematic representation of the balancing springs model elaborated by F. Lange and M. Wuttig from the Physikalisches Institut in Aachen.

$$F_{Mat.A/Mat.B}(x) = k_{Mat.A/Mat.B}(x - a_{Mat.A/Mat.B}) \tag{4.1}$$

$$F_{Tot}(x,d) = \int_0^d \left(\underbrace{\rho_{Mat.A} \cdot F_{Mat.A}(x) \cdot \Omega_{Mat.A}(z) + \rho_{Mat.B} \cdot F_{Mat.B}(x) \cdot \Omega_{Mat.B}(z)}_{F^*(x,z)} \right) dz \tag{4.2}$$

[†]I. Physikalisches Institut (IA), RWTH Aachen University, Aachen, Germany

In this expression, ρ is the spring density, and $\Omega(z)$ is the crystal shape function that is composed of a series of unit step functions to describe how the materials are stacked. For our purpose, because GeTe and Sb_2Te_3 exhibit similar plane spacings in z-direction, ρ is assumed to be the same for both materials and is set to unity in the following simulations. Equilibrium is reached when $F_{Tot} = 0$, and the corresponding equilibrium lattice constant $\bar{x}(d)$ can be calculated and plotted as a function of grown CSL thickness d. Thus, the curve in the right-hand side panel of Figure 4.16 is obtained. The dampening of the variations occurs, exactly as expected from the above-mentioned Gedankenexperiment.

Now, in order to prevent this dampening from occurring in the model, and to fit the curves obtained by RHEED during CSL growth, an additional factor ϵ with values between zero and unity needs to be introduced into the equation, representing the partial strength of the coupling at the vdW gaps. In an intuitive way, the extreme cases where $\epsilon = 0$ or 1 correspond to the ideal 2D and 3D cases respectively. The way this additional factor is implemented is shown in the following expression 4.3:

$$F_{Tot}(x,d) = \int_{z(N)}^{d} F^*(x,z)dz + \sum_{i=1}^{N} \epsilon^{N-i+1} \int_{z(i-1)}^{z(i)} F^*(x,z)dz \tag{4.3}$$

With this computation, where N represents the number of blocks separated by vdW gaps, and z(i) denotes the position of these vdW gaps. The surface layer is computed with full coupling strength, but the contribution of the adjacent block below is reduced to a fraction ϵ, and the bulk layers further below contribute only by a factor of ϵ^{N-i+1}. In other words, the contribution of buried blocks become decreasingly relevant as the loss in coupling scales with each vdW gap. With this periodic loss in coupling, the oscillatory behavior of the experimentally obtained RHEED data can by reproduced very faithfully, as shown in Figure 4.20 for all four experimental sets of data, using a single set of consistent values for k, ϵ, and reference values for a.

To summarize this last part, the measured variations of in-plane lattice spacing obtained by RHEED were successfully reproduced by considering a model with blocks of elastically strained springs coupled between them. These results corroborate the hypothesis that the materials in the CSL could be strained, despite the initial assumption that they were 2D materials. This explanation aligns well with the bimodal RHEED data merging into the unimodal GID data; showing that the top layer being deposited has to find new compromises with the subsequent layers as the growth proceeds.

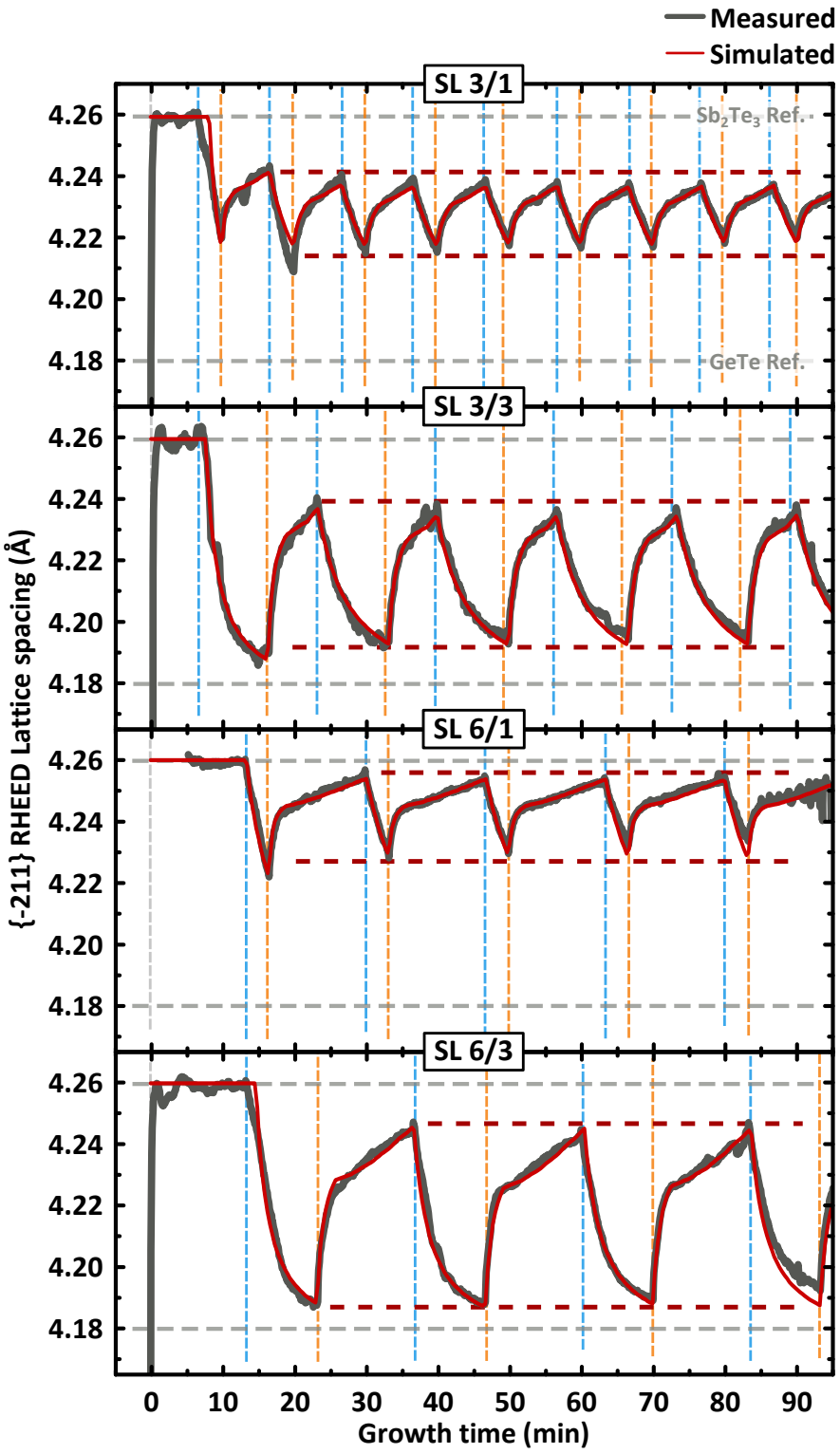

Figure 4.20: Experimental RHEED streak spacing oscillations presented in Figure 4.17 compared with simulated curves using the balanced spring model of F. Lange and M. Wuttig from the Physikalisches Institut in Aachen

The argument that the coupling needs to be only partial stemmed from the lack of dampening in the lattice spacing variations as the thickness of the grown heterostructure increases. In the spring model, dampening could be suppressed only by introducing an additional factor to simulate the loss of coupling. Looking more in detail at each of the four experimental sets of data in Figure 4.17, a very slight dampening can actually be observed over the whole growth experiment. However, this dampening does not follow the envelope of a power function, as predicted for a purely 3D case. Instead it could be attributed to an increase of the surface temperature during growth, and a resulting decrease of the growth rate. As the sublayers are getting thinner, the variation in lattice spacing also get smaller. In addition, a thinner GeTe sublayer intermixing with virtually always the same uppermost Sb_2Te_3 QL also yields GST compounds with a composition slightly richer in Sb.

In the GID data, the weakness of the coupling could be at the origin of the broadness in the CSL reflections that are measured: Instead of an entire structure strictly constrained to the same lattice parameter, as it could be expected in the ideal 3D case, the sublayers in the CSL are more loosely coupled, leading to more dispersion. Furthermore, the FWHM of these reflections is shown to increase with thicker sublayers, more specifically with increasing numbers of Sb_2Te_3 QLs. This can be understood from the fact that vdW gaps are mainly created during the deposition of Sb_2Te_3, and it is at these vdW gaps that this weak coupling is occuring. The deposition of thicker GeTe sublayers does not generate additional vdW gaps, but it changes the composition of the GST formed at the interface toward a Ge rich compound, increasing the mismatch with pure Sb_2Te_3.

The dispersion in the lattice spacing also implies that strain profile is not homogeneously distributed in the structure; according to our model, the Sb_2Te_3 QLs in direct contact with GST blocks are more strained than QLs in the middle of the sublayer. For optoelectronic applications, such dispersion would be undesirable because it would induce local variations in the electronic band structure. Instead, for thermoelectric properties, dispersion could provide advantageous phonon scattering sites. From this point of view, CSLs could have enhanced thermoelectric properties compared to their Sb_2Te_3 or GST counterparts. Because the strain status is only decided locally among neighboring layers, these properties could even be further enhanced by purposefully growing CSLs with highly irregular stacking sequences, thus engineering more dispersion, and further amplifying the anisotropy between the out of plane and in-plane properties.[124]

In the GID data, shifts in the CSL($\bar{4}22$) reflection were observed depending on the stacking sequence. In the RHEED data as well, the average value around which the lattice spacing oscillates differs in each sample. Indeed, the equilibrium lattice spacing is not

intrinsic to the pair of materials, or dictated by the substrate as in the pseudomorphic cases, but dependent on the thickness of the deposited sublayers. This means that the shared lattice spacing can be tuned, an the resulting strain can be engineered. In fact it is very interesting to compare the equilibrium lattice spacing with the relaxed lattice parameters in GST compounds of different compositions. The experimentally measured in-plane lattice parameters in GeTe, Sb_2Te_3, $Ge_2Sb_2Te_5$, and $Ge_3Sb_2Te_6$ are reported[118] (black squares) in Figure 4.21. Each compound is listed on the X-axis by the Ge concentration in its anionic sublattice ($Ge/Ge+Sb$). As one could have anticipated, there is a linear dependence between the composition and the in-plane lattice parameter in these compounds on the pseudo-binary line, as highlighted by the grey dashed line. If the same Ge concentration is quantified in the four CSLs investigated here and plotted on this graph, a striking consistency with the lattice spacing in GST alloys is observed.

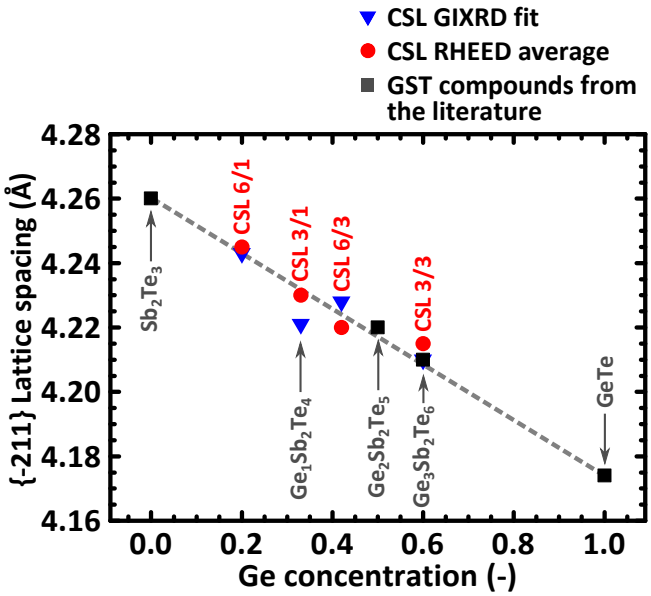

Figure 4.21: Average lattice spacing measured by RHEED (red circles), and lattice spacing obtained by GID (blue triangles) for the four superlattices presented in Figures 4.17 and 4.18. Experimental reference values for GeTe, Sb_2Te_3, $Ge_2Sb_2Te_5$, and $Ge_3Sb_2Te_6$ are shown (grey squares). The values found in CSLs matches with the expected value of a homogeneous GST alloy of the same average composition.

This linear relationship could be used as a very straightforward method to predict the resulting average state of strain in a given CSL: One only needs to consider the overall composition in the CSL, were it completely intermixed into a homogeneous alloy. In the CSL 3/1 case for example, the structure in this specific superlattice has been resolved as

being best represented by blocks of Sb_2Te_3 and $Ge_3Sb_2Te_6$. However, all compounds in the stacking adopt a common lattice spacing converging toward the expected value for $Ge_1Sb_2Te_4$, the overall composition considering the entire SL.

For strain engineering purposes, it would be most interesting to fabricate a 3D heterostructure that is free-standing on the substrate, as considered in our Gedankenexperiment. Also in this case, strain could be tuned simply by changing the thickness of the compounds. The resulting strain could even be more consequent, owing to the stronger coupling between the layers. However, the whole structure will adopt one common lattice spacing, whereas strain could potentially be modulated locally along the growth direction by growing a CSL with a non periodic stacking sequence.

Finally, the question of the origin for this coupling in CSLs is raised. One point to keep in mind is that vdW bonds are often neglected because of the large contrast in strength compared to covalent bonds. But phase change materials are resonantly bonded; although they are considered covalent in their principle of shared electrons, they are still much weaker compared to hybridized covalent bonds. Therefore, the contrast in strength between vdW and resonant bonds is less pronounced than compared with hybridized bonds. The assumption that the vdW bonds are relatively negligible may simply not be true in this case.

One other possible factor inducing coupling could be the presence of defects, such as the discontinued vdW gaps observed by TEM, as shown in Figure 4.6. Indeed, because of the weakness of vdW bonds, any dangling bonds could help to pin the blocks together. However, it seems unlikely for defects to be the only factor responsible for the coupling, because the density of defects is expected to increase as the surface roughness increases with more CSL repetitions. But all four CSLs RHEED datasets could be fitted using the spring model with one single constant value of ϵ. So the strength of the coupling does not seem to differ throughout one experiment, and also remains consistent between different growths. In order to better understand the role of defects in these vdW heterostructures, the growth of CSLs with very precise control of each sublayer thickness could offer further insights. By ensuring that each molecular layer is fully covering, the density of defects can be greatly reduced, and a more drastic loss of coupling between the layers could be expected.

4.3 Summary and conclusion

In this chapter, the successful growth of Sb_2Te_3/GeTe superlattices has been demonstrated. To be mentioned in particular, the growth on the Sb passivated $Si(111) - (\sqrt{3} \times \sqrt{3})R30° -$ Sb surface ensures the whole CSL is textured with one single out-of-plane and in-plane orientation (plus its twinned domain).

Revealed by XRD and Raman, then demonstrated by STEM, intermixing is observed between the GeTe and the topmost Sb_2Te_3 QL of each sublayer, forming different GST compounds at the interface. Using the ability of the STEM HAADF mode to discriminate between heavy and lighter atomic species, an asymmetry in the Ge concentration inside the GST blocks is discovered. Mainly from this observation, a growth model is drafted, attributing the intermixing specifically to the deposition of GeTe on top of Sb_2Te_3.

Precise analysis of RHEED data acquired during CSL growth uncovered an oscillating in-plane lattice spacing incompatible with neither the theoretical 2D case, nor the 3D case. CSLs seem to fall in-between these two cases. As corroborated by GID measurements acquired after growth, the CSL sublayers could be strained toward one common lattice spacing. In contrast with pseudomorphic 3D heterostructures, the amplitude of this strain is not intrinsic to the pair of materials, but is dependent on the thickness of the sublayers. This implies that the strain can be engineered locally in the CSL simply by growing different stacking sequences. It is shown that a certain degree of coupling can exist across vdW gaps. The possibility for induced strain should be acknowledged for the design of 2D heterostructures, they cannot simply be assumed to be fully relaxed because of their 2D nature.

Conclusion and outlook

Beyond phase change materials, this thesis exemplifies how different characterization methods can be used in concert, complementing and corroborating each other. While RHEED surveys the state of the surface, XRD is necessary to access the crystalline structures below. Inversely, an ultra-thin layer can be characterized by RHEED, whereas it would be invisible to XRD because of its lack of periodicity in the out-of-plane direction. Similarely, amorphous matter does not give rise to any features in XRD, and Raman spectroscopy is needed instead. XRD is also an averaging technique, and TEM is necessary to understand how the local structure changes along the thickness of the film. Limitations regarding XRR have also been highlighted when the density contrast between different phases is insufficient.

To list the main achievements accomplished in this thesis, the epitaxial growth of GeTe and GeTe/Sb_2Te_3 CSL films is demonstrated on three different Si(111) surfaces reconstructions. Through this comparative study, the importance of surface treatments is evidenced. More specifically, the distinction between passivated and non-passivated surfaces is clearly shown. In the case of GeTe, in-plane twisted and twinned domains could be suppressed by growing on a passivated surface. These new thin-films boasting superior crystalline quality turned out to be highly suitable platforms for the study of the giant-Rashba spin splitting in GeTe, and its coupling to the ferroelectric properties of the material.[29,125]

Mainly evidenced by RHEED, abnormal phenomena were observed close to the beginning of the deposition: On the $\mathrm{Si}(111)-(7\times7)$ and $\mathrm{Si}(111)-(1\times1)-\mathrm{H}$ reconstructions, growth is initiated by the accumulation of an amorphous layer, although the chosen growth parameters should clearly yield a crystalline film. In contrast, on the $\mathrm{Si}(111)-(\sqrt{3}\times\sqrt{3})R30°-\mathrm{Sb}$ surface, a crystalline film is formed immediately at growth onset, but a larger than expected in-plane lattice spacing is measured during the very first few atomic layers. These phenomena were explained by the destabilization of the structure

expected in the bulk, under the influence of the interface. Resonant bonding and Peierls distortion, the fundamental actors deciding the structure of GeTe, could not be normally expressed in an ultra-thin film.

Improvements brought by the passivated surfaces into the crystalline quality of GeTe and Sb_2Te_3 directly translated into an improvement of the CSL structure with both materials stacked on top of each other. Indeed, the epitaxial registry of the whole structure is decided already by the very first sublayer. Therefore, when the formation of in-plane twisted domains are eliminated from the very first layer, they are prevented in the whole superlattice structure above as well. Attention is drawn to the intermixing occurring at the interfaces of CSLs grown by MBE. Based on HAADF-STEM imaging, a model is proposed to describe exactly how this intermixing is occuring. For their modeling and understanding, these MBE grown CSLs should be considered as a stack of Sb_2Te_3 and ordered GST alloy; two different 2D laminar materials.

Despite the intermixing, occuring *a contrario* from models that suggest a clear interface between GeTe and Sb_2Te_3,[10,126] state of the art switching performances were achieved in MBE grown CSL memory cells: After the growth parameters were optimized on silicon, as described in this thesis, the growth recipe was adapted by J. Boschker,[†] and grown in test vehicles engineered in collaboration with Micron Microelectronics.[8] In Figure 4.22, the programming current is plotted versus the SET resistance in GST and CSL cells of the same geometry.[127] As a rule of thumb, in such plots, the closer the data points are from the origin, the less energy is needed to switch the material. Figure 4.22 clearly shows an improvement going from GST to CSL. The performances of MBE grown CSLs are on par with, or better, than the ones of state of the art CSL cells, labeled as AIST (blue star) and LEAP (red star).[10,126] In fact, even the homogeneous GST alloy cells grown by MBE (lila dots) boast very decent performances, in line with the 200 mm production line of Micron in Agrate.[8]

It would now be very interesting to further investigate how exactly these improvements are achieved in the CSL, and what role the vdW interfaces play in the switching. The exact thickness of the sublayers could also play an important role, in analogy to the case of MBE grown $GaAs/Al_{0.25}Ga_{0.75}$ heterostructures for quantum cascade laser applications,[128] where the functionality of the device relies entirely on the control of the quantum well thicknesses. Since HAADF-STEM has proved to be a technique capable of discriminating atomic species in these MBE grown CSLs, it would be of great interest to investigate pieces of the same sample before and after switching, to really understand

[†]Paul-Drude-Institut, Berlin, Germany

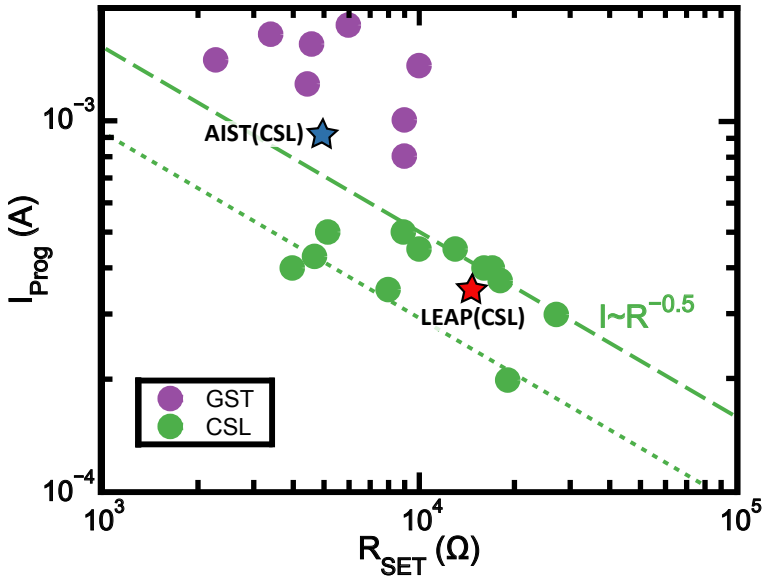

Figure 4.22: RESET programming current as a function of SET resistance for GST and CSL based devices (Device fabrication and characterization performed by J. Boschker from the Paul-Drude-Institut using test vehicles engineered by Micron Microelectronics). Best results from the literature from AIST [10] and LEAP [126] groups are reported with blue and red stars.

how the structure is transformed. If the contrast in optical and electrical properties between the crystalline and amorphous phase in PCMs is owed to the transition from resonant to hybridized bonds, a similarly drastic change in the bonding mechanism should be expected between the SET/RESET states in the CSL.

Knowing that intermixing is likely to occur during MBE growth of GeTe on Sb_2Te_3, it may be worthwhile to directly grow and investigate GST/Sb_2Te_3 CSL structures. In this way, it may be possible to prevent the assymetrical concentration of Ge within the GST blocks (Figure 4.8). Regarding intermixing, it could be interesting to investigate epitaxy of GeTe or GST on a fully covering Sb_2Te_3 layer, versus growth upon a partially covering layer. For this purpose, it may be necessary to monitor the growth rate very precisely, using an in-line QMS to dynamically adjust the substrate temperature and keep the desorption rate constant. The growth also needs to be further optimized to ensure that deposition follows closely a layer-by-layer Frank van der Merwe growth process; the simultaneous nucleation and coalescence of multiple layers would be detrimental to such an experiment.

Intermixing in the CSL could also be exploited as a fabrication method for epitaxial hexagonal GST films. TEM imaging and XRD characterization have shown that a very high quality hexagonal GST 124 film was obtained after annealing the CSL 3/1 at 350°C for 30min (Figure 4.10). It would be interesting to anneal other CSLs with average com-

position GST 326 and GST 225, to understand whether GST 124 is simply the most stable composition, or if the superlattice would intermix toward its average composition. The latter case would be very interesting: While the control of the composition is difficult during the growth of the ternary compound by MBE, it could be easier to grow the two stoichiometric binary compounds with well controlled thicknesses, and then anneal in order to obtain the hexagonal GST with the desired composition.

As discussed in the last chapter, variations are observed by monitoring the in-plane lattice spacing at the top-most surface of the growing film by RHEED. These changes could neither be attributed to a fully decoupled case of 2D vdW epitaxy nor to a typical case of 3D classical epitaxy. The hybrid behavior seemed to be situated somewhere in-between instead; a certain degree of coupling is observed, even across the vdW bonds. Moreover, the resulting strain can be modulated simply by changing the thickness of the different sublayers. This strongly contrasts with 3D heterostructures and pseudomorphic growth, where the strain in the film is rigidly fixed by the lattice of the substrate. A new degree of freedom for strain engineering is thus enabled in 2D heterostructures. Following this path, the next step is clearly to engineer strained 2D heterostructures and measure the effect of strain on specific properties of the material. For instance, thermoelectric properties could be interesting to investigate, since GST and Sb_2Te_3 both show improved thermoelectric figure of merit Z, owing to their resonantly bonded network and 2D lamellar structure.[42,43] And these thermoelectric properties are known to be further influenced by strain in such materials.[129,130] Phase-change properties have been demonstrated to be strain-dependent as well.[131,132]

Appendix

List of MBE samples prepared

In the table below, all MBE growths were I actively participated are listed in a loose chronological order. All the first calibration samples up to the first Sb_2Te_3/GeTe superlattice tests were performed with the help of Dr. Alessandro Giussani and Dr. Karthick Perumal. Overnight experiments were conducted with either Dr. Raffaella Calarco or Dr. Stefano Checci. We also often helped each other with our various tasks with Dr. Jos Boschker and Valeria Bragaglia.

Sample ID	Description	# of samples
s2_0612 - s2_0648	PHARAO II Individual cell calibration and sputtering unit calibration. While sputtering, Ge and Sb cell worked properly, the tip of the Te cell was incorrectly mounted, resulting in the cell getting obstructed. System needed to be opened to repair the cell. It could then be correctly calibrated.	37
s2_0649 - s2_0660	First GeTe and GST growth on Si. Growth parameters previously used by Alessandro Giussani and Karthick Perumal could be used. By adjusting substrate temperature, growth could be performed on silicon membranes for ex-situ measurements in transmission at the BESSY II beamline	12
s2_0662, s2_0663, s2_0668	First Sb_2Te_3/GeTe superlattice tests	3
s2_0667, s2_0671, s2_0677 - s2_0679	GeTe growth optimisation and sample for ARPES experiments by Prof. Bertacco	5
s2_0682, s2_0687 - s2_0692, s2_0790	More superlattice growth and characterization, optimization of GeTe and Sb_2Te_3 for superlattice growth	8

s2_0698, s2_0701, s2_0703	First GeTe samples on the Sb passivated silicon, optimized sample sent to Prof. Bertacco.	3
s2_0695, s2_0709, s2_0717, s2_0728, s2_0730, s2_0732, s2_0734	Growth and characterization of superlattices with inverted stacking, starting with Ge. Sublayer growth rate calculation by changing the deposition time of GeTe only.	7
s2_0720, s2_0721, s2_0741, s2_0742, s2_0748, s2_0759	More GeTe growth optimization, and more GeTe samples sent to Prof. Bertacco.	6
s2_0743, s2_0747	Super thin GeTe film growth and characterization	2
s2_0761, s2_0762, s2_0765, s2_0767 - s2_0769	GeTe series with Ge predeposition	6
s2_0773, s2_0775, s2_0778	GeTe with low substrate T; best sample was sent to Prof. Bertacco, to be used for another ARPES beamtime	3
s2_0782, s2_0783, s2_0793, s2_0810	GeTe samples for RHEED study	4
s2_0788, s2_0789	GeTe and GST samples for BESSY II beamtime	2
s2_0825 - s2_0830, s2_0840, s2_0894, s2_0895, s2_0914	GeTe growth onset study on the Sb passivated Si. A number of these growths were done overnight for best RHEED stability.	9
s2_0850 - s2_0853	MBE system maintenance, Te cell refilling and calibration	4
s2_0855, s2_0856, s2_0859, s2_0862, s2_0866, s2_0868	Serie of superlattices with growth interruptions under Te flux after each sublayer	6
s2_0896, s2_0898, s2_0900, s2_0903, s2_0905, s2_0913	More GeTe samples for Prof. Bertacco	6
s2_0897, s2_0906, s2_0956 - s2_0958, s2_0961	GeTe on H passivated Si, and overnight growth onset RHEED study.	6
s2_0986 - s2_0991, s2_0993	Overnight RHEED study during superlattice growth	7
s2_0811, s2_0927, s2_0937, s2_1003	GST or GeTe growth on special Omicron sample holder for transfer by vaccum shuttle to BESSY II	4

Total count	**140**

Bibliography

[1] W. Wełnic, S. Botti, L. Reining, and M. Wuttig, "**Origin of the optical contrast in phase-change materials**," *Physical review letters*, vol. 98, pp. 236403 1–4, jun 2007.

[2] K. Shportko, S. Kremers, M. Woda, D. Lencer, J. Robertson, and M. Wuttig, "**Resonant bonding in crystalline phase-change materials**," *Nature materials*, vol. 7, pp. 653–8, aug 2008.

[3] S. Raoux, W. Wełnic, and D. Ielmini, "**Phase change materials and their application to nonvolatile memories**," *Chemical reviews*, vol. 110, pp. 240–267, jan 2010.

[4] S.K.Bahl and K.L.Chopra, "**Amorphous versus Crystalline GeTe Films. III. Electrical Properties and Band Structure**," *Journal of Applied Physics*, vol. 41, no. 5, pp. 2196–2212, 1970.

[5] S. Raoux, "**Phase Change Materials**," *Annual Review of Materials Research*, vol. 39, pp. 25–48, aug 2009.

[6] H.-S. P. Wong, S. Raoux, S. Kim, J. Liang, J. P. Reifenberg, B. Rajendran, M. Asheghi, and K. E. Goodson, "**Phase Change Memory**," *Proceedings of the IEEE*, vol. 98, pp. 2201–2227, dec 2010.

[7] M. Wuttig and N. Yamada, "**Phase-change materials for rewriteable data storage**," *Nature Materials*, vol. 6, pp. 824–832, nov 2007.

[8] J. E. Boschker, M. Boniardi, A. Redaelli, H. Riechert, and R. Calarco, "**Electrical performance of phase change memory cells with $Ge_3Sb_2Te_6$ deposited by molecular beam epitaxy**," *Applied Physics Letters*, vol. 106, p. 023117, jan 2015.

[9] D. Loke, T. Lee, W. Wang, L. Shi, R. Zhao, Y. Yeo, T. Chong, and S. Elliott, "**Breaking the speed limits of phase-change memory**," *Science*, vol. 336, p. 1566, jun 2012.

[10] R. E. Simpson, P. Fons, A. Kolobov, T. Fukaya, M. Krbal, T. Yagi, and J. Tominaga, "**Interfacial phase-change memory**," *Nature nanotechnology*, vol. 6, pp. 501–505, aug 2011.

[11] T. Chong, L. Shi, X. Wei, R. Zhao, H. Lee, P. Yang, and A. Du, "**Crystalline Amorphous Semiconductor Superlattice**," *Physical Review Letters*, vol. 100, pp. 4–7, mar 2008.

[12] C. Pauly, M. Liebmann, A. Giussani, J. Kellner, S. Just, J. Sanchez-Barriga, E. Rienks, O. Rader, R. Calarco, G. Bihlmayer, and M. Morgenstern, "**Evidence for topological band inversion of the phase change material $Ge_2Sb_2Te_5$**," *Applied Physics Letters*, vol. 103, no. 24, p. 243109, 2013.

[13] H. Zhang, C.-X. Liu, X.-L. Qi, X. Dai, Z. Fang, and S.-C. Zhang, "**Topological insulators in Bi_2Se_3, Bi_2Te_3 and Sb_2Te_3 with a single Dirac cone on the surface**," *Nature Physics*, vol. 5, pp. 438–442, may 2009.

[14] D. Wu, L. D. Zhao, S. Hao, Q. Jiang, F. Zheng, J. W. Doak, H. Wu, H. Chi, Y. Gelbstein, C. Uher, C. Wolverton, M. Kanatzidis, and J. He, "**Origin of the high performance in GeTe-based thermoelectric materials upon Bi_2Te_3 doping**," *Journal of the American Chemical Society*, vol. 136, pp. 11412–11419, 2014.

[15] D.-S. Suh, C. Kim, K. H. P. Kim, Y.-S. Kang, T.-Y. Lee, Y. Khang, T. S. Park, Y.-G. Yoon, J. Im, and J. Ihm, "**Thermoelectric heating of $Ge_2Sb_2Te_5$ in phase change memory devices**," *Applied Physics Letters*, vol. 96, no. 12, p. 123115, 2010.

[16] M. Krbal, a. V. Kolobov, P. Fons, K. V. Mitrofanov, Y. Tamenori, J. Hegedus, S. R. Elliott, and J. Tominaga, "**Selective detection of tetrahedral units in amorphous GeTe-based phase change alloys using Ge L3-edge x-ray absorption near-edge structure spectroscopy**," *Applied Physics Letters*, vol. 102, no. 11, p. 111904, 2013.

[17] N. Mott and E. Davis, **Electronic Processes in Non-Crystalline Materials** *(Oxford Classic Texts in the Physical Sciences)*. Oxford University Press, 2 edition ed., 2012.

[18] D. Lencer, M. Salinga, and M. Wuttig, "**Design rules for phase-change materials in data storage applications**," *Advanced materials (Deerfield Beach, Fla.)*, vol. 23, pp. 2030–58, may 2011.

[19] D. Lencer, M. Salinga, B. Grabowski, T. Hickel, J. Neugebauer, and M. Wuttig, "**A map for phase-change materials**," *Nature materials*, vol. 7, pp. 972–7, dec 2008.

[20] P. B. Littlewood, "**The crystal structure of IV-VI compounds. I. Classification and description**," *Journal of Physics C: Solid State Physics*, vol. 13, no. 26, p. 4855, 1980.

[21] J. P. Gaspard, A. Pellegatti, F. Marinelli, and C. Bichara, "**Peierls instabilities in covalent structures I. Electronic structure, cohesion and the $Z = 8 - N$ rule**," *Philosophical Magazine Part B*, vol. 77, pp. 727–744, mar 1998.

[22] B. Huang and J. Robertson, "**Bonding origin of optical contrast in phase-change memory materials**," *Physical Review B*, vol. 81, pp. 1–4, feb 2010.

[23] T. Nonaka, G. Ohbayashi, Y. Toriumi, Y. Mori, and H. Hashimoto, "**Crystal structure of GeTe and $Ge_2Sb_2Te_5$ meta-stable phase**," *Thin Solid Films*, vol. 370, pp. 258–261, jul 2000.

[24] V. L. Deringer, M. Lumeij, and R. Dronskowski, "**Ab Initio Modeling of α-GeTe(111) Surfaces**," *The Journal of Physical Chemistry C*, vol. 116, pp. 15801–15811, jul 2012.

[25] J. J. Gervacio-Arciniega, E. Prokhorov, F. J. Espinoza-Beltran, and G. Trapaga, "**Characterization of local piezoelectric behavior of ferroelectric GeTe and $Ge_2Sb_2Te_5$ thin films**," *Journal of Applied Physics*, vol. 112, no. 5, p. 052018, 2012.

[26] A. V. Kolobov, D. J. Kim, A. Giussani, P. Fons, J. Tominaga, R. Calarco, and A. Gruverman, "**Ferroelectric switching in epitaxial GeTe films**," *APL Materials*, vol. 2, p. 066101, jun 2014.

[27] F. Kadlec, C. Kadlec, P. Kužel, and J. Petzelt, "**Study of the ferroelectric phase transition in germanium telluride using time-domain terahertz spectroscopy**," *Physical Review B*, vol. 205209, pp. 1–8, 2011.

[28] M. J. Polking, J. J. Urban, D. J. Milliron, H. Zheng, E. Chan, M. a. Caldwell, S. Raoux, C. F. Kisielowski, J. W. Ager, R. Ramesh, and A. P. Alivisatos, "**Size-Dependent Polar Ordering in Colloidal GeTe Nanocrystals**," *Nano Letters*, vol. 11, pp. 1147–1152, mar 2011.

[29] M. Liebmann, C. Rinaldi, D. Di Sante, J. Kellner, C. Pauly, R. N. Wang, J. E. Boschker, A. Giussani, S. Bertoli, M. Cantoni, L. Baldrati, M. Asa, I. Vobornik, G. Panaccione, D. Marchenko, J. Sánchez-Barriga, O. Rader, R. Calarco, S. Picozzi, R. Bertacco, and M. Morgenstern, "**Giant Rashba-Type Spin Splitting in Ferroelectric GeTe(111)**," *Advanced Materials*, vol. 28, pp. 560–565, jan 2016.

[30] D. Di Sante, P. Barone, R. Bertacco, and S. Picozzi, "**Electric control of the giant Rashba effect in bulk GeTe**," *Advanced materials (Deerfield Beach, Fla.)*, vol. 25, pp. 509–13, jan 2013.

[31] S. Picozzi, "**Ferroelectric Rashba semiconductors as a novel class of multifunctional materials**," *Frontiers in Physics*, vol. 2, no. February, pp. 1–5, 2014.

[32] P. Fons, A. V. Kolobov, M. Krbal, J. Tominaga, K. Andrikopoulos, S. Yannopoulos, G. Voyiatzis, and T. Uruga, "**Phase transition in crystalline GeTe: Pitfalls of averaging effects**," *Physical Review B*, vol. 82, pp. 2–6, oct 2010.

[33] T. Siegrist, P. Jost, H. Volker, M. Woda, P. Merkelbach, C. Schlockermann, and M. Wuttig, "**Disorder-induced localization in crystalline phase-change materials**," *Nature Materials*, vol. 10, pp. 202–208, mar 2011.

[34] H. Przybylińska, G. Springholz, R. Lechner, M. Hassan, M. Wegscheider, W. Jantsch, and G. Bauer, "**Magnetic-Field-Induced Ferroelectric Polarization Reversal in the Multiferroic $Ge_{1-x}Mn_xTe$ Semiconductor**," *Physical Review Letters*, vol. 112, p. 047202, jan 2014.

[35] R. Wang, J. E. Boschker, E. Bruyer, D. D. Sante, S. Picozzi, K. Perumal, A. Giussani, H. Riechert, and R. Calarco, "**Toward Truly Single Crystalline GeTe Films: The Relevance of the Substrate Surface**," *The Journal of Physical Chemistry C*, vol. 118, pp. 29724–29730, dec 2014.

[36] A. V. Kolobov, J. Tominaga, P. Fons, and T. Uruga, "**Local structure of crystallized GeTe films**," *Applied Physics Letters*, vol. 82, no. 3, p. 382, 2003.

[37] A. Edwards, A. Pineda, P. Schultz, M. Martin, A. Thompson, H. Hjalmarson, and C. Umrigar, "**Electronic structure of intrinsic defects in crystalline germanium telluride**," *Physical Review B*, vol. 73, jan 2006.

[38] V. L. Deringer, M. Lumeij, R. P. Stoffel, and R. Dronskowski, "**Mechanisms of Atomic Motion Through Crystalline GeTe**," *Chemistry of Materials*, vol. 25, pp. 2220–2226, jun 2013.

[39] W. Zhang, A. Thiess, P. Zalden, R. Zeller, P. H. Dederichs, J.-Y. Raty, M. Wuttig, S. Blügel, and R. Mazzarello, "**Role of vacancies in metal-insulator transitions of crystalline phase-change materials**," *Nature materials*, vol. 11, pp. 952–6, nov 2012.

[40] J. H. Oh, S. W. Ryu, B. J. Choi, S. Y. Hwang, and Y. J. Kim, "**Phase Transition Characteristics of Nitrogen-Doped Antimony-Telluride ($N-$$Sb_2Te_3$) Thin Films for a Phase Change Random Access Memory**," *Journal of the Korean Physical Society*, vol. 49, no. 3, 2006.

[41] M. Wuttig, D. Lüsebrink, D. Wamwangi, W. Wełnic, M. Gillessen, and R. Dronskowski, "**The role of vacancies and local distortions in the design of new phase-change materials**," *Nature materials*, vol. 6, pp. 122–8, feb 2007.

[42] M. N. Touzelbaev, P. Zhou, R. Venkatasubramanian, and K. E. Goodson, "**Thermal characterization of Bi_2Te_3/Sb_2Te_3 superlattices**," *Journal of Applied Physics*, vol. 90, no. 2, pp. 763–767, 2001.

[43] S. Lee, K. Esfarjani, T. Luo, J. Zhou, Z. Tian, and G. Chen, "**Resonant bonding leads to low lattice thermal conductivity**," *Nature Communications*, vol. 5, pp. 1–8, 2014.

[44] T. C. Chong, L. P. Shi, X. S. Miao, P. K. Tan, R. Zhao, and Z. P. Cai, "**Study of the Superlattice-Like Phase Change Optical Recording Disks**," *Japanese Journal of Applied Physics*, vol. 39, pp. 737–740, feb 2000.

[45] Y. Cao and W. Qiang, "**On the properties of GeTe/Sb_2Te_3 superlattice-like structure for phase-change optical recording**," *Proc. SPIE*, vol. 6029, no. ICO20, 2006.

[46] T. C. Chong, L. P. Shi, R. Zhao, P. K. Tan, J. M. Li, H. K. Lee, X. S. Miao, a. Y. Du, and C. H. Tung, "**Phase change random access memory cell with superlattice-like structure**," *Applied Physics Letters*, vol. 88, no. 12, p. 122114, 2006.

[47] C. Kim, D. Kang, T.-Y. Lee, K.-B. K. H. P. Kim, Y.-S. Kang, J. Lee, S.-W. Nam, and Y. Khang, "**Direct evidence of phase separation in $Ge_2Sb_2Te_5$ in phase change memory devices**," *Applied Physics Letters*, vol. 94, p. 193504, 2009.

[48] T.-Y. Yang, I.-M. Park, B.-J. Kim, and Y.-C. Joo, "**Atomic migration in molten and crystalline $Ge_2Sb_2Te_5$ under high electric field**," *Applied Physics Letters*, vol. 95, no. 3, pp. 32103–32104, 2009.

[49] Y. Saito, J. Tominaga, P. Fons, A. V. Kolobov, and T. Nakano, "**Ab-initio calculations and structural studies of $(SiTe)_2(Sb_2Te_3)_n$(n : 1, 2, 4 and 6) phase-change superlattice films**," *physica status solidi (RRL) - Rapid Research Letters*, vol. 8, pp. 302–306, apr 2014.

[50] T. Ohyanagi, M. Kitamura, M. Araidai, S. Kato, N. Takaura, and K. Shiraishi, "**GeTe sequences in superlattice phase change memories and their electrical characteristics**," *Applied Physics Letters*, vol. 104, p. 252106, jun 2014.

[51] J. Tominaga, A. V. Kolobov, P. Fons, T. Nakano, and S. Murakami, "**Ferroelectric Order Control of the Dirac-Semimetal Phase in GeTe-Sb_2Te_3 Superlattices**," *Advanced Materials Interfaces*, vol. 1, p. 1300027, feb 2014.

[52] X. Yu and J. Robertson, "**Modeling of switching mechanism in GeSbTe chalcogenide superlattices**," *Scientific Reports*, vol. 5, p. 12612, jul 2015.

[53] M. Wienold, L. Schrottke, M. Giehler, R. Hey, W. Anders, and H. T. Grahn, "**Low-threshold terahertz quantum-cascade lasers based on GaAs/$Al_{0.25}Ga_{0.75}$As heterostructures**," *Applied Physics Letters*, vol. 97, no. 7, p. 071113, 2010.

[54] M. Musolino, D. van Treeck, A. Tahraoui, L. Scarparo, C. D. Santi, M. Meneghini, E. Zanoni, L. Geelhaar, and H. Riechert, "**A physical model for the reverse leakage current in (In,Ga)N/GaN light-emitting diodes based on nanowires**," *Journal of Applied Physics*, vol. 119, no. 4, p. 044502, 2016.

[55] M. Mandl, X. Wang, T. Schimpke, C. Kölper, M. Binder, J. Ledig, A. Waag, X. Kong, A. Trampert, F. Bertram, J. Christen, F. Barbagini, E. Calleja, and M. Strassburg, "**Group III nitride core-shell nano- and microrods for optoelectronic applications**," *Physica Status Solidi - Rapid Research Letters*, vol. 7, no. 10, pp. 800–814, 2013.

[56] B. Jenichen, W. Braun, V. M. Kaganer, A. Shtukenberg, L. Däweritz, C.-G. Schulz, and K. Ploog, "**Combined molecular beam epitaxy and diffractometer system for in situ x-ray studies of crystal growth**," *Review of Scientific Instruments*, vol. 74, no. 3, pp. 1267–1273, 2003.

[57] M. Copel, M. C. Reuter, M. Horn von Hoegen, and R. M. Tromp, "**Influence of surfactants in Ge and Si epitaxy on Si(001)**," *Physical Review B*, vol. 42, pp. 11682–11689, dec 1990.

[58] E. a. Paisley, M. D. Losego, B. E. Gaddy, J. S. Tweedie, R. Collazo, Z. Sitar, D. L. Irving, and J.-P. Maria, "**Surfactant-enabled epitaxy through control of growth mode with chemical boundary conditions**," *Nature Communications*, vol. 2, p. 461, sep 2011.

[59] M. Grundmann, "**Formation of epitaxial domains: Unified theory and survey of experimental results**," *Physica Status Solidi (B)*, vol. 248, pp. 805–824, apr 2011.

[60] J. Narayan and B. C. Larson, "**Domain epitaxy: A unified paradigm for thin film growth**," *Journal of Applied Physics*, vol. 93, no. 1, p. 278, 2003.

[61] H. Zi-Pu, D. F. Ogletree, M. A. Van Hove, and G. A. Somorjai, "**Leed theory for incommensurate overlayers: Application to graphite on Pt(111)**," *Surface Science*, vol. 180, no. 2-3, pp. 433–459, 1987.

[62] G. V. Hansson, H. H. Radamsson, and W.-X. Ni, "**Strain and relaxation in Si-MBE structures studied by reciprocal space mapping using high resolution X-ray diffraction**," *Journal of Materials Science: Materials in Electronics*, vol. 6, pp. 292–297, oct 1995.

[63] I. K. Robinson, "**Crystal truncation rods and surface roughness**," *Physical Review B*, vol. 33, pp. 3830–3836, mar 1986.

[64] J. Zhang, J. Neave, B. Joyce, P. Dobson, and P. Fawcett, "**On the RHEED specular beam and its intensity oscillation during MBE growth of GaAs**," *Surface Science*, vol. 231, pp. 379–388, may 1990.

[65] R. S. S. John O'Connor, Brett Sexton, **Surface Analysis Methods in Materials Science**, Springer Science & Business Media, 2 ed., 2013.

[66] J. H. Neave, B. A. Joyce, P. J. Dobson, and N. Norton, "**Dynamics of film growth of GaAs by MBE from Rheed observations**," *Applied Physics A Solids and Surfaces*, vol. 31, pp. 1–8, may 1983.

[67] K. Yamanaka, H. Ogiso, and O. Kolosov, "**Ultrasonic force microscopy**," *App. Phys. Lett.*, vol. 64, no. 2, pp. 178–180, 1994.

[68] J. L. Bosse, I. Grishin, B. D. Huey, and O. V. Kolosov, "**Nanomechanical morphology of amorphous, transition, and crystalline domains in phase change memory thin films**," *Applied Surface Science*, vol. 314, pp. 151–157, 2014.

[69] S. Fölsch, J. Martínez-Blanco, J. Yang, K. Kanisawa, and S. C. Erwin, "**Quantum dots with single-atom precision**," *Nature nanotechnology*, vol. 9, no. 7, pp. 505–8, 2014.

[70] A. H. Al-Bayati, K. G. Orrman-Rossiter, J. van den Berg, and D. Armour, "**Composition and structure of the native Si oxide by high depth resolution medium energy ion scatering**," *Surface Science*, vol. 241, no. 1-2, pp. 91–102, 1991.

[71] H. Ubara, T. Imura, and A. Hiraki, "**Formation of Si-H bonds on the surface of microcrystalline silicon covered with SiO_x by HF treatment**," *Solid State Communications*, vol. 50, no. 7, pp. 673–675, 1984.

[72] Y. Morita, K. Miki, and H. Tokumoto, "**Atomic Structure of Hydrogen-Terminated Si (lll) Surfaces by Hydrofluoric Acid Treatments**," *Japanese journal of applied physics*, vol. 30, p. 3570, 1991.

[73] G. S. Higashi, Y. J. Chabal, G. W. Trucks, and K. Raghavachari, "**Ideal hydrogen termination of the Si(111) surface**," *Applied Physics Letters*, vol. 56, no. 7, p. 656, 1990.

[74] K. Brommer, M. Needels, and B. Larson, "**Ab Initio Theory of the Si(111)-(7×7) Surface Reconstruction**," *Physical review letters*, vol. 68, no. 9, pp. 1355–1359, 1992.

[75] C.-Y. Park, T. Abukawa, T. Kinoshita, Y. Enta, and S. Kono, "**Low Energy Electron Diffraction and X-Ray Photoelectron Spectroscopy Studies of the Formation of Submonolayer Interfaces of Sb/Si(111)**," *Japanese Journal of Applied Physics*, vol. 27, pp. 147–148, jan 1988.

[76] V. K. Paliwal, A. G. Vedeshwar, and S. M. Shivaprasad, "**Residual thermal desorption study of the room-temperature-formed Sb/Si(111) interface**," *Physical Review B*, vol. 66, p. 245404, dec 2002.

[77] S. Bengió, M. Martin, J. Avila, M. Asensio, and H. Ascolani, "**Atomic structure of the Sb-terminated Si(111) surface: A photoelectron diffraction study**," *Physical Review B*, vol. 65, p. 205326, may 2002.

[78] A. Antons, Y. Cao, B. Voigtländer, K. Schroeder, R. Berger, and S. Blügel, "**Strain-induced surface structures on Sb-covered Ge(111): Epitaxial Ge films on Si(111):Sb**," *Europhysics Letters (EPL)*, vol. 62, pp. 547–553, may 2003.

[79] K.-H. Park, J. S. Ha, W. S. Yun, E.-H. Lee, J.-Y. Yi, and S.-J. Park, "**Atomic structure and formation kinetics of the Sb/Si(111)-$5\sqrt{3} \times 5\sqrt{3}$ surface**," *Physical Review B*, vol. 55, pp. 9267–9270, apr 1997.

[80] A. Giussani, K. Perumal, M. Hanke, P. Rodenbach, H. Riechert, and R. Calarco, "**On the epitaxy of germanium telluride thin films on silicon substrates**," *Physica Status Solidi (B)*, vol. 249, pp. 1939–1944, oct 2012.

[81] P. Hirsch, "**Nucleation and propagation of misfit dislocations in strained epitaxial layer systems**," *Polycrystalline Semiconductors II*, vol. 54, pp. 470–482, 1991.

[82] F. Grey and J. Bohr, "**A Symmetry Principle for Epitaxial Rotation**," *Europhysics Letters (EPL)*, vol. 18, pp. 717–722, apr 1992.

[83] K. Momma and F. Izumi, "**VESTA 3 for three-dimensional visualization of crystal, volumetric and morphology data**," *Journal of Applied Crystallography*, vol. 44, pp. 1272–1276, dec 2011.

[84] J. E. Boschker, J. Momand, V. Bragaglia, R. Wang, K. Perumal, A. Giussani, B. J. Kooi, H. Riechert, and R. Calarco, "**Surface reconstruction-induced coincidence lattice formation between two-dimensionally bonded materials and a three-dimensionally bonded substrate**," *Nano letters*, vol. 14, pp. 3534–8, jun 2014.

[85] A. Koma, "**Van der Waals epitaxy—a new epitaxial growth method for a highly lattice-mismatched system**," *Thin Solid Films*, vol. 216, pp. 72–76, aug 1992.

[86] A. V. Kolobov, M. Krbal, P. Fons, J. Tominaga, and T. Uruga, "**Distortion-triggered loss of long-range order in solids with bonding energy hierarchy**," *Nature Chemistry*, vol. 3, pp. 311–316, mar 2011.

[87] W. H. Hall, "**X-Ray Line Broadening in Metals**," *Proceedings of the Physical Society. Section A*, vol. 62, no. 11, pp. 741–743, 2002.

[88] L. Tarnawska, A. Giussani, P. Zaumseil, M. a. Schubert, R. Paszkiewicz, O. Brandt, P. Storck, and T. Schroeder, "**Single crystalline Sc_2O_3/Y_2O_3 heterostructures as novel engineered buffer approach for GaN integration on Si (111)**," *Journal of Applied Physics*, vol. 108, no. 6, p. 063502, 2010.

[89] W. Braun, R. Shayduk, T. Flissikowski, M. Ramsteiner, H. T. Grahn, H. Riechert, P. Fons, and A. V. Kolobov, "**Epitaxy of Ge–Sb–Te phase-change memory alloys**," *Applied Physics Letters*, vol. 94, p. 041902, 2009.

[90] D. N. McCarthy, S. Yaginuma, H. Gui, and T. Nagao, "**Thickness dependent phase transition of Bi films quench condensed on semiconducting surfaces**," *CrystEngComm*, vol. 13, no. 14, p. 4604, 2011.

[91] M. Hashimoto, T. Niizeki, and K. Kambe, "**Effect of Substrate Temperature on Crystallization of Amorphous Antimony Film**," *Japanese journal of applied physics*, vol. 19, no. 1, pp. 21–23, 1980.

[92] M. Vyshnepolsky, C. Klein, F. Klasing, a. Hanisch-Blicharski, and M. Horn-Von Hoegen, "**Epitaxial growth of the topological insulator Bi_2Se_3 on Si(111): Growth mode, lattice parameter, and strain state**," *Applied Physics Letters*, vol. 103, no. 11, pp. 2011–2015, 2013.

[93] M. Hanke, V. M. Kaganer, O. Bierwagen, M. Niehle, and A. Trampert, "**Delayed crystallization of ultrathin Gd_2O_3 layers on Si(111) observed by in situ X-ray diffraction**," 2012.

[94] Y. Kim, A. DiVenere, G. K. L. Wong, J. B. Ketterson, S. Cho, and J. R. Meyer, "**Structural and thermoelectric transport properties of Sb_2Te_3 thin films grown by molecular beam epitaxy**," *Journal of Applied Physics*, vol. 91, no. 2, p. 715, 2002.

[95] F. Katmis, R. Calarco, K. Perumal, P. Rodenbach, A. Giussani, M. Hanke, A. Proessdorf, A. Trampert, F. Grosse, R. Shayduk, R. Campion, W. Braun, and H. Riechert, "**Insight into the Growth and Control of Single-Crystal Layers of Ge–Sb–Te Phase-Change Material**," *Crystal Growth & Design*, vol. 11, pp. 4606–4610, oct 2011.

[96] A. C. Ferrari and D. M. Basko, "**Raman spectroscopy as a versatile tool for studying the properties of graphene**," *Nature nanotechnology*, vol. 8, no. 4, pp. 235–46, 2013.

[97] J. K. Huang, J. Pu, C. L. Hsu, M. H. Chiu, Z. Y. Juang, Y. H. Chang, W. H. Chang, Y. Iwasa, T. Takenobu, and L. J. Li, "**Large-area synthesis of highly crystalline WSe_2 monolayers and device applications**," *ACS Nano*, vol. 8, no. 1, pp. 923–930, 2014.

[98] N. N. Yu, H. Tong, J. Zhou, a. a. Elbashir, and X. S. Miao, "**Local order of Ge atoms in amorphous GeTe nanoscale ultrathin films**," *Applied Physics Letters*, vol. 103, no. 6, p. 061910, 2013.

[99] K. S. Andrikopoulos, S. N. Yannopoulos, G. A. Voyiatzis, A. V. Kolobov, M. Ribes, and J. Tominaga, "**Raman scattering study of the a-GeTe structure and possible mechanism for the amorphous to crystal transition**," *Journal of Physics: Condensed Matter*, vol. 18, pp. 965–979, jan 2006.

[100] K. Andrikopoulos, S. Yannopoulos, A. Kolobov, P. Fons, and J. Tominaga, "**Raman scattering study of GeTe and $Ge_2Sb_2Te_5$ phase-change materials**," *Journal of Physics and Chemistry of Solids*, vol. 68, pp. 1074–1078, may 2007.

[101] G. Lucovsky and R. M. R. White, "**Effects of Resonance Bonding on the Properties of Crystalline and Amorphous Semiconductors**," *Physical Review B*, vol. 8, p. 660, jul 1973.

[102] A. V. Kolobov, P. Fons, J. Tominaga, A. L. Ankudinov, S. N. Yannopoulos, and K. S. Andrikopoulos, "**Crystallization-induced short-range order changes in amorphous GeTe**," *Journal of Physics: Condensed Matter*, vol. 16, pp. S5103–S5108, nov 2004.

[103] R. Shayduk and W. Braun, "**Epitaxial films for Ge-Sb-Te phase change memory**," *Journal of Crystal Growth*, vol. 311, pp. 2215–2219, 2009.

[104] T. Chattopadhyay, J. Boucherle, and H. Vonschnering, "**Neutron diffraction study on the structural phase transition in GeTe**," *Journal of Physics C: Solid State Physics*, vol. 20, p. 1431, mar 1987.

[105] T. Matsunaga, N. Yamada, and Y. Kubota, "**Structures of stable and metastable $Ge_2Sb_2Te_5$, an intermetallic compound in GeTe-Sb_2Te_3 pseudobinary systems**," *Acta crystallographica. Section B, Structural science*, vol. 60, pp. 685–91, dec 2004.

[106] K. Uchinokura, T. Sekine, and E. Matsuura, "**Critical-point analysis of the two-phonon Raman spectrum of silicon**," *Journal of Physics and Chemistry of Solids*, vol. 35, pp. 171–180, jan 1974.

[107] E. Steigmeier and G. Harbeke, "**Soft phonon mode and ferroelectricity in GeTe**," *Solid State Communications*, vol. 8, pp. 1275–1279, aug 1970.

[108] R. Loudon, "**The Raman effect in crystals**," *Advances in Physics*, vol. 13, pp. 423–482, oct 1964.

[109] S. Baroni, S. De Gironcoli, A. Dal Corso, and P. Giannozzi, "**Phonons and related crystal properties from density-functional perturbation theory**," *Reviews of Modern Physics*, vol. 73, no. 2, pp. 515–562, 2001.

[110] D. Campi, D. Donadio, G. C. Sosso, J. Behler, and M. Bernasconi, "**Electron-phonon interaction and thermal boundary resistance at the crystal-amorphous interface of the phase change compound GeTe**," *Journal of Applied Physics*, vol. 117, p. 015304, 2015.

[111] J. Raty, V. Godlevsky, P. Ghosez, C. Bichara, J. Gaspard, and J. R. Chelikowsky, "**Evidence of a Reentrant Peierls Distortion in Liquid GeTe**," *Phys. Rev. Lett.*, vol. 85, no. 9, pp. 1950–1953, 2000.

[112] X. Biquard, M. Krbal, A. V. Kolobov, P. Fons, R. E. Simpson, B. Hyot, B. Andŕ, J. Tominaga, and T. Uruga, "**Effect of doping on global and local order in crystalline GeTe**," *Applied Physics Letters*, vol. 98, no. 2011, pp. 10–13, 2011.

[113] G. Dhanaraj, K. Byrappa, V. Prasad, and M. Dudley, **Springer Handbook of Crystal Growth**; Springer Science & Business Media, 2010.

[114] S. Soeya and T. Shintani, "**Crystalline structure of GeTe layer in GeTe/Sb_2Te_3 superlattice for phase change memory**," *Journal of Applied Physics*, vol. 112, no. 3, p. 034301, 2012.

[115] R. E. Simpson, P. Fons, a. V. Kolobov, M. Krbal, and J. Tominaga, "**Enhanced crystallization of GeTe from an Sb_2Te_3 template**," *Applied Physics Letters*, vol. 100, no. 2, p. 21911, 2012.

[116] B. Sa, J. Zhou, Z. Sun, J. Tominaga, and R. Ahuja, "**Topological Insulating in GeTe/Sb_2Te_3 Phase-Change Superlattice**," *Physical Review Letters*, vol. 109, p. 096802, aug 2012.

[117] L. Xiu and Z. Wu, "**Simulation of x-ray diffraction for superlattices with fluctuations from perfect periodicity**," *Journal of Applied Physics*, vol. 71, no. 10, p. 4892, 1992.

[118] J. Da Silva, A. Walsh, and H. Lee, "**Insights into the structure of the stable and metastable $(GeTe)_m(Sb_2Te_3)_n$ compounds**," *Physical Review B*, vol. 78, p. 224111, dec 2008.

[119] G. C. Sosso, S. Caravati, and M. Bernasconi, "**Vibrational properties of crystalline Sb_2Te_3 from first principles**," *Journal of physics. Condensed matter : an Institute of Physics journal*, vol. 21, p. 095410, mar 2009.

[120] P. Němec, A. Moreac, V. Nazabal, M. Pavlišta, J. Přikryl, and M. Frumar, "**Ge-Sb-Te thin films deposited by pulsed laser: An ellipsometry and Raman scattering spectroscopy study**," *Journal of Applied Physics*, vol. 106, no. 10, 2009.

[121] G. Meyer, B. Voigtländer, and N. M. Amer, "**Scanning tunneling microscopy of surfactant-mediated epitaxy of Ge on Si(111): strain relief mechanisms and growth kinetics**," *Surface Science*, vol. 274, pp. L541–L545, aug 1992.

[122] B. J. Kooi and J. T. M. De Hosson, "**Electron diffraction and high-resolution transmission electron microscopy of the high temperature crystal structures of $Ge_xSb_2Te_{3+x}$ (x=1,2,3) phase change material**," *Journal of Applied Physics*, vol. 92, no. 7, p. 3584, 2002.

[123] K. Perumal, W. Braun, H. Riechert, and R. Calarco, "**Desorption kinetics of GeTe deposited on Si(111)**," *EPCOS*, 2012.

[124] C. V. Manzano, B. Abad, M. Muñoz Rojo, Y. R. Koh, S. L. Hodson, A. M. Lopez Martinez, X. Xu, A. Shakouri, T. D. Sands, T. Borca-Tasciuc, and M. Martin-Gonzalez, "**Anisotropic Effects on the Thermoelectric Properties of Highly Oriented Electrodeposited Bi_2Te_3 Films**," *Scientific reports*, vol. 6, no. November 2015, p. 19129, 2016.

[125] C. Rinaldi, J. C. Rojas-Sánchez, R. N. Wang, Y. Fu, S. Oyarzun, L. Vila, S. Bertoli, M. Asa, L. Baldrati, M. Cantoni, J.-M. George, R. Calarco, A. Fert, and R. Bertacco, "**Evidence for spin to charge conversion in GeTe(111)**," *APL Materials*, vol. 4, no. 3, p. 032501, 2016.

[126] T. Ohyanagi, N. Takaura, M. Tai, M. Kitamura, M. Kinoshita, K. Akita, T. Morikawa, S. Kato, M. Araidai, K. Kamiya, T. Yamamoto, and K. Shiraishi, "**Charge-injection phase change memory with high-quality GeTe/Sb_2Te_3 superlattice featuring 70μA RESET, 10-ns SET and 100M endurance cycles operations**," in *2013 IEEE International Electron Devices Meeting*, pp. 30.5.1–30.5.4, IEEE, dec 2013.

[127] J. E. Boschker and R. Calarco, "**Enhanced non-thermal switching in interfacial phase change memory** (unpublished)," 2016.

[128] L. Schrottke, M. Wienold, R. Sharma, X. Lü, K. Biermann, R. Hey, a. Tahraoui, H. Richter, H.-W. Hübers, and H. T. Grahn, "**Quantum-cascade lasers as local oscillators for heterodyne spectrometers in the spectral range around 4.745 THz**," *Semiconductor Science and Technology*, vol. 28, p. 035011, 2013.

[129] V. Pardo, A. S. Botana, and D. Baldomir, "**Strain effects to optimize thermoelectric properties of hole-doped La_2NiO_4 via ab initio calculations**," *Physical Review B*, vol. 87, p. 125148, mar 2013.

[130] D. D. Cuong, S. H. Rhim, J.-H. Lee, and S. C. Hong, "**Strain effect on electronic structure and thermoelectric properties of orthorhombic SnSe: A first principles study**," *AIP Advances*, vol. 5, no. 11, p. 117147, 2015.

[131] M. N. Schneider, P. Urban, A. Leineweber, M. Döblinger, and O. Oeckler, "**Influence of stress and strain on the kinetic stability and phase transitions of cubicand pseudocubic Ge-Sb-Te materials**," *Physical Review B*, vol. 81, pp. 1–9, may 2010.

[132] X. Zhou, J. Kalikka, X. Ji, L. Wu, Z. Song, and R. E. Simpson, "**Phase-Change Memory Materials by Design: A Strain Engineering Approach**," *Advanced Materials*, pp. n/a–n/a, feb 2016.